Doctoral Thesis

Fabrication and Evaluation of Functional Thin Films and Electrochemical Devices and Application of Machine Learning

（機能性薄膜と電気化学デバイスの作製と評価及び機械学習の応用）

March 2022

JEONG CHANYANG

Contents

Chapter 1

Introduction

Adjusting the indoor environment to human needs is attractive and the proper approach for this is to adjust it in a reversible way [1-3]. Recently, adjusting the indoor environment has been made possible to some extent by incorporating chromogenic technology into many items (e.g. planes[4], automobiles[5,6], buildings[7], etc.), due to its optical change properties in response to a variety of external stimuli; light (photochromism[8]), temperature (thermochromism[9]), or external voltage (electrochromism[10,11]). Among the chromogenic technologies, the electrochromic technology enables automatic switching control of the light transmittance from the outside with a small voltage. Therefore, electrochromic technology has attracted considerable attention because it is effective for energy saving compared to other technologies[11,12]. In addition, the electrochromic properties provide greater optical contrast and adjustable memory independent of backlight and viewing angle compared to liquid crystal technology. Electrochromic materials are an application of special interest due to the need to produce energy-efficient systems that can reduce fossil fuel consumption in the context of the current world's energy problem[13].

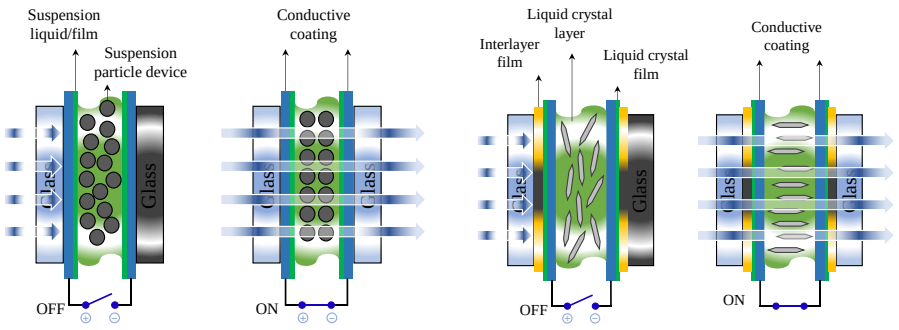

(a) Suspension particle device (SPD) (b) Polymer dispersed liquid crystal (PDLC)

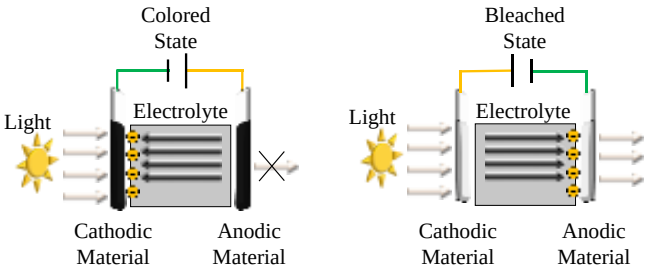

(c) Electrochromic device (ECD)

Figure 1. 1 Illustration of (a) suspension particle device, (b) polymer dispersed liquid crystal, and (c) electrochromic device.

Electrochromic devices are usually organized into five layers: transparent conductive electrode, anodic electrochromic layer, electrolyte layer, cathodic electrochromic layer, and transparent conductive electrode[3]. Electrochromic material can control transmittance by changing optical properties as shown in Figure 1. 1 according to the electrochemical reaction by the movement of ions (e.g., H^+ and Li^+) contained in the electrolyte.

The sputtering method is a representative method of manufacturing a functional thin film such as an EC material[14-17]. Although this has the advantage of continuously fabricating a uniform thin film, it has a disadvantage that needs high cost for fabricating process due to a long manufacturing process such as forming a vacuum atmosphere. Recently, attempts have been reported for the application of coating and printing methods to make a large-scale functional thin film in a short time[18-20]. However, many challenges such as adhesive, uniformity properties remain in the production of functional nano-dispersion inks for thin film production for practical application of coating or printing methods. Therefore, in this study, we focused on the preparation of nanoparticles dispersed inks applicable to the coating methods, and the fabrication of functional thin films using them. In addition, we applied machine learning to examine ink and thin-film fabrication parameters (e.g., materials amount, fabrication conditions, thin-film properties, etc.).

1. 1 Chromism

Chromism is a reversible change in the color of a compound caused by an external stimulus (electricity, light, heat, etc.)[21]. Representatively, inorganic and organic compounds and conductive polymers (CPs) are known as chromism materials, and they involve a variety of mechanisms. In recent years, as interest in global warming and carbon conservation has increased, research and development for low-power systems has been actively carried out. Typically, energy-efficient chromic technology has been developed in various forms for automobile rear mirrors[22], airplanes[4] and smart windows[23,24] of buildings. Chromism is based on changes in the electronic states of molecules, especially the π- and d-electronic states. Therefore, this development is triggered by various external stimuli that can change the electron density of the material. Table 1. 1 summarizes the main types of chromism.

Table. 1. 1 Main types of chromism.

Chromism	Type of stimuli
Thermochromism	Heat
Photochromism	Light irradiation
Gasochromism	Gas
Ionochromism	Ions
Solvatochromism	Solvent polarity
Halochromism	Change in pH
Piezochromism	Mechanical pressure
Electrochromism	Change in potential

1) Thermochromism

Thermochromism shows a reversible change in color in response to changes in temperature (heating or cooling). Various substances such as organic, inorganic, organic metal, supramolecular, and polymer systems exhibit this behavior in thermochromic materials. A typical example is a composite material of VO_x[25] and cobalt hexacyanoferrate[26].

2) Photochromism

Photochromism is a phenomenon in which the color changes when a specific wavelength is irradiated to a compound[27]. Various transition metal oxides such as MoO_3, WO_3, TiO_2, V_2O_5, and Nb_2O_5 exhibit a color change when exposed to either sunlight or UV radiation[28].

3) Gasochromism

Gasochromism is a phenomenon that exhibits a reversible color change when a compound reacts with a gas such as oxygen or hydrogen, and is typically used in gas sensors. The most typical gasochromism material is tungsten oxide (WO_3)[29,30], and it has been reported that Mg alloyed with VO_x[31], Mg-Ni[32], and alkaline earth metals[33] also exhibits gasochromism.

4) Ionochromism

Ionochromism is a phenomenon in which the addition of ions causes a reversible color change[34].

5) Halochromism

Halochromism is a phenomenon in which interaction with ionic species causes a

reversible color change. A wide range of color changes from colorless to colored or from one color to another. The most common materials are pH-sensitive materials, which have been used for decades as analytical pH indicators[35].

6) Solvatochromism

Solvatochromism is a reversible color change caused by a solvent, often manifested by a change in the polarity of the solvent. Poly(3-alkyl thiophenes) are known as solvatochromic materials, and the color change of the compound occurs through a charge transfer mechanism[36].

7) Piezochromism

Piezochromism is a type of mechanochromism that occurs as a result of the application of pressure. In general, organic polymers such as polydiacetylene and polythiophene are known as piezochromic materials[37].

8) Electrochromism

Electrochromism (EC) is a reversible change in optical properties when a material is oxidized or reduced due to an electrochemical reaction. This phenomenon was known when Deb discovered the electrochromic properties of WO_3 in 1968. WO_3 can be used for a variety of applications because it exhibits not only visible color change at low power but also transmittance change at wavelengths in the NIR, thermal infrared and microwave regions. In recent years, interest in low-power systems has been increasing due to environmental problems such as global warming, and energy-efficient EC technology is being actively developed in various fields such as automobile rearview mirrors, information displays, and smart windows. Table 1. 2 listed the mainly used materials of electrochromism[1-8].

Table 1. 2 The main materials of electrochromism.

Materials	Color change		Methods	Ref.
	Oxidation ⇔ Reduction			
WO_3	Colorless	Blue	Coating	18
V_2O_5	Colorless	Green	Colloid coating	38
TiO_2	Colorless	Blue	Colloidal dispersion	39
NiOOH	Brown	Colorless	Sputtering	16, 17
CoOOH	Brown	Colorless	Ionization precipitation	40
Rh_2O_3	Yellow	Dark green	Sputtering	14, 15
IrO_x	Dark blue	Colorless	Sputtering	41
Heptyl viologen	Red-purple	Colorless	Clathrate compound	42
Prussian blue	Blue	Colorless	Coating	5
InN	Yellow	Gray	RF ion plating	43
SnN_x	Dark brown	Gray	chemical vapor deposition	44

1. 2 Electrochromic devices (ECDs)

1) Structure of ECDs

Typically, ECDs consist of seven layers as shown in Figure 1. 2. In this structure, three active layers (anodic or cathodic EC layers, electrolyte layer) are sandwiched between two transparent conductor electrode layers. In addition, transparent glass and plastic are typically used for the substrate, and two substrate layers are placed outside to protect the five layers. Electroactive materials (anodic or cathodic EC layers) that exhibit reversible changes in optical properties are required to exhibit EC effects. Electrons or ions move from a EC layer (i.e. cathodic EC layer) through the electrolyte layer to exchange with an another EC layer (i.e. anodic EC layer) layer. Typical EC devices require contact between each layer to obtain good electrochemical properties.

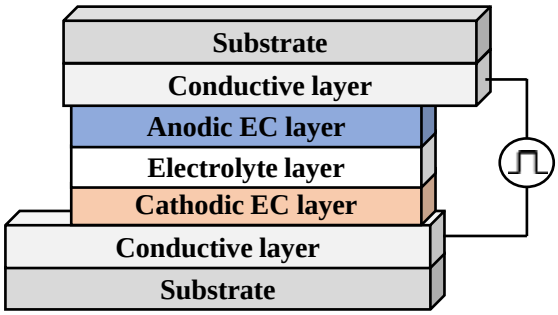

Figure 1. 2 Structure of electrochromic device

2) Electrolyte

The electrolyte may be in a liquid, gel, or solid phase. If the electrolyte layer is a liquid or gel, the ionic conductivity is high, but there is a risk of electrolyte leakage[45]. Therefore, sealing is necessary to completely prevent leakage of electrolytes. In contrast, solid electrolytes have high safety but low ionic conductivity. Many polymer electrolytes, salts are dissolved in a solution having a viscosity. In this case, NaCl and $LiClO_4$ are typically used as salts, and they are widely used as general-purpose electrolytes in the fabrication of PET(polyethylene terephthalate)-based flexible EC

devices.

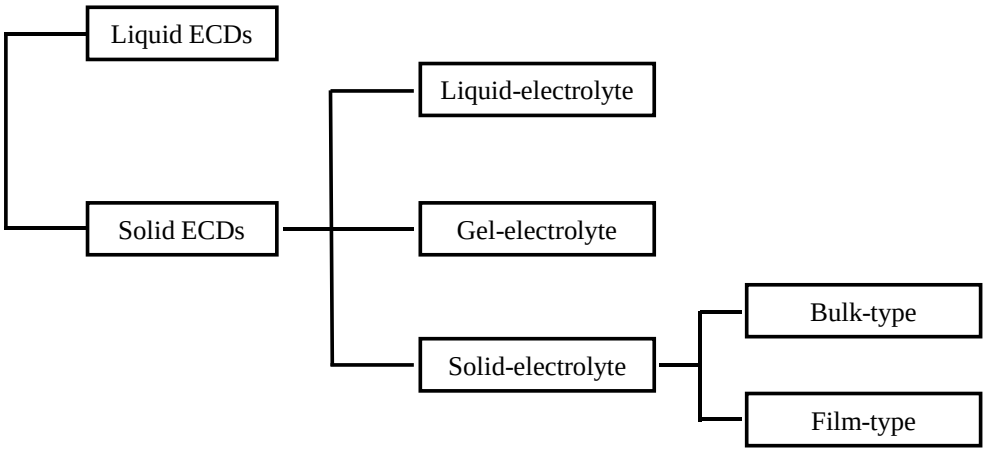

Figure 1. 3 Types of ECD electrolytes

1. 3 Electrochromic device application

In recent years, ECD has attracted attention because of its extremely low energy consumption, which can realize energy savings. Figure 1. 4 shows electrochromic devices in practical applications. For example, architectural applications include energy-efficient Glazing, privacy glass, skylights, etc., and automotive applications are used for sun routes and mirrors. Typical electrochromic smart windows include the Boeing 787, architectural applications include energy-efficient glazing, privacy glazing, skylights, and automotive applications for solar pathways and mirrors.

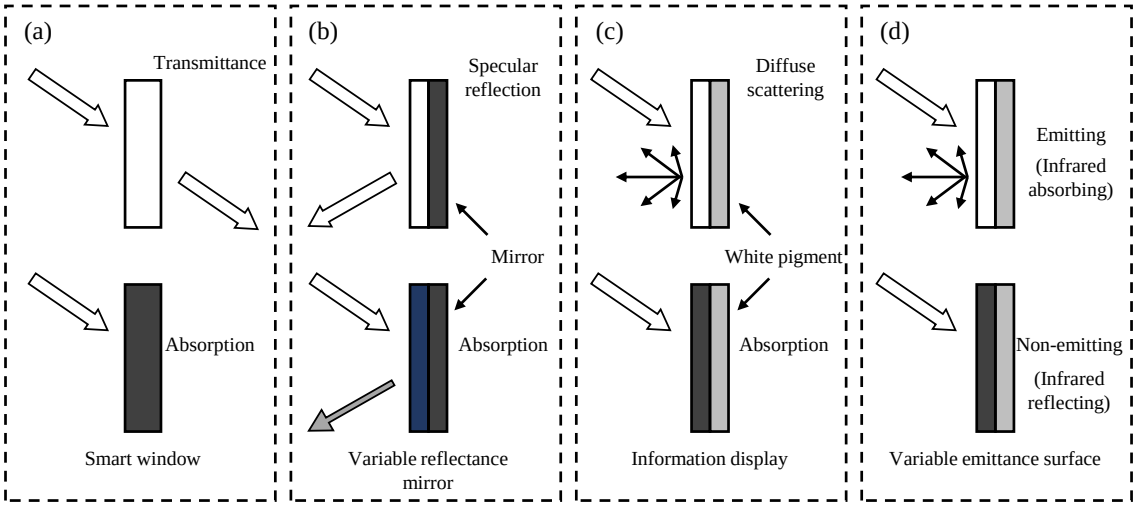

Figure 1. 4 (a) smart window, (b) variable reflectance mirror, (c) information display and (d) variable emittance surface[3].

1) Anti-glare rearview mirrors

Anti-glare rearview mirrors are EC devices that detect and eliminate rearview mirror glare to avoid driver glare from reflected vehicle light as shown in Figure 1. 5. The anti-glare rearview mirror has the structure shown in Figure 1. 4 (b) and reflects light while maintaining the function of a regular mirror when the surroundings are dark. On the other hand, when glare is detected, the EC material changes to a colored state to reduce light reflection, optically absorbing light from the reflective surface to prevent glare[46].

Figure 1. 5 Regular and anti-glare rearview mirrors.

2) EC information display and paper

EC displays are similar to LCD technology and require external lighting. EC displays have the advantage of retaining color due to memory effects like batteries. However, the slow switching speed limits applications such as reusable price labels or billboards. In addition, in the case of a large-area display, the electrochemical reaction does not occur smoothly in the center far from the electrode, so the electrochromic characteristics may be non-uniform. Examples of the EC display are shown in Figure 1. 6.

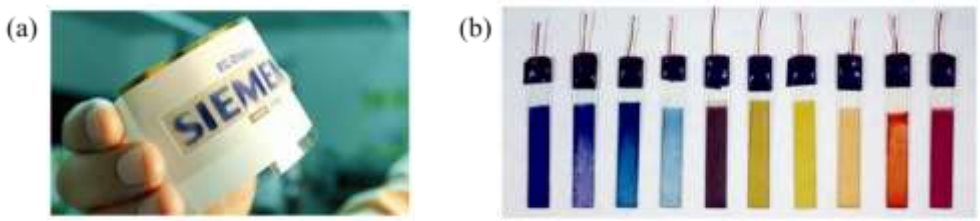

Figure 1. 6 (a) A flexible EC display, as developed by Siemens[47], and (b) EC display in various colors with polymer films prepared on indium-tin oxide coated glasses[48].

3) EC smart windows

Recently, due to concerns about the depletion of fossil fuels and environmental destruction due to global warming, interest in the use and development of green energy materials to replace fossil fuels is increasing. Most of these energies are used for heating and cooling of buildings. Therefore, there is a need for an efficient energy system that can control the indoor environment with a pleasant and low energy at the same time. Electrochromic (EC) windows, which can change their optical properties following an electrochemical redox reaction, are attractive for energy-efficient applications in

architectures for reducing global consumption of limited energy resources and for human comfort[10]. Unlike other devices, energy is required only during the switching time. Once switched, a potential is applied in the reverse direction, remaining transparent/opaque until disturbed again. A typical application is the window of a Boeing 787, which is shown in Figure 1. 7.

Figure 1. 7 EC smart window of Boeing 787

1. 4 Type of ECDs

Three types of ECDs exist and are directly related electrochemically and classified as shown in Figure 1. 8. The three main EC window configurations currently demonstrated are solution, hybrid, and battery-like types[49].

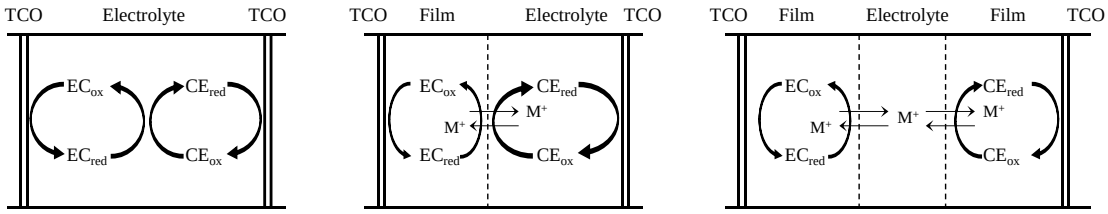

Figure 1. 8 Three types of ECDs applications

.

The optically transparent front and back electrodes for carrying current in the construction of these three types of all-solid (solution), liquid/solid (hybrid) and all-solid (battery-like) electrochromic systems are common in construction.
The EC reaction can be written as:

$$EC^n + yCE^m(bleached) \Leftrightarrow EC^{n-a} + yCE^{m+a/y}(colored)$$

where CE and EC are counter electrode and EC layers, respectively.

Type I : Solution configuration.

$$MV^{2+}(aq) + e(colorless) \Leftrightarrow MV^{+*}(aq)(Dark\ \ blue)$$

where MV is methyl viologen.

Type II : Hybrid configuration.

$$CPQ^{2+}(aq) + e^- + X^-(aq)(colorless) \Leftrightarrow [CPQ^{+*}X^-](s)(Dark\ \ blue)$$

Where CPQ is cyanophenylparaquat.

Type III : Battery-like configuration.

$$MO^{2+}(s) + e(colorless) \Leftrightarrow MO^{+*}(s)(Dark\ \ blue)$$

where MO is metal oxide.

Type III EC materials are in solid state in both bleached and colored states. Their structure is shown in Figure 1. 1.

Solution and hybrid ECD types require continuous application of electrical energy to maintain EC properties. By contrast, the battery-like ECD type has battery-like characteristics and exhibits open circuit memory.

1. 5 Electrochromic materials

The most representative compounds exhibiting electrochromic materials are Transition metal oxides (TMOs), Prussian Blue (PB) and its analogues, and viologens, etc[3]. The detailed materials are listed in Table 1. 3.

Table 1. 3 The EC materials examples and potential uses

Class of EC materials	Example
Transition metal oxides (TMOs)	WO_3, MoO_3, V_2O_5, Nb_2O_5, IrO_x, and NiO_x
Prussian Blue (PB) system	$Fe_x[Fe(CN)6]_y$ (FeHCF), $Ni_x[Fe(CN)6]_y$ (NiHCF), $Zn_x[Fe(CN)6]_y$ (ZnHCF), and $Cu_x[Fe(CN)6]_y$ (CuHCF)
Viologens	1,1′-Disubstituted-4,4′-bipyridinium salts (being pyridinium=C_5H_6N).
Conducting polymers	PEDOT (being EDOT=$C_6H_6O_2S$), PPy (being Py=Pirrole=C_4H_5N), PT (being =thiophene=C_4H_4S), and PANI (being anyline=ANI=$C_6H_5NH_2$)
Transition metal and lanthanide	poly-$[Ru^{II}(vbpy)_2(py)_2]Cl_2$ (being py=pyridine =C_5H_5N)
Metal phthalocyanies (Pc)	$[Lu(Pc)_2]$ being Pc= $C_{32}H_{18}N_8$

1. 5. 1 Transition metal oxides (TMOs)

The periodic table in the figure shows two types of transition metal oxide (cathode and anode) materials exhibiting EC properties. It can be classified as shown in Figure 1. 9 according to whether the material is colored by ion charging or discharging, i.e. reduction or oxidation processes, respectively. Representative cathode EC materials (blue) are TiO_x[50] and WO_x[5,19,20], of which the first reported and widely studied material is tungsten oxide (WO_3). The anode coloring (red) includes NiO_x[16,17] and IrO_x[41], and the most irradiated counter electrode of tungsten is nickel oxide (NiO_x).

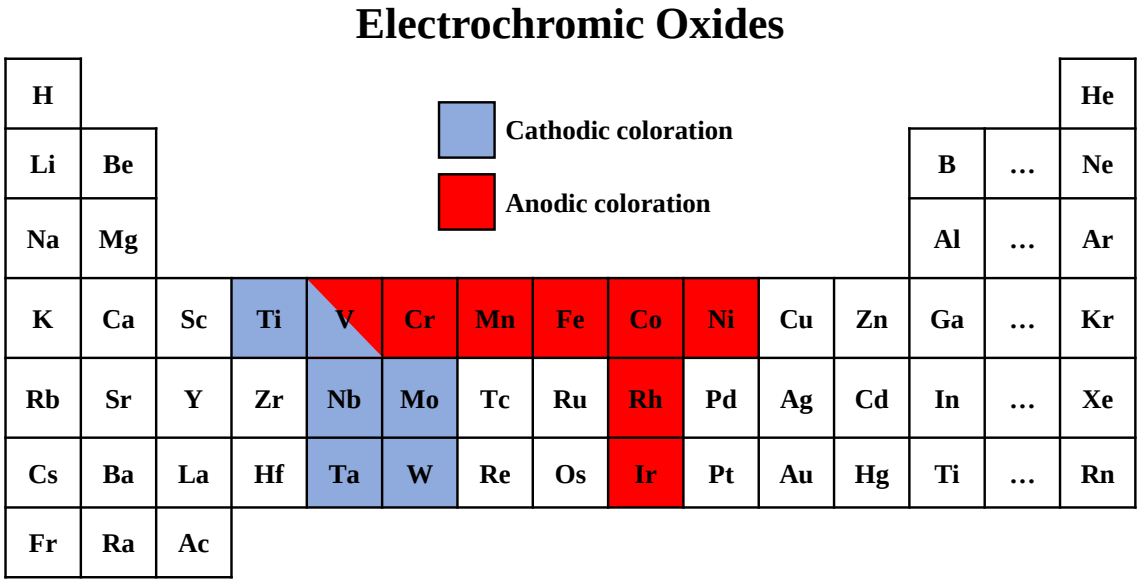

Figure 1. 9 Electrochromic oxides showing both cathodic and anodic coloration[3].

1) Tungsten oxide

WO_3 was first discovered by Deb in the 1960s and is the most studied EC material[51]. It changes reversely from transparent (oxidized state) to dark blue (reduced state) according to an electrochemical reaction. Their electrochromic properties are greatly affected by the composition, structure, pores, and type of electrolyte (ion size) of the thin film [52]. The redox process of WO_3 can be represented as follows.:

$$WO_3 + x(M^+ + e^-)(transparent) \Leftrightarrow M_xWO_3(Blue)$$
$$WO_3 + x(M^+ + xe^-) \Leftrightarrow M_x{W^{VI}}_{(x-1)}{W^V}_xO_3$$

where M^+ is usually considerable to be H^+, Li^+, Na^+ or K^+. WO_3 exhibits transparent in the W^{6+} (oxidation) state and exhibits blue color in the W^{5+} (reduced) state. In addition, the color become more darker as decrease the x value of WO_x.

1. 5. 2 Prussian Blue (PB) and PB analogs

PB (FeHCF) and its analogs (PBA) have the following chemical formula.

$$A_x M_A[M_B(CN)_6]_{1-y} \cdot zH_2O$$

where A is an intercalating ion such as that of potassium or sodium. M_A and M_B are transition metals such as Fe, Mn, Ni and Cu, and y is the number of $[M_B(CN)]_6$ vacancies[53] (Figure 1. 10). The CN group connects M_A and M_B; the M_A and M_B atoms are coordinated to 6 nitrogen and 6 carbon atoms, respectively, forming structures such as Metal Organic Frameworks (MOFs)[54]. In the case of PB used in electrochemical materials, the size of the pores in the structure varies depending on the size of M_A and M_B atoms. Therefore, an appropriate ion must be selected.

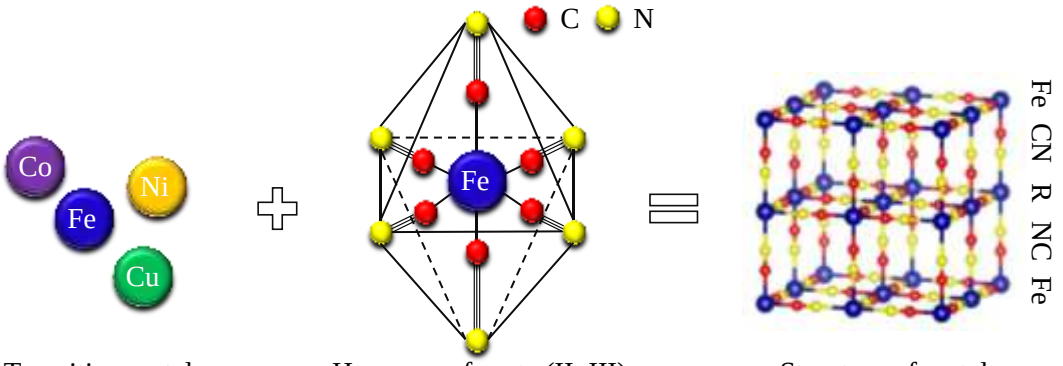

Figure 1. 10 Structural illustration of metal hexacyanoferrate complexes (FeHCF) using transition metal (Fe).

PB and PBA can change their physical properties through combination with various metal elements. Therefore, they are used in various fields and are recently attracting attention as memory or switching materials[55]. In particular, PB is attracting attention in electrochemical applications such as ECD due to the unique structure of the three-dimensional network and tunnel structure as shown in the Figure 1. 10.

The redox reaction of PB is described by the equation:

$$M_A[Fe^{III}(CN)_6] + M^+ + e^- \Leftrightarrow MM_A[Fe^{II}(CN)_6]$$

The EC properties of PB combined with various metal elements are listed in Table 1. 4.

Table 1. 4 Electrochromic properties of MHCFs.

MHCF	Color change		Ref.
	Oxidation ⇔ Reduction		
FeHCF	Blue	Colorless	56, 57
NiHCF	Yellow	Colorless	58
ZnHCF	Colorless	Colorless	59
CuHCF	Yellow	Reddish brown	60
CoHCF	Green	Reddish brown	59, 61
InHCF	Yellowish	Colorless	62

In particular, FeHCF is attracting attention for smart window applications as an anodic EC material with excellent EC properties. PB film prepared by electrodeposition has been reported as an EC material with high durability that shows no degradation in electrochemical and optical modulation from transparent to blue for 5×10^6 cycles[63,64]. In addition, as an anodic EC material, PB can be usefully used in the preparation of complementary ECDs with excellent performance in combining with WO_3, a representative cathodic EC material.

PB exhibits four redox states: colorless (Everitt's salt, ES), sky blue (PB), light green (Berlin green, BG), and yellow (Prussian yellow, PY) as shown in the following equation[56,65].

$$Fe^{III}[Fe^{III}(CN)_6] + e^-(\text{Prussian Brown}) \rightarrow Fe^{III}[Fe^{II}(CN)_6]^-(\text{Prussian Blue})$$
$$Fe^{III}[Fe^{II}(CN)_6]^- + e^-(\text{Prussian Blue}) \rightarrow Fe^{II}[Fe^{II}(CN)_6]^{2-}(\text{Prussian White})$$

1) Prussian Blue nanoparticles

Recently, many attempts have been carried out for application to a functional thin film preparation by using a technology that uses a solution such as printing and coating that can prepare a thin film with low energy in a short time. Therefore, in order to improve the precision of printing/coating technologies for the preparation of electronic devices and fine patterns, the preparation of nanoparticles dispersion solution is a very important part. Since the conventional synthesis of PB nanoparticle dispersions uses organic materials, the PB particles aggregate to form agglomerates of non-uniform particles. Therefore, it is not suitable for producing uniform thin films for use in printing and stripping methods. In addition, a lot of caution is required because organic substances that are harmful to the human body are used in the synthesis process. Therefore, it is necessary to manufacture a uniform and electrochemically active PB thin film for application to electronic devices. That is, it is important to synthesize PB nanoparticles (NPs) in which the small particles are well dispersed in the solvent. Recently, a method for manufacturing eco-friendly and inexpensive PB solution by simply dispersing PB NPs in water without using such hazardous organic materials. The detail mechanism to synthesize PB NPs water-dispersed solution is shown in Figure 1. 11.

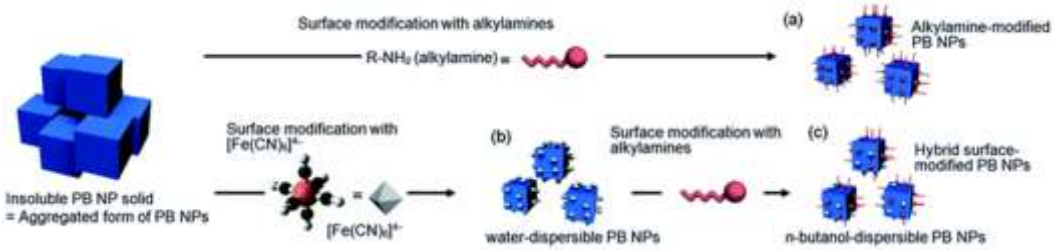

Figure 1. 11 Preparation of water-dispersible PB nanoparticles[66].

1. 5. 3 Organic materials

Organic materials are easy to synthesize, have flexibility and faster reaction rate than TMOs and PBAs, and thus have many advantages for EC device applications. However, organic EC materials must be handled with caution because they use flammable and/or toxic organic solvents, and these safety concerns offset the advantages of organic electrochromic devices. However, it is not environmentally friendly and may not be suitable for long-term EC device manufacturing strategies due to the use of toxic organic substances. Therefore, many attempts have been reported recently for the development of water-soluble organic substances. Organic EC materials can be classified into two types as shown in Figure 1. 12. Type I is a material having one or more colored states and one or more colorless or 'colorless' states. Examples are PEDOT and viologens[67]. They can be colored or bleached in the neutral state of the materials and change color by an electrochemical reaction. Type II material does not change to transparent state. On the other hand, there are two or more color states by an electrochemical reaction, typically polythiophene, which changes from red to blue with oxidation.

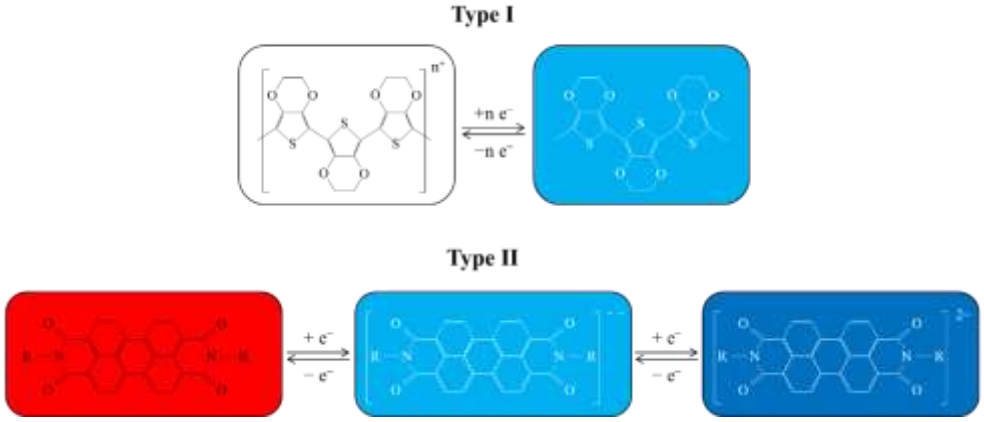

Figure 1. 12 Organic electrochromic materials: Type I: Bleached to colored states and Type II: Colored to colored states

1) Viologens

Viologen is a representative organic compound EC material, and their electrochemical reaction is shown in the following formula and Figure 1. 13[68].

$$bipm^{2+}(Colorless) + e^{-} \rightarrow bipm^{+*}(colored)$$

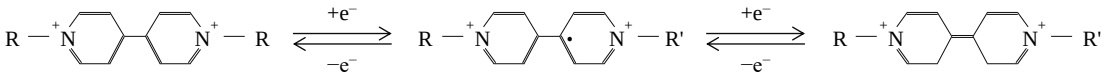

Figure 1. 13 Electrochemical redox reaction of viologens

Diquaternisation of 4.4'-bipyridyl produces 1.1'-dis-ubstituted4.4'-bipyridilium salts, commonly known as 'viologens'. Viologens are colorless and most stable in the dication state ($bipm^{2+} + 2e^{-} \rightarrow bipm^{0}$) which is in oxidation states among the three electrochemical reactions (left in Figure 1. 13). When electrons are reduced ($bipm^{0}$), the color of viologen appears, and the color at this time depends on the substituents R and R'(middle in Figure 1. 13). In addition, when two electrons are reduced, the viologen shows a different color and changes to a neutral state ($bipm^{+\bullet} + e^{-} \rightarrow bipm^{0}$, right in Figure 1. 13). Viologens are attracting attention for EC display or device applications because it has the advantage of being able to display various colors as needed by changing the chemical structure. However, it has fatal disadvantages such as poor electrochemical safety and short lifespan.

2) Conducting polymers: polypyrrole, polythiophene and PEDOT

Electronically conductive polymers are used in the manufacture of EC materials that do not require electrolytes. Representative conductive polymers are shown in Figure 1. 14, and all of them are characterized by having a conjugated ring structure. These are synthesized by doping anions or cations into a polymer material to exhibit conductivity[69]. The synthesized conductive polymer is mainly used for the preparation of thin-film by printing and coating methods, and it is used for complementary ECD

prepared by combining with EC materials such as a WO_3 thin film.

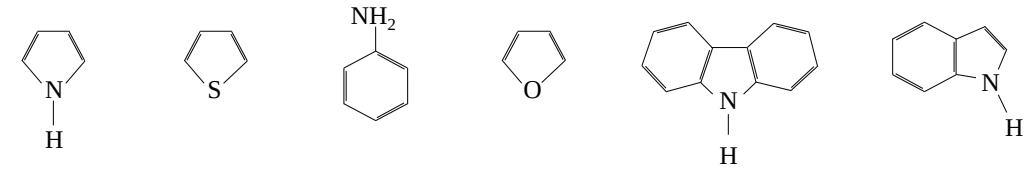

Pyrrole Thiophene Aniline Furan Carbazole Indole

Figure 1. 14 Typical conjugated polymers

1. 6 Machine learning methods

Machine learning (ML) is a technology that uses algorithms to learn and identify patterns in data, and can make predictions using these patterns[70]. Therefore, by applying it to the development of materials with innumerable parameters, the number of experiments required to obtain the optimum parameters can be reduced. In recent years, research and development using machine learning have increased dramatically in various fields. In particular, the deep learning method using algorithms provides optimal material production conditions in a short time in material research fields, enabling innovative development in various fields such as image analysis, data processing, and classification based on this.

1. 7 Aim and outline of this study

A high-performance electrochromic material must possess fast color switching, reversible light modulations, high color contrast, low energy consumption, and long-term chemical and thermal stabilities[1-8,10-13].

Our research group has been studying the synthesis of the WO_3 and PB NPs well dispersed in water without any chemical which is harmful to the human body for application in EC thin films fabrication by coating processes. The coating process has the advantage of being able to fabricate a high-quality EC thin film on a large-area ITO-coated glass substrate in a short time and at a low cost. In the case of coating technology, the adhesive and wettability properties of the substrate and NPs inks are very important as a factor to improve the electrochemical reaction and durability for thin-film preparation.

Therefore, we focused on the development of a wet-coatable WO_3 NPs dispersed ink with good adhesion. Chapter 3 describes in detail the synthesis of a wet-coatable WO_3 NPs dispersed ink with improved adhesion and the correlation between the adhesive and electrochemical properties of the coated WO_3 thin film prepared using the ink.

Chapter 4 describes electrochemical devices of various (glass and flexible PET) substrates that were prepared using the WO_3 ink developed in Chapters 3 and their EC properties were evaluated. Finally, in Chapter 5, we developed a simulation model that can predict the synthesis conditions for the synthesis of WO_3 ink suitable for the coating process using machine learning. In addition, WO_3 ink was prepared using the conditions obtained through the simulation model and verified by comparative analysis.

This research aims to develop functional nano-dispersion ink and thin film that can be applied to coating process in various fields such as catalyst and battery as well as EC smart window material by developing adhesive WO_3 ink that can be finally applied to the coating method.

Reference

[1] R.J. Mortimer, Electrochromic Materials, Annu. Rev. Mater. Sci. 41 (2011) 241. https://doi.org/10.1146/annurev-matsci-062910-100344

[2] R.J. Mortimer, A.L. Dyer, J.R. Reynolds, Electrochromic organic and polymeric materials for display applications, Displays 27 (2006) 2-18. https://doi.org/10.1016/j.displa.2005.03.003

[3] C.G. Granqvist, Handbook of Inorganic Electrochromic Materials, Elsevier, Amsterdam (1995), pp. 1-10.

[4] C.Y. Jeong, T. Kubota, K. Tajima, M. Kitamura, H. Imai, Complementary electrochromic devices based on acrylic substrates for smart window applications in aircrafts, Mater. Chem. Phys. 277 (2022) 125460. https://doi.org/10.1016/j.matchemphys.2021.125460

[5] C.Y. Jeong, T. Kubota, K. Tajima, Flexible electrochromic devices based on tungsten oxide and Prussian blue nanoparticles for automobile applications, RSC Adv. 11 (2021) 28614. https://doi.org/10.1039/D1RA05280B

[6] G. Cai, J. Wang, P.S. Lee, Next-generation multifunctional electrochromic devices, Acc. Chem. Res. 49 (2016) 1469. https://doi.org/10.1002/1521-4095(200106)13:11<783::AID-ADMA783>3.0.CO;2-D

[7] C.G. Granqvist, Electrochromism and smart window design, Solid State Ionics, 53 (1992) 479. https://doi.org/10.1016/0167-2738(92)90418-O

[8] M. Irie, Photochromism: memories and switches introduction, Chem. Rev. 100 (2000) 1683. https://doi.org/10.1021/cr980068l.

[9] J. Harada, T. Fujiwara, K. Ogawa, Crucial role of fluorescence in the solid-state thermochromism of salicylideneanilines, J. Am. Chem. Soc. 129 (2007) 16216. https://doi.org/10.1021/ja076635g

[10] C.G. Granqvist, M.A. Arvizu, İ. Bayrak Pehlivan, H.-Y. Qu, R.-T. Wen, G.A. Niklasson, Electrochromic materials and devices for energy efficiency and human comfort in buildings: A critical review, Electrochim. Acta, 259 (2018) 1170. https://doi.org/10.1016/j.electacta.2017.11.169

[11] A. Azens, C.G. Granqvist, Electrochromic smart windows: energy efficiency and

device aspects, J. Solid State Electrochem. 7 (2003) 64. https://doi.org/10.1007/s10008-002-0313-4

[12] P.R. Somani, S. Radhakrishnan, Electrochromic materials and devices: present and future, Mater. Chem. Phys., 77 (2003) 117. https://doi.org/10.1016/S0254-0584(01)00575-2

[13] C.G. Granqvist, Electrochromics for smart windows: Oxide-based thin films and devices, Thin Solid Films, 564 (2014) 1. https://doi.org/10.1016/j.tsf.2014.02.002

[14] C.Y. Jeong, Y. Abe, M. Kawamura, K.H. Kim, T. Kiba, Electrochromic properties of rhodium oxide thin films prepared by reactive sputtering under an O_2 or H_2O vapor atmosphere, Sol. Energy Mater. Sol. Cells 200 (2019) 109976. https://doi.org/10.1016/j.solmat.2019.109976

[15] C.Y. Jeong, Y. Abe, M. Kawamura, K.H. Kim, T. Kiba, H. Watanabe, K. Tajima, T. Kawamoto, Electrochromic properties of sputter-deposited rhodium oxide thin films of varying thickness, Thin Solid Films 709 (2020) 138226. https://doi.org/10.1016/j.tsf.2020.138226

[16] Y. Yokoiwa, Y. Abe, M. Kawamura, K.H. Kim, T. Kiba, Metallic-mode reactive sputtering of nickel oxide thin films and characterization of their electrochromic properties, Jpn. J. Appl. Phys. 58 (2019) 055504. https://doi.org/10.7567/1347-4065/ab1189

[17] Y. Abe, H. Ueta, T. Obata, M. Kawamura, K. Sasaki, H. Itoh, Effects of sputtering gas pressure on electrochromic properties of Ni oxyhydroxide thin films prepared by reactive sputtering in H_2O atmosphere, Jpn. J. Appl. Phys. 49 (2010) 115802. https://doi.org/10.1143/JJAP.49.115802.

[18] K. Tajima, C.Y. Jeong, T. Kubota, T. Ito, K. Araki, T. Kamei, M. Fukui, Mass-producible slit coating for large-area electrochromic devices, Sol. Energy Mater. Sol. Cells 232 (2021) 111361. https://doi.org/10.1016/j.solmat.2021.111361

[19] P.J. Wojcik, L. Santos, L. Pereira, R. Martins, E. Fortunato, Tailoring nanoscale properties of tungsten oxide for inkjet printed electrochromic devices, Nanoscale 7 (2015) 1696. https://doi.org/10.1039/C4NR05765A

[20] C. Costa, C. Pinheiro, I. Henriques, C.A.T. Laia, Inkjet printing of sol–gel synthesized hydrated tungsten oxide nanoparticles for flexible electrochromic devices,

ACS Appl. Mater. Interfaces 4 (2012) 1330. https://doi.org/10.1021/am201606m
[21] H. Ramlow, K.L. Andrade, A.P.S. Immich, Smart textiles: an overview of recent progress on chromic textiles, J. Text. Inst. 112 (2021) 152-171. https://doi.org/10.1080/00405000.2020.1785071
[22] A. Pawlicka, Development of electrochromic devices, Recent Pat. Nanotechnol. 3 (2009) 177. https://doi.org/10.2174/187221009789177821
[23] A. Piccolo, F. Simone, Performance requirements for electrochromic smart window, J. Build. Eng. 3 (2015) 94. https://doi.org/10.1016/j.jobe.2015.07.002
[24] J.-L. Wang, S.-Z. Sheng, Z. He, R. Wang, Z. Pan, H.-Y. Zhao, J.-W. Liu, S.-H. Yu, Self-powered flexible electrochromic smart window, Nano Lett. 21 (2021) 9976. https://doi.org/10.1021/acs.nanolett.1c03438
[25] C. Batista, R.M. Ribeiro, V. Teixeira, Synthesis and characterization of VO_2-based thermochromic thin films for energy-efficient windows, Nanoscale Res. Lett. 6 (2011) 301. https://doi.org/10.1186/1556-276X-6-301
[26] A. Zanottoa, R. Matassa, M.L. Saladino, M. Berrettoni, M. Giorgetti, S. Zamponi, E. Caponetti, Cobalt hexacyanoferrate–poly(methyl methacrylate) composite: Synthesis and characterization, Mater. Chem. Phys. 120 (2010) 118. https://doi.org/10.1016/j.matchemphys.2009.10.032
[27] J. Z. Zhang, B. J. Schwartz, J. C. King, C. B. Harris, Ultrafast studies of photochromic spiropyrans in solutiom, J. Am. Chem. Soc. 114 (1992) 10921. https://doi.org/10.1021/ja00053a032
[28] S. Songara, M.K. Patra, M. Manoth, L. Saini, V. Gupta, G.S. Gowd, S.R. Vadera, N. Kumar, Synthesis and studies on photochromic properties of vanadium doped TiO_2 nanoparticles, J. Photochem. Photobiol. A: Chem. 209 (2010) 68. https://doi.org/10.1016/j.jphotochem.2009.11.001
[29] V. Wittwer, M. Datz, J. Ell, A. Georg, W. Graf, G. Walze, Gasochromic windows, Sol. Energy Mater. Sol. Cells 84 (2004) 305. https://doi.org/10.1016/j.solmat.2004.01.040
[30] V. Vitry, F. Renaux, R. Gouttebaron, J.-P. Dauchot, M. Hecq, Preparation and characterization of gasochromic thin films, Thin Solid Films 502 (2006) 265. https://doi.org/10.1016/j.tsf.2005.07.293

[31] W.-L. Jang, Y.-M. Lu, Y.-R. Lu, C.-L. Chen, C.-L. Dong, W.-C. Chou, J.-L. Chen, T.-S. Chan, J.-F. Lee, C.-W. Pao, W.-S. Hwang, Effects of oxygen partial pressure on structural and gasochromic properties of sputtered VO_x thin films, Thin Solid Films 544 (2013) 448. https://doi.org/10.1016/j.tsf.2013.02.083

[32] S. Bao, Y. Yamada, K. Tajima, M. Okada, K. Yoshimura, Effect of deposition conditions on the response and durability of an Mg_4Ni film switchable mirror, Vacuum 83 (2009) 486. https://doi.org/10.1016/j.vacuum.2008.04.013

[33] K. Yoshimura, Y. Yamada, S. Bao, K. Tajima, M. Okada, Preparation and characterization of gasochromic switchable-mirror window with practical size, Sol. Energy Mater. Sol. Cells 93 (2009) 2138. https://doi.org/10.1016/j.solmat.2009.03.023

[34] T. S. Lee, H. Ahn, J. K. Lee, W. H. Park, Ionochromic 4,4′-azobispyridinium salt-incorporated polymer: synthesis and optical properties, Optical Mater. 21 (2002) 285. https://doi.org/10.1016/S0925-3467(02)00151-9

[35] L. V. Schueren, K. Hemelsoet, V. V. Speybroeck, K. D. Clerck, The influence of a polyamide matrix on the halochromic behaviour of the pH-sensitive azo dye Nitrazine Yellow, Dyes. Pigm. 94 (2012) 443. https://doi.org/10.1016/j.dyepig.2012.02.013

[36] J. Catalan, On the chromism of polyenes, Chem. Phys. Lett. 457 (2008) 87. https://doi.org/10.1016/j.cplett.2008.03.073

[37] L. Bu, Y. Li, J. Wang, M. Sun, M. Zheng, W. Liu, S. Xue, W. Yang, Synthesis and piezochromic luminescence of aggregation-enhanced emission 9,10-bis(N-alkylcarbazol-2-yl-vinyl-2)anthracenes, Dyes. Pigm. 99 (2013) 833. https://doi.org/10.1016/j.dyepig.2013.07.012

[38] K. Zhao, W. Han, Z. Tang, G. Zhang, J. Lu, G. Lu, X. Zhen, Investigation of coating technology and catalytic performance over monolithic V_2O_5–WO_3/TiO_2 catalyst for selective catalytic reduction of NO_x with NH_3, Colloids Surf. A Physicochem. Eng. Asp. 503 (2016) 53. https://doi.org/10.1016/j.colsurfa.2016.05.014

[39] S. Cao, S. Zhang, T. Zhang, J.Y. Lee, J.Y. Lee, Fluoride-assisted synthesis of plasmonic colloidal Ta-doped TiO_2 nanocrystals for near-infrared and visible-light selective electrochromic modulation, Chem. Mater. 30 (2018) 4838. https://doi.org/10.1021/acs.chemmater.8b02196

[40] F. Švegl, B. Orel, M. Hutchins, Structural and electrochromic properties of Co-oxide

and Co/Al/Si-oxide films prepared by the sol-gel dip coating technique, J. Solgel Sci. Technol. 8 (1997) 765–769. https://doi.org/10.1007/BF02436936

[41] S. Ito, Y. Abe, M. Kawamura, K.H. Kim, Electrochromic properties of iridium oxide thin films prepared by reactive sputtering in O_2 or H_2O atmosphere, J. Vac. Sci. Technol. B 33 (2015) 041204. https://doi.org/10.1116/1.4923227

[42] N. Corrigan, J. Xu, C. Boyer, A photoinitiation system for conventional and controlled radical polymerization at visible and NIR wavelengths, Macromolecules 49 (2016) 3274. https://doi.org/10.1021/acs.macromol.6b00542

[43] N. Asai, Y. Inoue, H. Sugimura, O. Takai, Electrochromic Reaction of InN Thin Films, J. Electrochem. Soc. 146 (1999) 2365. https://doi.org/10.1149/1.1391942

[44] N. Takahashi, K. Terada, T. Nakamura, Atmospheric pressure chemical vapor deposition of tin nitride thin films using a halide source, J. Mater. Chem. 10 (2000) 2835. https://doi.org/10.1039/B005032F

[45] O. Bohnke, C. Rousselot, P. A. Gillet, C. Truche, Gel Electrolyte for Solid-State Electrochromic Cell, J. Electrochem. Soc. 139 (1992) 1862. https://doi.org/10.1149/1.2069512

[46] K.-C. Ho, H.-C. Lua, H.-F. Yua, Chapter 12: Viologens-based Electrochromic Materials and Devices, in Electrochromic Smart Materials: Fabrication and Applications (2019) pp.372-405. https://doi.org/10.1039/9781788016667-00372

[47] L. Meunier, F.M Kelly, C. Cochrane, V. Koncar, Flexible displays for smart clothing : Part II — Electrochromic displays, Indian J Fibre Text Res. 36 (2011) 429. http://hdl.handle.net/123456789/13238

[48] S.A Sapp, G.A. Sotzing, J.R. Reynolds, High contrast ratio and fast-switching dual polymer electrochromic Devices Chem Mater, 10 (1998) 2101. https://doi.org/10.1021/cm9801237

[49] W. Zhang, H. Li, M.A. -Hussein, A.Y. Elezzabi, Electrochromic battery displays with energy retrieval functions using solution-processable colloidal vanadium oxide nanoparticles, Adv. Opt. Mater. 8 (2019) 1901224. https://doi.org/10.1002/adom.201901224

[50] A. Ghicov, H. Tsuchiya, R. Hahn, J.M. Macak, A.G. Muñoz, P. Schmuki, TiO_2 nanotubes: H^+ insertion and strong electrochromic effects, Electrochem. commun. 8

(2006) 528. https://doi.org/10.1016/j.elecom.2006.01.015
[51] S.K. Deb, J.A. Chopoorian, Optical properties and color-center formation in thin films of molybdenum Trioxide, J. Appl. Phys. 34 (1966) 4818. https://doi.org/10.1063/1.1708145
[52] A. Kraft, M. Rottmann, K.-H. Heckner, Large-area electrochromic glazing with ion-conducting PVB interlayer and two complementary electrodeposited electrochromic layers, Sol. Energy Mater. Sol. Cells 90 (2006) 469. https://doi.org/10.1016/j.solmat.2005.01.019
[53] A. Simonov, T.D. Baerdemaeker, H.L.B. Boström, M.L.R. Gómez, H.J. Gray, D. Chernyshov, A. Bosak, H.-B. Bürgi, A.L. Goodwin, Hidden diversity of vacancy networks in Prussian blue analogues, Nature 578 (2020) 256. https://doi.org/10.5287/bodleian:8JB5XgybE
[54] L.E. Kreno, K. Leong, O.K. Farha, M. Allendorf, R.P.V. Duyne, J.T. Hupp, Metal–organic framework materials as chemical sensors, Chem. Rev. 112 (2012) 1105. https://doi.org/10.1021/cr200324t
[55] K. Hurlbutt, S. Wheeler, I. Capone, M. Pasta, Prussian blue analogs as battery materials, Joule 2 (2018) 1950. https://doi.org/10.1016/j.joule.2018.07.017
[56] K.-C. Chen, C.-Y. Hsu, C.-W. Hu, K.-C. Ho, A complementary electrochromic device based on Prussian blue and poly(ProDOT-Et_2) with high contrast and high coloration efficiency Sol. Energy Mater. Sol. Cells 95 (2011) 2238. https://doi.org/10.1016/j.solmat.2011.03.029
[57] C.-F. Lin, C.-Y. Hsu, H.-C. Lo, C.-L. Lin, L.-C. Chen, K.-C. Ho, A complementary electrochromic system based on a Prussian blue thin film and a heptyl viologen solution, Sol. Energy Mater. Sol. Cells 95 (2011) 3074. https://doi.org/10.1016/j.solmat.2011.06.037
[58] S. Hara, H. Shiozaki, A. Omura, H. Tanaka, T. Kawamoto, M. Tokumoto, M. Yamada, A. Gotoh, M. Kurihara, M. Sakamoto, Color-switchable glass and display devices fabricated by liquid processes with electrochromic nanoparticle "Ink", Appl. Phys. Express, 1 (2008) 104002. https://doi.org/10.1143/APEX.1.104002
[59] S.-F. Hong, L.-C. Chen, Nano-Prussian blue analogue/PEDOT:PSS composites for electrochromic windows, Sol. Energy Mater. Sol. Cells 104 (2012) 64.

https://doi.org/10.1016/j.solmat.2012.04.032
[60] M. Ishizaki, M. Sakamoto, H. Tanaka, T. Kawamoto, M. Kurihara, Synthesis of water-dispersible copper hexacyanoferrate nanoparticles and electrochromism of the thin films, Mol. Cryst. Liquid Cryst. 539 (2011) 18. https://doi.org/10.1080/15421406.2011.566024
[61] S. Pahal, M. Deepa, S. Bhandari, K.N. Sood, A.K. Srivastava, Electrochromism and redox switching of cobalt hexacyanoferrate–polyaniline hybrid films in a hydrophobic ionic liquid, Sol. Energy Mater. Sol. Cells 94 (2010) 1064. https://doi.org/10.1016/j.solmat.2010.02.027
[62] J.-Y. Wang, C.-M. Yu, S.-C. Hwang, K.-C. Ho, L.-C. Chen, Influence of coloring voltage on the optical performance and cycling stability of a polyaniline–indium hexacyanoferrate electrochromic system, Sol. Energy Mater. Sol. Cells 92 (2008) 112. https://doi.org/10.1016/j.solmat.2007.02.028
[63] Z. Jiao, J. L. Song, X. W. Sun, X. W. Liu, J. M. Wang, L. Ke, H. V. Demir, A fast-switching light-writable and electric-erasable negative photoelectrochromic cell based on Prussian blue films, Sol. Energy Mater. Sol. Cells 98 (2012) 154. https://doi.org/10.1016/j.solmat.2011.10.030
[64] Y. Rong, S. Kim, F. Su, D. Myers, M. Taya, New effective process to fabricate fast switching and high contrast electrochromic device based on viologen and Prussian blue/antimony tin oxide nano-composites with dark colored state, Electrochim. Acta 56 (2011) 6230. https://doi.org/10.1016/j.electacta.2011.02.110
[65] H. Kamioka, Y. Morimoto, W. Kosaka, S. Ohkoshi, Charge-transfer dynamics in cyano-bridged M_A–Fe system (M_A=Mn, Fe, and Co), J. Phys. Soc. Jpn. 77 (2008) 093710. https://doi.org/10.1143/jpsj.77.093710
[66] M. Ishizaki, K. Kanaizuka, M. Abe, Y. Hoshi, M. Sakamoto, T. Kawamoto, H. Tanaka, M. Kurihara, Preparation of electrochromic Prussian blue nanoparticles dispersible into various solvents for realisation of printed electronics, Green Chem. 14 (2012) 1537. https://doi.org/10.1039/C2GC35079C
[67] C.-W. Hu, K.-M. Lee, R. Vittal, D.-J. Yang, K.-C. Ho, A high contrast hybrid electrochromic device containing PEDOT, heptyl viologen, and radical provider TEMPO, 157 (2010) 75. https://doi.org/10.1149/1.3428711

[68] K. Madasamy, D. Velayutham, V. Suryanarayanan, M. Kathiresan, K.-C. Ho, Viologen-based electrochromic materials and devices, J. Mater. Chem. C 7 (2019) 4622. https://doi.org/10.1039/C9TC00416E
[69] M. Fabretto, K. Zuber, C. Hall, P. Murphy, H.J. Griesser, The role of water in the synthesis and performance of vapour phase polymerised PEDOT electrochromic devices, J. Mater. Chem. 19 (2009) 7871. https://doi.org/10.1039/B912324E
[70] J. Wei, X. Chu, X.-Y. Sun, K. Xu, H.-X. Deng, J. Chen, Z. Wei, M. Lei, Machine learning in materials science, Infomat. 1 (2019) 338. https://doi.org/10.1002/inf2.12028

Chapter 2

Experimental Methods

2. 1 Particle-size classification

When no energy is applied to a suspension in which different substances are mixed, the dense substance slowly sinks to the bottom under the influence of gravity, and the low-density substance slowly moves upward to separate[1]. This process is called precipitation. Substances with such a density difference cause sedimentation by gravity and can be separated according to the density difference over time. By artificially increasing the gravity acting on the suspension, sedimentation can be accelerated. In this case, centrifugal force can be used to accelerate the sedimentation phenomenon. This process is called centrifugation. The magnitude of centrifugal force can be defined by the following equation[2].

$$F_{centerfugal} = m \times \frac{V^2}{r} \tag{2-1}$$

where, object of mass *m*, a circular path or radius *r*, and angular velocity *V*.

Thus, the magnitude of the centrifugal force can be controlled by adjusting the angular velocity. Angular velocity is expressed in units called rpm, which is a unit that indicates how many revolutions per minute. Since the rotation radius of the material to be centrifuged varies depending on the location of the rotor, which is the place where the object is placed, the unit G is mainly used instead of rpm considering the angular velocity and the rotation radius (1G is a force equal to gravity, 10G is 10 times the force of gravity) power). Centrifugation is a common technique (Figure 2. 1) used to separate solid particles dispersed in a liquid medium (blood cells, dispersion solutions, etc.).

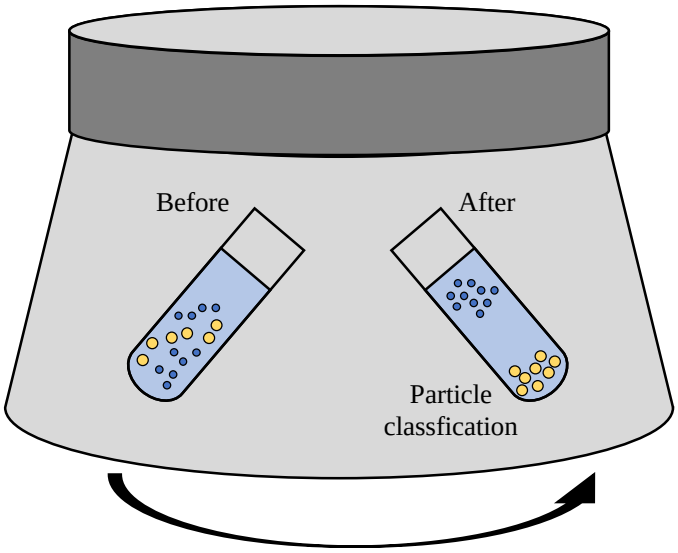

Figure 2. 1 Particle-size classification process using centrifugation.

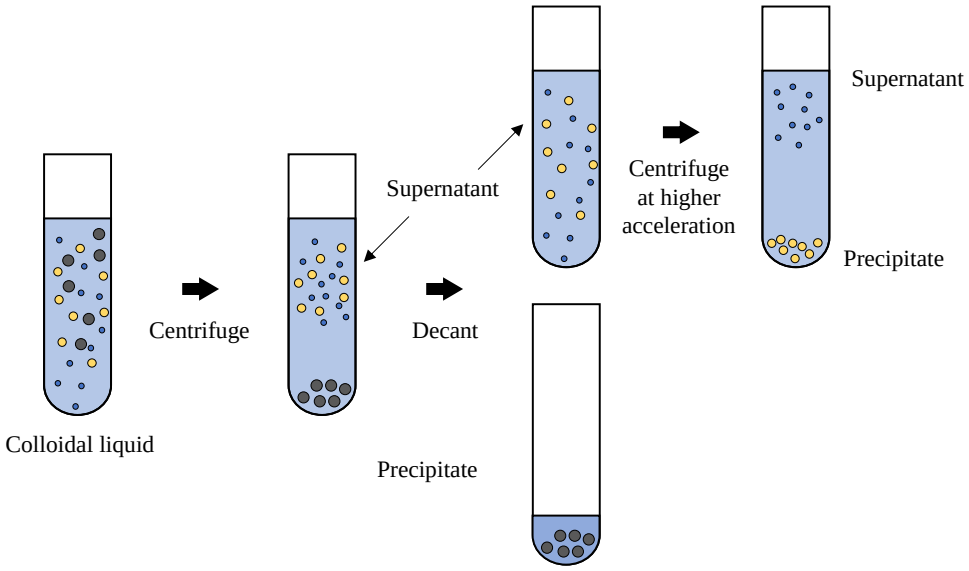

Figure 2. 2 Centrifugal processes for general colloidal liquids.

2. 2 Particle size measurements

Dynamic light scattering (DLS) is a method of analyzing the molecular weight, size, shape, etc. of polymer or colloidal particles using light scattering[3]. Particles dispersed in a solution generally have Brownian motion, and the movement of the particles becomes slower as the particle size increases and becomes faster as the particle size decreases. Using this principle, when laser light is irradiated to particles that are in Brownian motion, the scattered light from the particles shows a shake corresponding to the particle size (Figure 2. 3).

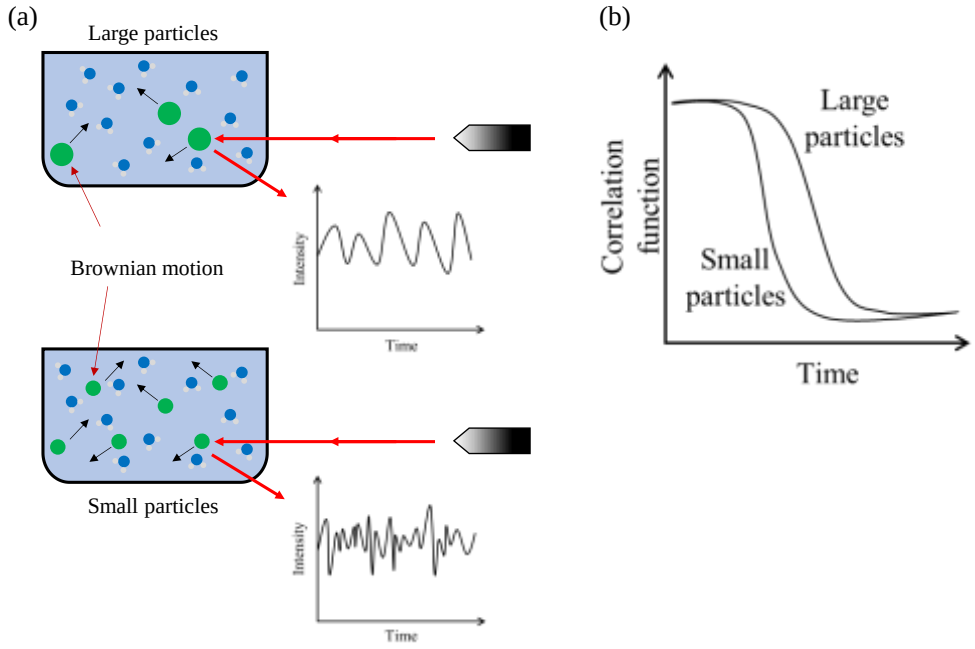

Figure 2. 3 (a) Schematic representation of Brownian motion and (b) the relationship of the correlation function with time.

That is, by detecting the change in the intensity of scattered light over time, the molecular weight can be known using an appropriate model for the relationship between the particle sizes, and further, the molecular weight distribution can be measured. The change or fluctuation of the intensity of scattered light is important information about the motion of the particle, and the time required for the fluctuation is determined by the dynamics of the particle. The translational diffusion coefficient *D*, which is an important

constant for understanding particle motion, is expressed by the Stokes-Einstein relation when the particle is spherical as follows[4]:

$$D = \frac{k_B T}{\pi \eta \gamma} \tag{2-2}$$

where k_B is Boltzmann's constant, T is temperature, η is dynamic viscosity, D is the translational diffusion coefficient, and γ is the hydrodynamic diameter.

2. 3 Colloidal stability

The zeta potential or ζ potential is the physical property of all particles in a suspension[5]. When the fine particles suspended in the liquid phase come into contact with a polar solvent, they are charged on the surface by 1) dissolution of constituent ions, 2) surface of ionization, 3) isomorphous substitution, and 4) specific adsorption of ion. The oppositely charged ions in the solution are attracted to the particle surface and the identically charged ions are repelled. At this time, an electrical double layer occurs within a certain distance between the particle and the liquid (Figure 2. 4). As the distance from the charged particle surface to the liquid phase increases, the distribution of oppositely charged ions and identically charged ions becomes equal, resulting in neutralization. On the other hand, when a voltage is applied to a suspension in which charged particles are dispersed, the particles have a velocity due to a potential difference, and this velocity is called electrophoretic mobility (EM). When a particle moves with speed, the double layer arranged around the particle is divided into a moving part (inside the stern layer) and a non-moving layer. This interface is called a shear layer (or slippage plane), and the observed potential at this plane is the zeta potential[6].

The zeta potential value indicates the stability of the dispersed suspension. For example, an emulsion that is electrically stabilized exhibits a high negative or positive zeta potential, whereas an emulsion with a low zeta potential coagulates or aggregates, resulting in poor dispersibility. Therefore, emulsions with a high zeta potential have a relatively stable system with the face repulsion force exceeding the attractive force. ZP values are typically in the range of +100 to −100 mV and the colloidal states were described in Table 2. 1[7].

Table 2. 1 Colloidal stability of particles as a function of zeta potential values[8,9].

Zeta potential (mV)	Colloidal stability
0 to ±5	Rapid coagulation or flocculation
±10 to ±30	Incipient instability
±30 to ±40	Moderate stability
±40 to ±60	Good stability
More than ±60	Excellent stability

The magnitude of ZP gives a prediction of colloidal stability. ZP of NPs with values >+25 mV or <−25 mV usually have a high degree of stability. Lower dispersions ZP values will lead to aggregation, coagulation, or flocculation due to van der Waals interparticle attraction[10].

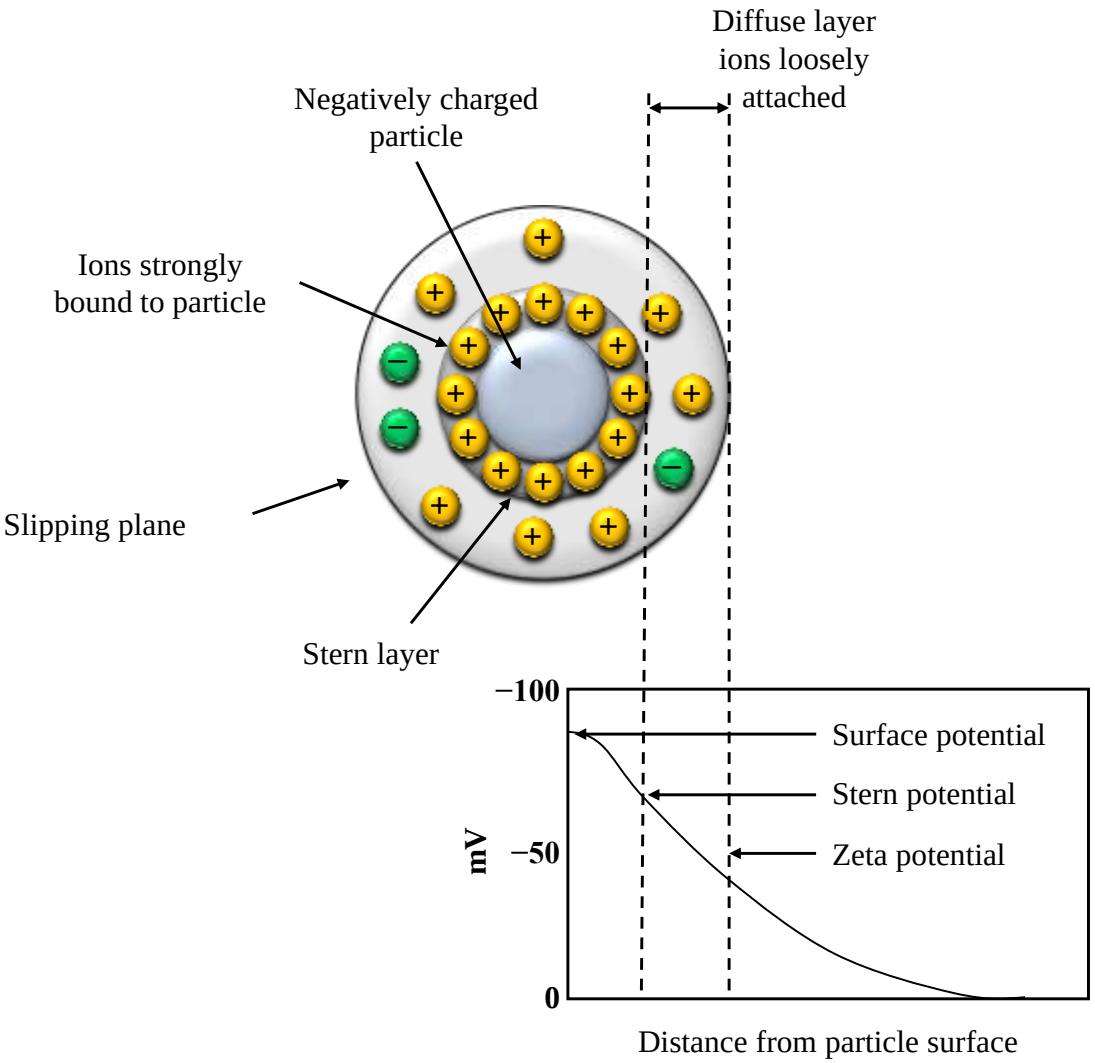

Figure 2. 4 Schematic representation of zeta potential.

2. 4 Viscosity

Viscosity is a basic physical quantity that expresses the ease of flow of a fluid. For example, viscosity is an important parameter for understanding the physical properties of liquids, and it is necessary to optimally set and manage viscosity for product research and development and quality control in a wide range of industrial fields such as paints, chemistry, pharmaceuticals, cosmetics, and foods. Especially, viscosity is an important parameter that determines the thickness in the thin film manufacturing process using wet coating methods such as spin coating. When the detection terminal driven by piezoelectric ceramic is immersed in the liquid, the vibration is attenuated in proportion to the viscosity. The change in vibration is detected by the accelerometer and displayed as a viscosity value. The detection terminal using a piezoelectric ceramic actuator is vibrated in the rotational direction so that it becomes a resonance state at a constant frequency, the tip (detection terminal) is immersed in the liquid, and the amplitude of the vibration changes depending on the magnitude of the liquid viscosity. It is a vibrating meter that captures this as a change in angular acceleration with a piezoelectric accelerometer and converts it into an electrical signal for measurement.

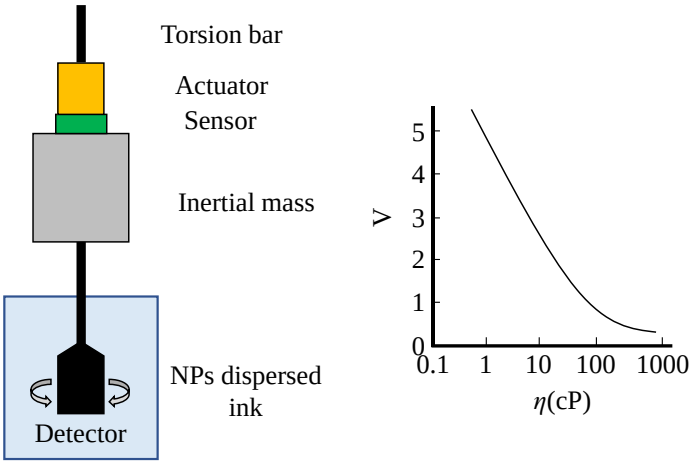

Figure 2. 5 Schematics and principle of viscometer.

2. 5 Surface treatments

1) Plasma surface treatment

When an electric field is applied between the two electrodes, electrons are emitted from the cathode to the anode, and these electrons are accelerated by the electric field and collide with surrounding N_2 and O_2 molecules. When electrons of sufficient energy (tens to hundreds of eV) collide with air molecules, the air molecules are ionized to form plasma. These electrons finally collide with the substrate between the two discharge electrodes to charge the substrate surface. At this time, if the energy of the colliding electrons is large enough (above several tens of eV), the surface molecules are broken and activated. Since the activated surface molecules have an unstable molecular structure, the property of bonding with other substances (chemical activity) becomes very strong (Figure 2. 6).

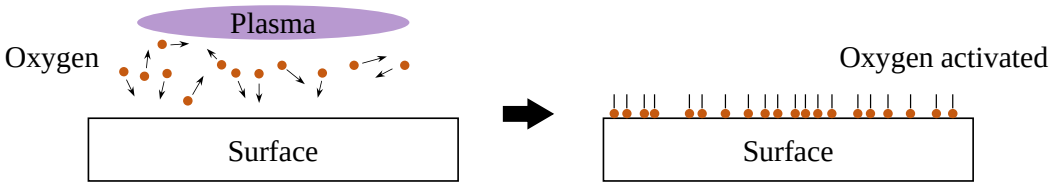

Figure 2. 6 Schematic of the plasma surface treatment

This plasma chemically bonds with the active molecules on the surface of the product to change the molecular structure of the surface. A surface modification method that lowers the surface tension (formation of a hydrophobic surface) through this process is sometimes referred to as plasma surface modification[11].

Figure 2. 7 shows an example of the change in the contact angle of water droplets before and after surface (hydrophilization) treatment.

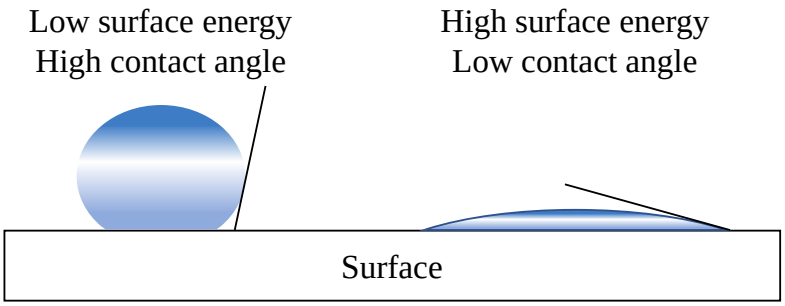

Figure 2. 7 The contact angle changes according to the surface energy.

2) UV surface treatment

The dry-cleaning method using UV is one of the representative dry-cleaning methods that have been introduced and utilized in the actual process as a method that has recently received a lot of attention. The organic matter removal mechanism using UV/O_3 is as follows[12].

$$Organic\ \ compounds + hv \rightarrow Exited\ \ organic\ \ compounds\ \ (200\sim300\ \ nm\ \ UV)$$
$$O_2 + hv \rightarrow 2O(184.9\ \ nm\ \ UV)$$
$$O + O_2 \rightarrow O_3$$
$$O_3 + hv \rightarrow O + O_2(243.7\ \ nm\ \ UV)$$
$$Exited\ \ organic\ \ compounds + (O, O_3) \longrightarrow volatile\ \ compounds$$

Oxygen molecules are decomposed into oxygen atoms by ultraviolet rays, the decomposed oxygen atoms combine with oxygen molecules to produce ozone, and the generated ozone is again decomposed into oxygen atoms and molecules by ultraviolet rays. The concept of the UV/O_3 method is to change and remove organic pollutants excited by oxygen atoms and ozone generated in this way into volatile compounds. In order to obtain such an organic matter removal effect, wavelengths of 184.9 nm (Absorbed by O_2 and organic molecules) and 253.7 nm (Absorbed by O_3 and organic molecules) should be used (Figure 2. 8).

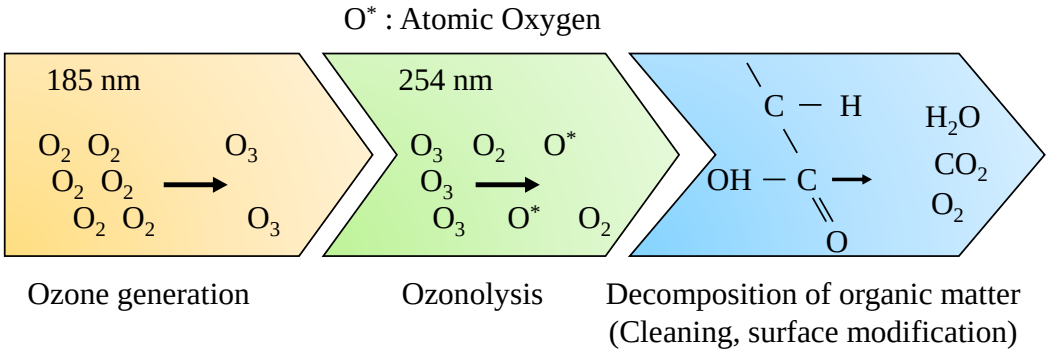

Figure 2. 8 Schematics of UV/O_3 treatments

Surface cleaning with ozone removes organic matter and moisture generated on the surface of glass, film, and metal, and improves the adhesion between the substrate and the coating thin film by modifying the surface of the material to be hydrophilic. In addition, since the energy is small compared to atmospheric pressure plasma or vacuum plasma, the surface treatment can be performed without damage.

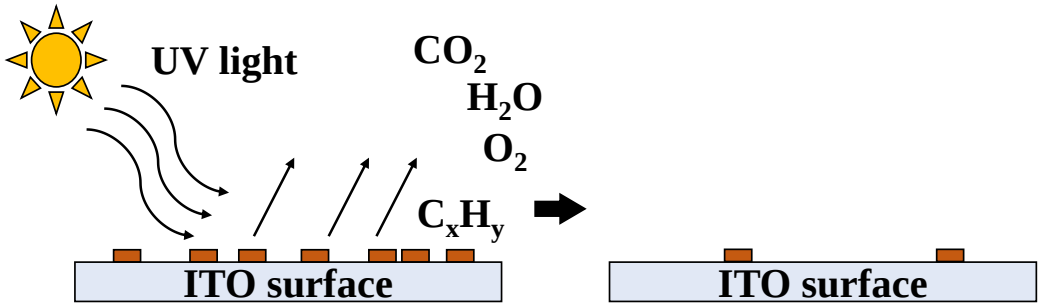

Figure 2. 9 Mechanism of UV/O_3 surface treatment.

2. 6 Film preparation

1) Spin coating methods

Spin coating is a method of manufacturing a thin film using centrifugal force generated by dropping a coating solution on a generally flat substrate surface and rotating it at high speed. Spin coating is a type of wet process coating that dries the liquid phase. Although it is limited to flat-coated objects, it is possible to produce simple and uniform thin films. Thin-film production is divided into three major processes as shown in Figure 2. 10.

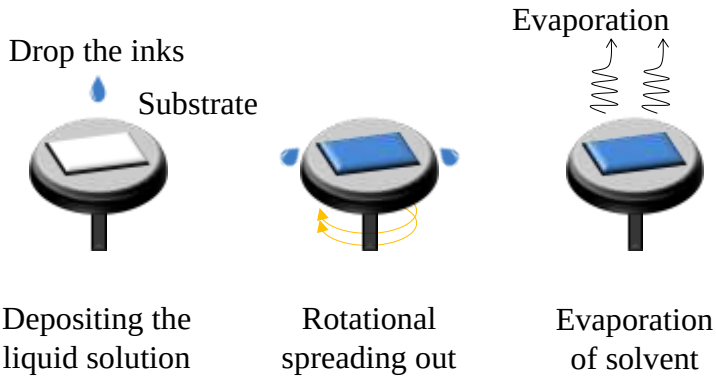

Figure 2. 10 Spin-coating processes of film preparation

2. 1) Preparation of substrate and dropping of the coating solution

The target is vacuum-adsorbed and fixed on the stage of the spin coater, and the coating solution is dropped near the center. The amount of dropping depends on the size of the object to be applied, but it is very small, ranging from several CCs to several tens of CCs.

2. 2) Rotation treatment process

Rotate the stage to gradually increase the rotation speed and remove the coating solution by centrifugal force. As the coating solution is removed by centrifugal force,

the viscosity increases, and the coating solution becomes immobile. The higher the rotation speed and the longer the time, the thinner the thin film can be produced.

2. 3) Drying/curing process

After the rotation treatment process, the substrate is removed from the spin coater, and the solvent is removed, or UV cured using a hot air drying furnace or UV curing device to prepare a thin film.

Assuming that the liquid on the rotating substrate is balanced by centrifugal and viscous forces, the thickness of the spin-made thin film can be calculated from Newton's law of viscosity[13-16].

$$h = e_0/(1 + \frac{4\omega^2 {h_0}^2 t}{3\eta})^{\frac{1}{2}} \quad (2\text{-}3)$$

where, h is the film thickness, η is viscosity of the liquid solution, h_0 is initial film thickness, ω is the angular velocity (spin speed), and t is spin time.

2. 7 Adhesion test

1) Scratch test

The scratch test is a method of measuring the critical load (L_c) when the film is cracked or peeled by moving the substrate while increasing the load on the surface of the thin film using a stylus. This method is allowed simple and fast analysis, and it can be applied to thin films with several hundred nm or less. In addition, it has an advantage that adhesion strength can be quantified[17].

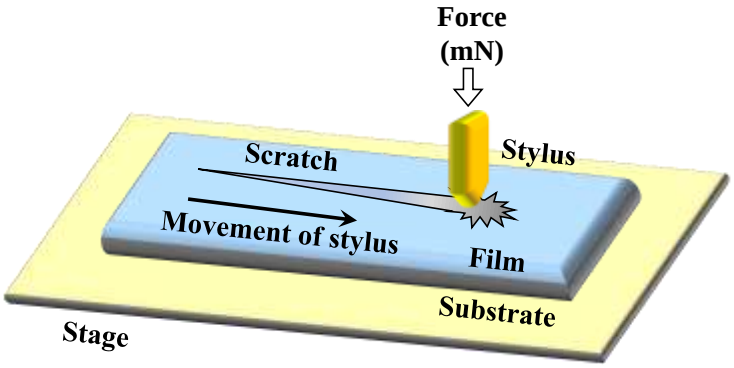

Figure 2 .11 A schematic illustration a scratch test on a coated film

Figure 2. 12 shows a typical plots of scratch test data experiment. As the load increases, the delamination of material coated on the substrate is observed, and the force at which the deformation of the peak is observed is the adhesion strength.

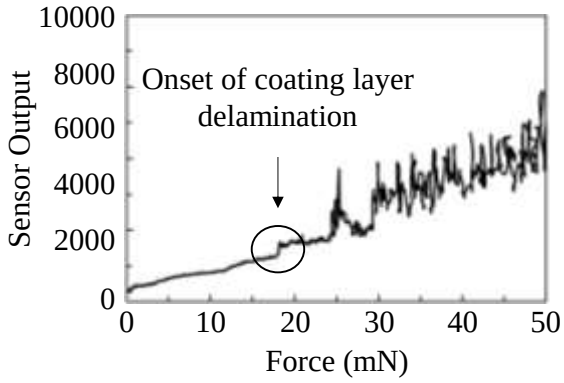

Figure 2. 12 Typical scratch test data plots.

2) Crosscut test

cross-cut test method is a test that examines the adhesion, which is the important quality performance of the coating. A rectangular grid pattern is applied to the coating film to evaluate the peel resistance of the coating film from the substrate using an adhesive tape with a set standard (Japanese Industrial Standards: JIS Z 1522 was used in this study) as shown in Figure 2. 13.

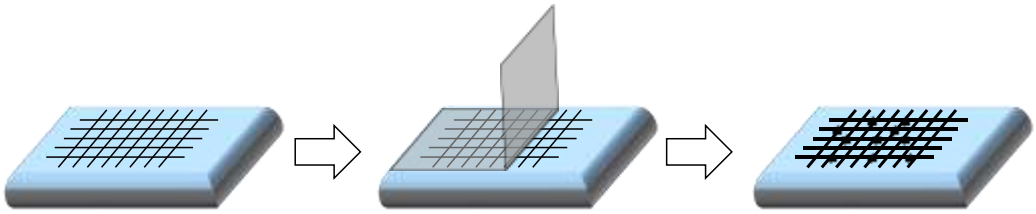

Figure 2. 13 Schematics of crosscut test

Adhesion is evaluated by observing the surface condition of the tested thin film through an optical microscope.

2. 8 Crystal structure

1) X-Ray Diffraction

X-ray diffraction is the most representative method for interpreting the crystal structure, and it can be used for a wide range of fields such as metals, organic and inorganic compounds, and biomaterials because non-destructive measurement is possible. X-ray diffraction is an indirect phenomenon that occurs when a crystal acts as a diffraction grating for X-rays. A crystal is a solid in which atoms are arranged with periodicity in three-dimensional space. Therefore, inside the crystal, electrons are distributed as a density function with the same periodicity as the arrangement of atoms. When X-rays are irradiated to the crystal, some of the X-rays undergo coherent scattering with electrons. Consistent scattering is a phenomenon in which X-ray photons are scattered without losing energy. Consistent scattering of X-rays has indirection. Therefore, when X-rays are incident in a specific direction related to the periodicity of the electron density function, X-rays are propagated with strong intensity in a specific direction by superposition of waves. This phenomenon is called X-ray diffraction. Since X-ray diffraction is a phenomenon that occurs because the atomic arrangement of a crystal has periodicity, X-ray diffraction can be used to analyze the crystal structure. Figure 2. 14 shows the Bragg conditions for X-ray diffraction to occur in the crystal. where d is the interplanar spacing and λ is the wavelength. When parallel X-rays are incident on a crystal plane at an angle θ, in order for the reflected beams to appear as a single beam of sufficient intensity, they must be in phase with each other, and the path difference between the interfering beams must be an integer multiple of the wavelength. The path difference between the two beams can be expressed by Bragg's equation as follows[18].

$$n\lambda_x = 2d \cdot sin\theta \quad (2\text{-}4)$$

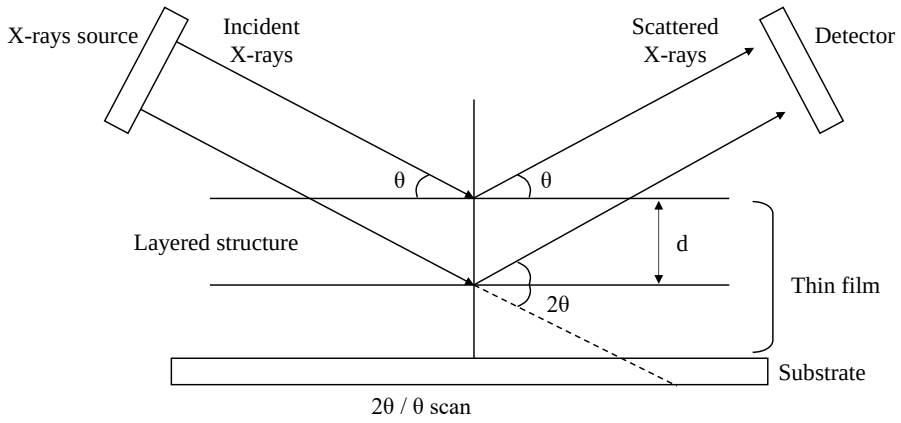

Figure 2. 14 Incident X-Rays are diffracted by the layers of atoms in a crystalline material.

2. 9 Chemical composition state

1) X-ray photoelectron spectroscopy

X-ray photoelectron spectroscopy (XPS) makes it possible to measure the electrons emitted in an interval of energy according to the binding energy of the electrons. Each chemical element is characterized by a single spectrum, this spectroscopic method makes it possible to precisely analyze the chemical nature of a given material[19].

XPS method is based on photoionization. The surface of the examined sample is excited by monoenergetic x-ray photons in the range of 150-1500 eV and the emitted photoelectrons are detected separated according to their energy. The primary photon energy is large enough to extract electrons even from the inner atomic electron shells thus ionizing the atoms of the surface. The penetration depth of photons is between 1-10 μm, but electrons - due to their large inelastic scattering cross section causing multiple scattering process - can leave the surface only from the few topmost atomic layers (Figure 2. 15). X-ray photons can excite electrons from the valence band in the range of 0-25 eV and from atomic core levels with binding energy in the range of 25-1500eV. In this way XPS is suitable for characterizing electron structure of the surface. The X-ray photon excitation gives rise to photoelectron emission according to the equation[20]:

$$KE = h\nu - BE - \varphi_{spectrometer} \quad (2\text{-}5)$$

where $h\nu$ represents the energy of the absorbed photon, BE is binding energy of an electron referenced to Fermi level attracted to a nucleus, and $\varphi_{spectrometer}$ is the work function of the spectrometer. In the above equation, the energy of exciting radiation is known, $\varphi_{spectrometer}$ can be calibrated to the energy of a well-known photoelectron peak of a precious metal standard, and the value of KE is measured (Figure 2. 15). Thus, BE can be calculated. This characteristic energy enables the identification of the surface element, and in this way, the composition of the sample surface can be determined.

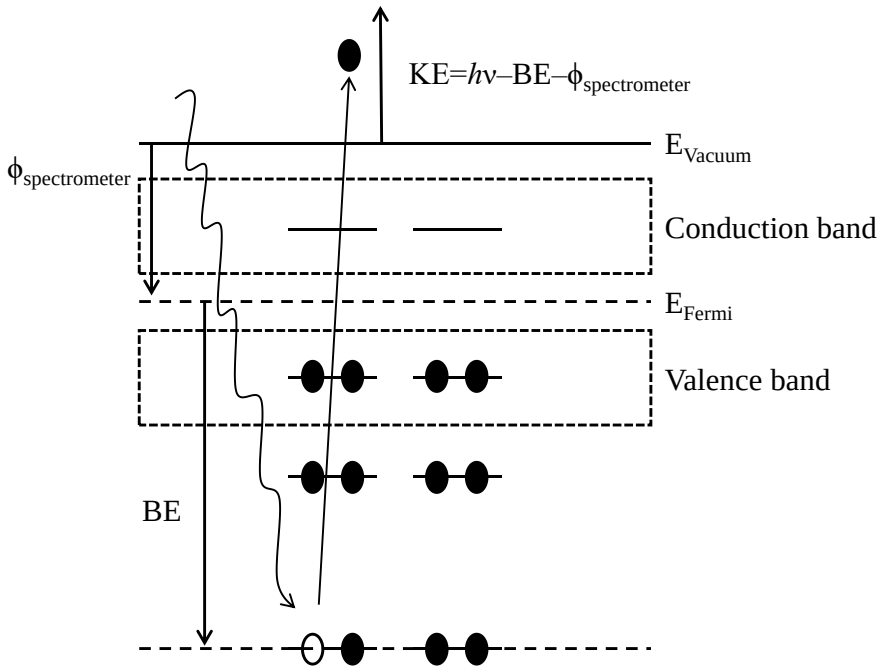

Figure 2. 15 Schematic diagram of a core-level-photoelectron emission process[21].

In XPS two materials are used most often as anodes in soft X-ray sources: magnesium and aluminum. The Mg Kα and Al Kα lines have sufficiently narrow widths (0.7 eV and 0.8eV respectively) so a good resolution can be achieved, and the line energies (1253.6 eV and 1486.3 eV) are also high enough for the detection of all elements[22]. The large intensity of the Mg Kα and Al Kα lines provides high sensitivity measurements.

All XPS analyzes were completed using a PHI 5000 VersaProbe. A simplified diagram of the main components of the XPS instrument is shown in Figure 2. 16.

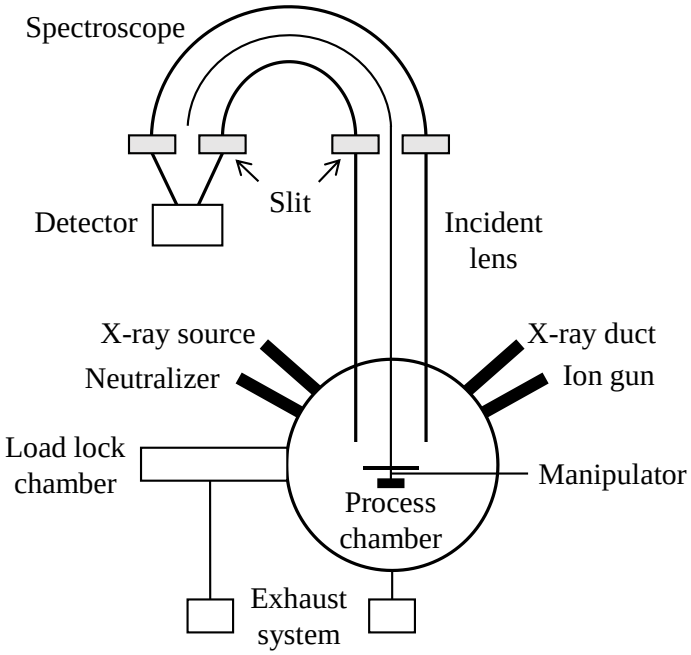

Figure 2. 16 Schematic of XPS system

2) Energy dispersive X-ray spectrometer (EDX)

Energy-dispersive X-ray spectroscopy (also known as EDS, EDX, or EDXA) is a powerful technique that enables the user to analyze the elemental composition of the desired sample[36]. EDS is a method of analyzing the components and composition of components of a sample from characteristic X-rays generated by irradiating accelerated electrons to the sample. This analysis method is widely used for the analysis of sample components because it can non-destructively analyze the sample, quantitative analysis is possible, and the analysis speed is fast. Figure 2. 17 shows the principle of generation of characteristic X-rays. When electrons collide with a sample by accelerating them with a high voltage, secondary electrons are generated in the electron shell. This creates a hole in the electron shell. Then, the electrons in the upper orbital transition to the hole to be thermodynamically stable. In this process, energy is generated in the form of X-rays as much as the gap between the two electron orbitals. EDS is a measurement method that enables qualitative analysis of samples by measuring this energy. Since every atom has a different value for X-ray energy, it is possible to distinguish all atoms by X-ray energy.

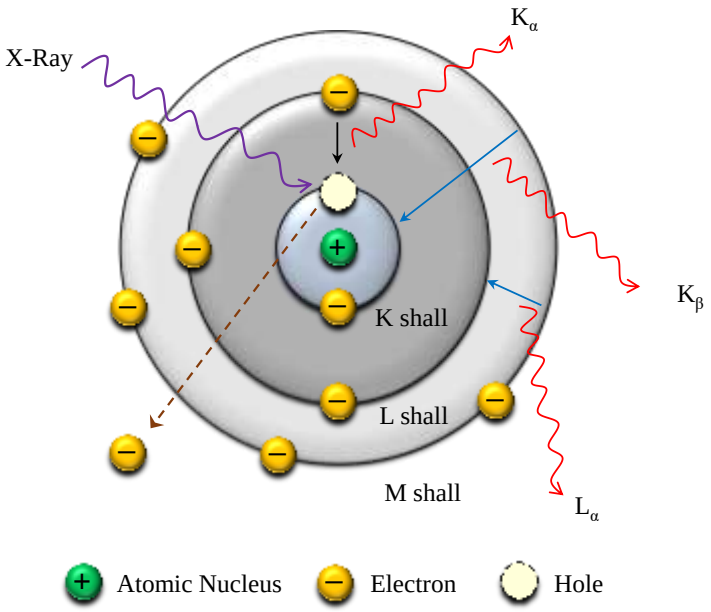

Figure 2. 17 Illustration of the principle of EDX.

2. 10 Film morphology and thickness

1) Field emission scanning electron microscope

Field emission scanning electron microscopy (FE-SEM) is used to observe the morphology of the sample surface from low to high magnification. In FE-SEM observation, it is possible to observe at a higher magnification than a scanning electron microscope (SEM)[24].

The principle of FE-SEM is that an electron beam generated from an electron source is scanned two-dimensionally on a sample, and a signal generated therefrom is imaged to obtain an image as shown in Figure 2. 18. At that time, signals such as secondary electrons (SE), backscattered electrons (BSE), X-rays, fluorescence, and absorption electrons are generated from the data (Figure 2. 19)[25]. In SEM, SE is mainly used to acquire surface information, and BSE is used to acquire images with compositional information.

SE indicates that electrons in the material are excited by the incident electrons, and the retained energy is as low as several tens of eV or less regardless of the energy of the incident electrons. Therefore, the depth of occurrence of SE is as shallow as 10 nm, and thus SE brings sample surface information. BSE is an electron emitted in vacuum by backscattering after incident electrons cause a synthesis action inside the sample, and mainly has compositional information. The retained energy and the emission region are proportional to the incident energy and have information in the region as deep as the high accelerating voltage.

Conventionally, SEM was difficult to obtain surface information compared to SE because a rather high acceleration voltage (several kV or more) was required from the characteristics of the detector. However, recently, a new emission method has been developed (FE-SEM) and the observation of the BSE phase at a lower accelerating voltage has been realized. Composition information of the sample surface was obtained.

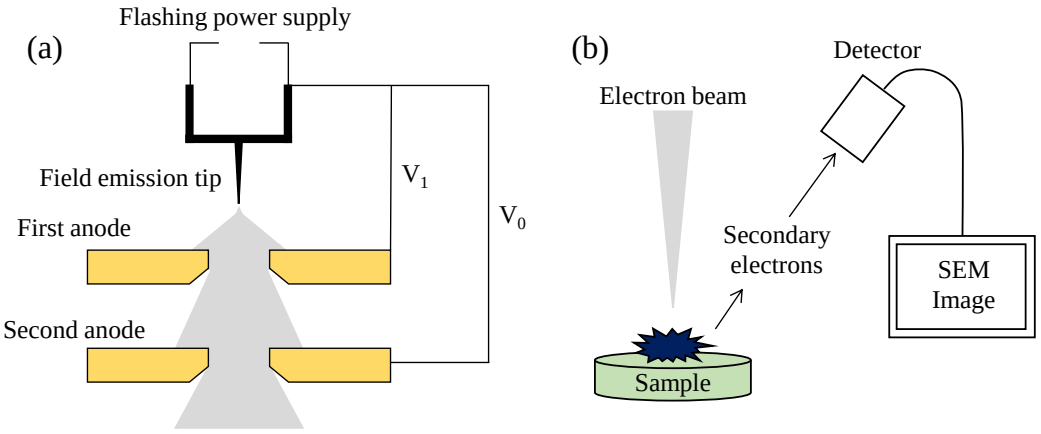

Figure 2. 18 Illustration of (a) a field emission gun structure and (b) the measurement principles for the scanning electron microscope[26].

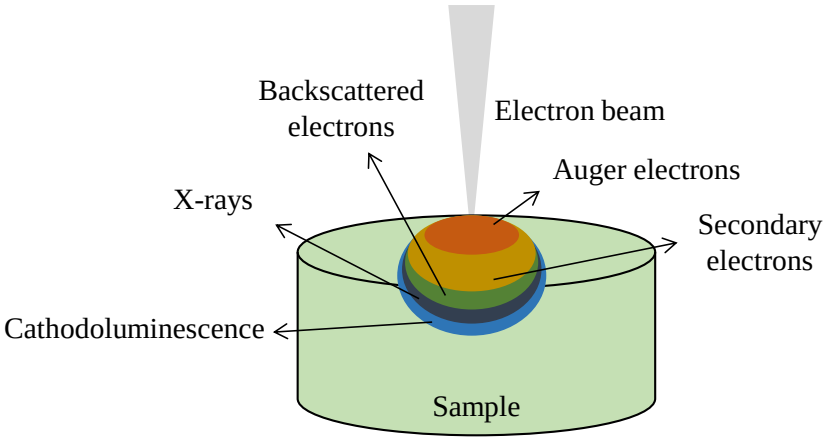

Figure 2. 19 The interaction of electron beam with specimen and the signal emitted from the sample

For observation with FESEM, the sample first needs to be made conductive to an electric current. In this case, gold or palladium is used to coat the sample surface with an extremely thin layer (1.5-3.0nm) using a sputter for the sample conductivity.

To be observed with an FESEM, objects are first made conductive for currents. This can be done by coating them with an extremely thin layer (1.5–3.0 nm) of gold or palladium[22]. The spatter coating of the sample is shown in the Figure 2. 20.

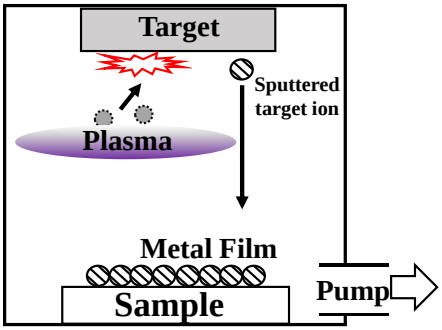

Figure 2. 20 Schematic of sputter coater for FESEM.

2. 11 Electrochemical and electrochromic properties

1) Electrochemical measurements

Recently, the electrochemical measurement method is not only used as an analytical method but is used for the measurement of the electron transfer process in development research in various fields such as new sensor development, functional film production, and new battery and capacitor material development. Therefore, it is a very important experimental method not only in the field of electrochemistry, but also in many fields such as polymers, biotechnology, inorganic chemistry, material chemistry, medicine, pharmaceuticals, and electronic engineering. Electrochemical analysis can be said to analyze the chemical response of a sample when an electrical stimulus is applied to the sample. A chemical response involves the movement of electrons (oxidation or reduction) accompanied by a substance in response to an electrical stimulus[27]. These oxidation and reduction reactions are called redox reactions. In addition, it brings a lot of information about a series of phenomena such as the concentration of active species in the sample, equilibrium constant, reaction mechanism, electron transfer reaction on the electrode surface, and adsorption. In electrochemical experiments, one or more of the four variables of potential difference (E), current (i), charge amount (Q), and time (t) are generally measured. In particular, in recent years, the development of electronic devices has been radically developed, and electrochemical measurements are also increasing in the research field, and it is widely used to systematically analyze the redox reaction, electronic state and electrochemical reaction mechanism of materials[28]. The most representatively used for measuring electrochemical properties is an electrochemical measuring method using a three-electrode cell. The electrochemical cell is composed of a working electrode (WE), which is the sample material being tested, a reference electrode (RE, typically Ag/AgCl or calomel electrodes, and a counter electrode (CE). In the three-electrode cell, current flows between the WE and the CE, and the potential of the WE are controlled by a potential regulator with reference to the RE. At this time, the potential difference between the WE and the RE can be accurately measured regardless of the current value flowing by the electrode reaction. (Figure 2. 21).

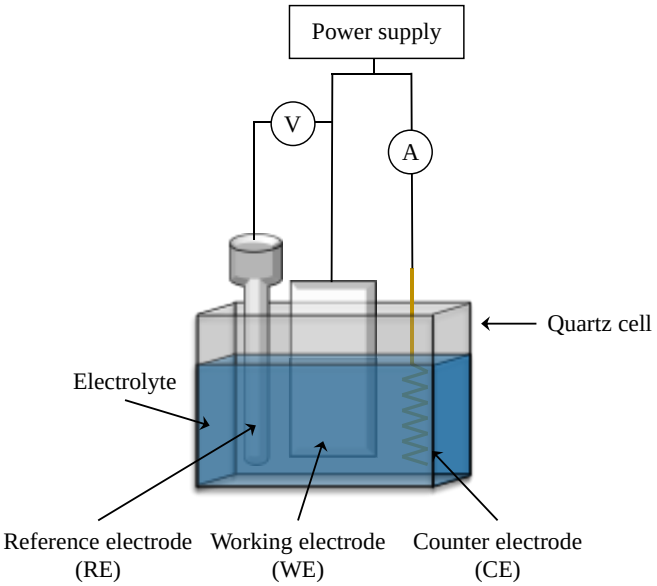

Figure 2. 21 Illustration of a three-electrode cell structure.

2) Cyclic voltammetry

Cyclic voltammetry is a method of measuring the current by circulating the potential of the working electrode at a constant speed as shown in Figure. 2. 22 (a) and a cyclic voltammogram can be obtained using this method as shown in Figure 2. 22 (b). Cyclic voltammetry is widely used as one of the methods to directly investigate what kind of reaction is taking place on the electrode surface. For measurement, a potential at which no current flows are set as the initial potential (a).

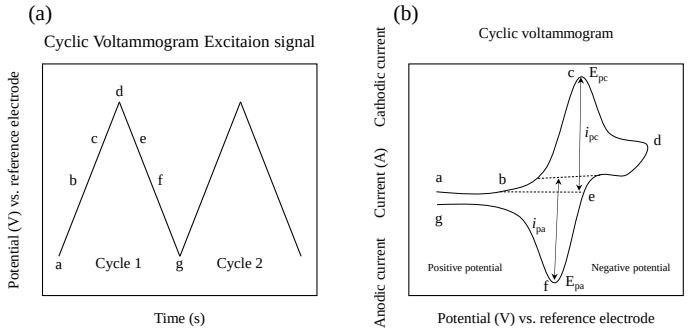

Figure 2. 22 (a) CV excitation signal and (b) voltammogram of a single electron oxidation-reduction.

It starts from the set potential and scans at a constant speed, reverses the scanning direction at the reverse potential (d), scans the potential at the same scanning speed as the forward direction, and returns to the initial potential. The single injection method (single CV) is the method of performing such a cycle once, and the method of repeating the same type of potential injection repeatedly is the multiple injection method (multiple CV). In the experiment, the initial potential and the reverse potential should be appropriately set so that the redox signal of the electrode can be observed.

The peak current, i_p, of the reversible redox process is described by the Randles-Sevcik equation. At 298 K, the Randles-Sevcik equation is[29]:

$$i_p = (2.69 \times 10^5) n^{3/2} A C D^{1/2} v^{1/2} \quad (2\text{-}6)$$

where n is the number of electrons, A the electrode area (cm^2), C the concentration ($mol \cdot cm^{-3}$), D the diffusion coefficient ($cm^2 \cdot s^{-1}$), and v the potential scan rate ($V \cdot s^{-1}$).

3) Chronocoulometry

Chronocoulometry (CC), as indicated by the name, is a technique in which the charge is measured (i.e., "coulometry") as a function of time (i.e., "chrono"). There are various types of coulometry. The one discussed here is potentiostatic coulometry in which the potential (or voltage) is set and, as a result, charge flows through the cell. As shown in Figure 2. 23 the potential is changed instantaneously from the initial potential (E_i) to the first step potential (E_f), and it is held at this value for the first step time. Next, the potential changes to the second step potential (E_s) after the first step time, and then remains at this value for the set time.

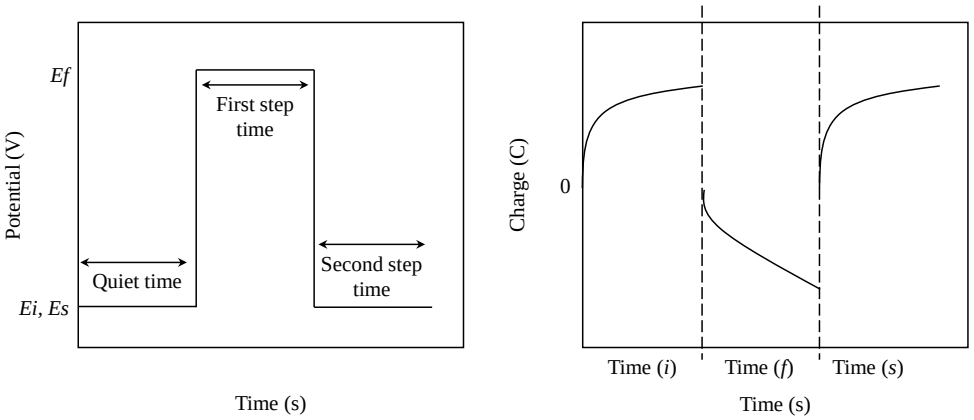

Figure 2. 23 Chronocoulometry excitation signal.

In the CC technique, the transferred charge density (Q) passing during the application of a step potential is recorded versus time. By integrating the current through the applied potential step, Q is calculated. Using Cottrell's equation, the Anson equation may be derived for chronocoulometric systems[29].

$$Q_d = 2nFAC_0{D_0}^{1/2}t^{1/2}/\pi^{1/2} \qquad (2\text{-}7)$$

where D_0 is diffusion constant for electroactive species (cm^2/s), C_0 is concentration of electroactive species (mol/cm^3), A is electrode area (cm^2), F is Faraday's constant (96.485 C/equivalent), and n is stoichiometric number of electrons involved in the reaction. CC analysis is preferred for measuring the diffusion coefficient (D) with

respect to the electrode area (A). In the reverse potential step experiment, there is the possibility for the material to be reoxidized to the original material during the reverse potential step, as a reduced form of the redox reaction during the forward step remains in the district of the working electrode[29]. According to the data obtained from the chronoamperometric technique, the signal recorded in the backward step is lower than that recorded in the forward step.

2. 12 Electrochromic measurements

1) Coloration efficiency

The coloration efficiency (*CE*) of an EC material is a critical factor for demonstrating its performance. The *CE* is defined as the change in optical density (Δ*OD*) per unit of the intercalated ionic charge (*Q*) into an EC layer. *CE* and Δ*OD* can be obtained from the following equations[30]

$$CE = \Delta OD/Q \tag{2-8}$$

$$\Delta OD = \log(\frac{T_{\lambda b}}{T_{\lambda c}}) \tag{2-9}$$

where $T_{\lambda b}$ and $T_{\lambda c}$ refer to the transmittances of the layer in its bleached and colored states, respectively.

2) Optical modulation rate

In the EC field, the color change (optical modulation) rate of the materials according to the electrochemical redox reaction is an important parameter. Transmission spectra and time-strip charts were obtained using multiple potential step (MPS) measurements, from which response times were calculated[30]. The optical modulation rate was measured by applying the potentials of colored and bleached states and was defined as the time required for the system to exhibit a 90% variation in total transmittance (Figure 2. 24).

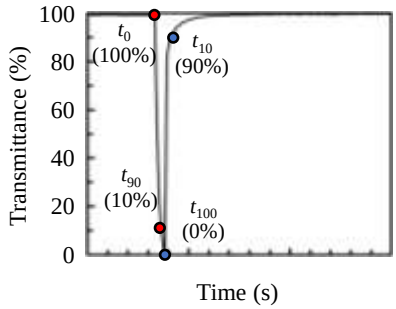

Figure 2. 24 Optical modulation rates.

2. 12 Color detail information

1) Chromaticity

Chromaticity is a color value stipulated by The International Commission on Illumination (CIE) and is a color space that can be expressed numerically in a color difference and color space that can be detected by the human eye.

In the past, digital color displays have displayed similar color spaces in Red, Green, and Blue (RGB) to the eyes of the authorized person, X, Y, and Z (CIE 1931 XYZ color space as shown in Figure 2. 25 (a))[31]. However, there is a problem that these color spaces do not match the colors perceived by humans. On the other hand, CIELAB is a color space that is currently standardized worldwide because it shows a very close difference to the eye as a uniform color space coordinate.

In CIELAB, color coordinates are expressed as L*, a*, b*. L* stands for brightness (L*=0 indicates black, L*=100 indicates diffuse white, specular white may be higher), a* stands for red and green (a *, negative for green, positive for red), and b* stands for yellow and blue (b *, negative numbers represent blue, positive numbers represent yellow)[32].

The CIE 1976 developed the L*a*b* color model in 1976 is called L*a*b* color display system or CIELAB color display system (Figure 2. 25 (b)).

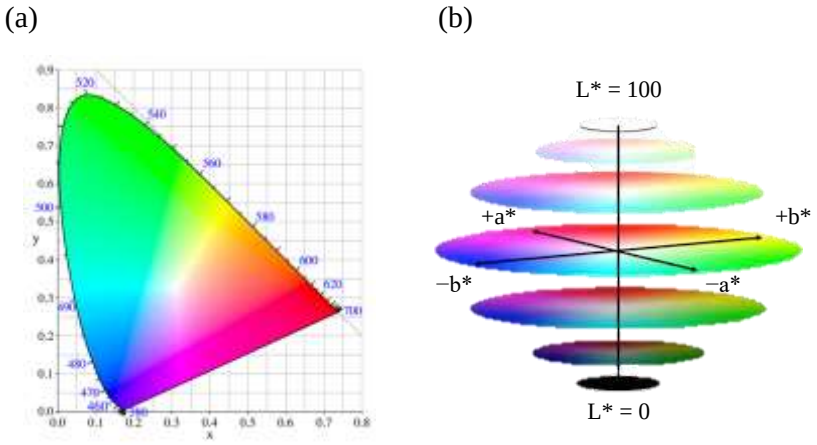

Figure 2. 25 Defining and communication color: The (a) CIE1931 XYZ and (b) CIE1976 LAB systems

2) Haze

Haze is how blurry or cloudy the appearance of a transparent material. The appearance of a transparent or translucent product is described by total transmittance, haze and clarity. They are important parameters for plastic films, glass, food packaging, LCD panel, automotive windshields and other transparent and translucent products. Total transmittance is influenced by absorption and reflection, while haze and clarity are interrelated which is influenced by the scattering of the diffused light[33]. The light before passing through the sample is called incident light, the entire light after passing through the sample is called transmitted light, and the scattered light with a scattering angle greater than 2.5 ° after the transmission sample is called scattered light, ration of the scattered light to transmitted light (as show in green color (bottom) of Figure 2. 26) and T_t is the total transmitted light (as show in pink color (top) of Figure 2. 26).

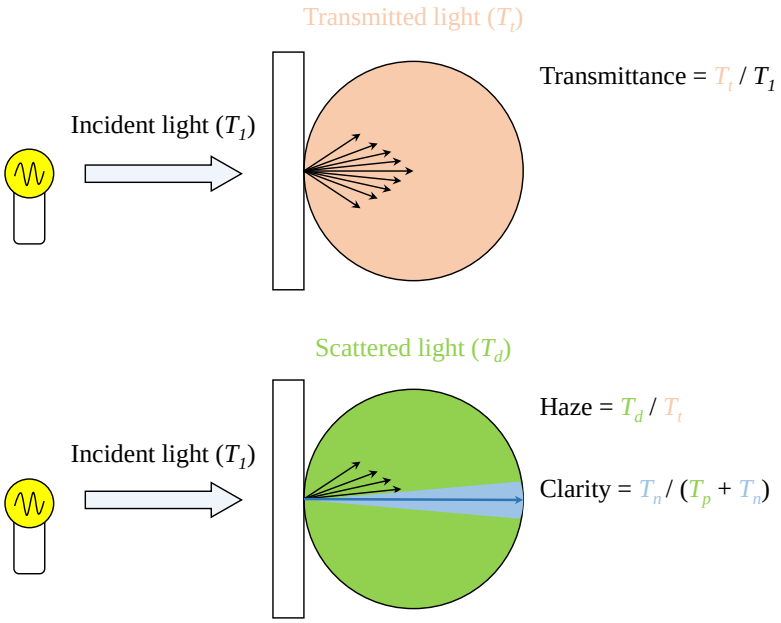

Figure 2. 26 Measurement of transmittance, haze, and clarity.

Reference

[1] F.H. Stephenson, in Calculations for Molecular Biology and Biotechnology (Second Edition), Elsevier, Academic Press, 2010, pp. 413-421.

[2] O. M. Griffith, Practical Techniques for Centrifugal Separations, THERMO FISHER SCIENTIFIC Application Guide, p.5.

[3] M.V. Lozano, M.J. Santander-Ortega, M.J. Alonso, Nanotechnology for Oral Drug Delivery, Elsevier, Academic Press, 2020, pp. 419-458.

[4] N.D. Jaeger, H. Demeyere, R. Finsy, R. Sneyers, J. Vanderdeelen, P. Meeren, M. Laethem, Part. Part. Syst. Charact. 8 (1991) 179.

[5] J. Kim, D. F. Lawler, Characteristics of zeta potential distribution in silica particles, Bull. Korean Chem. Soc. 26 (2005) 1083. https://doi.org/10.5012/bkcs.2005.26.7.1083

[6] G.V. Lowry, R.J. Hill, S. Harper, A.F. Rawle, C.O. Hendren, F. Klaessig, Ulf Nobbmann, P. Sayre, J. Rumble, Guidance to improve the scientific value of zeta-potential measurements in nanoEHS, Environ. Sci.: Nano 3 (2016) 953. https://doi.org/10.1039/C6EN00136J

[7] R. D. Letterman, Water Quality and Treatment, 5th Ed. McGraw-Hill, (New York, (1999)) sec. 6.1.

[8] R. Greenwood, K. Kendall: J. Europ. Cera. Soc. 19 (1999) 479.

[9] D. Hanaor, M. Michelazzi, C. Leonelli, C.C. Sorrell, The effects of carboxylic acids on the aqueous dispersion and electrophoretic deposition of ZrO_2, J. Europ. Cera. Soc. 32 (2012) 235. https://doi.org/10.1016/j.jeurceramsoc.2011.08.015

[10] M. Horie, K. Fujita, Advances in Molecular Toxicology, Elsevier, 2011, pp.145-178.

[11] K.-B. Lim, D.-C. Lee, Surface modification of glass and glass fibres by plasma surface treatment, Surf. Interface Anal. 36 (2004) 254. https://doi.org/10.1002/sia.1682

[12] K. Umeda, T. Miyasako, A. Sugiyama, A. Tanaka, M. Suzuki, E. Tokumitsu, T. Shimoda, Impact of UV/O_3 treatment on solution-processed amorphous $InGaZnO_4$ thin-film transistors, J. Appl. Phys. 113 (2013) 184509. https://doi.org/10.1063/1.4804667

[13] P.J. Kelly, R.D. Arnell, Magnetron sputtering: a review of recent developments and applications, Vacuum 56 (2000) 159. https://doi.org/10.1016/S0042-207X(99)00189-X

[14] Y.-Y. Huang, K.-S. Chou, Studies on the spin coating process of silica films, Ceram. Int. 29 (2003) 485. https://doi.org/10.1016/S0272-8842(02)00191-8

[15] D.B. Hall, P. Underhill, J.M. Torkelso, Spin coating of thin and ultrathin polymer films, Poly. Eng. Sci. 38 (1998) 2039. https://doi.org/10.1002/pen.10373

[16] A.G. Emslie, F.T. Bonner, L.G. Peck, Flow of a viscous liquid on a rotating disk, J. Appl. Phys. 29 (1958) 858. https://doi.org/10.1063/1.1723300

[17] N. Saba, M. Jawaid, M.T.H. Sultan, Mechanical and Physical Testing of Biocomposites, Fibre-Reinforced Composites and Hybrid Composites, Elsevier, Woodhead Publishing, 2019, pp.1-12.
[18] D.D.Le Pevelen, Encyclopedia of Spectroscopy and Spectrometry (Second Edition), Elsevier, Academic Press, 2010, pp.2559-2576.
[19] V. Chevali, E. Kandare, Biopolymers and Biotech Admixtures for Eco-Efficient Construction Materials, Elsevier, Woodhead Publishing, 2016, pp.275-304
[20] M.H. Engelhard, T.C. Droubay, Y. Du, Encyclopedia of Spectroscopy and Spectrometry (Third Edition), Elsevier, Academic Press, 2017
[21] F.A. Stevie, C.L. Donley, Introduction to x-ray photoelectron spectroscopy, J. Vac. Sci. Technol. A 38 (2020) 063204. https://doi.org/10.1116/6.0000412
[22] D.R. Baer, S. Thevuthasan, Handbook of Deposition Technologies for Films and Coatings (Third Edition), Elsevier, William Andrew, 2010, pp.749-864.
[23] B.J. Lewis, W.T. Thompson, F.C. Iglesias, Comprehensive Nuclear Materials, Elsevier, Elsevier Science, 2012, pp.515-546.
[24] A. Mayeen, L.K. Shaji, A.K. Nair, N. Kalarikkal, Characterization of Nanomaterials, Elsevier, Woodhead Publishing, 2018, pp. 335-364.
[25] N. Brodusch, H. Demers, R. Gauvin, Field Emission Scanning Electron Microscopy, Singapore, Springer, 2018, pp 13-35
[26] D.Semnani, Electrospun Nanofibers, Elsevier, Woodhead Publishing, 2017, pp.151-180.
[27] T.W. Napporn, Y. Holade, B. Kokoh, S. Mitsushima, K. Mayer, B. Eichberger, V. Hacker, Fuel Cells and Hydrogen, Elsevier, 2018, pp.175-214.
[28] A.J. Bard, L.R. Faulkner, Electrochemical Method: Fundamentals and Applications (Second Edition), JOHN WILEY & SONS, 2000, p.227
[29] Y.S. Choudhary, L. Jothi, G. Nageswaran, Spectroscopic Methods for Nanomaterials Characterization, Elsevier, 2017, pp.19-54.
[30] C. G. Granqvist, Handbook of Inorganic Electrochromic Materials, Elsevier, Amsterdam, 1995
[31] K. Jack, Digital Video and DSP, Newnes, Elsevier, 2008, pp.15-29.
[32] B.C.K. Ly, E.B. Dyer, J.L. Feig, A.L. Chien, S.D. Bino, Research techniques made simple: cutaneous colorimetry: A reliable technique for objective skin color measurement, J. Investig. Dermatol. 140 (2020) 3. https://doi.org/10.1016/j.jid.2019.11.003
[33] Y. Zheng, Z. Zhou, W. Cao, C. Li, Q. Wang, Y. Huang, S. Shen, Robust, low haze and graded porous anti-reflective glass by Tailoring the Nanostructures, Ceram. Int. 46 (2020) 18623. https://doi.org/10.1016/j.ceramint.2020.04.174

Chapter 3

Fabrication of Adhesion WO_3 Nanoparticle Dispersion Ink and Evaluation of Electrochromic Properties of WO_3 Thin Films

3. 1 Introduction

WO_3 was discovered by Deb[1] in the 1960s as a material exhibiting electrochromic properties and attracted great attention as a material for smart windows. In particular, materials using WO_3 exhibit transmittance changes in both the visible and near-infrared (NIR) regions[2], which can filter out most of the incident sunlight, potentially reducing the building's air conditioning costs. Although there are various methods for manufacturing the WO_3 thin film, the sputtering method is known most representatively among them[3]. Sputtering has several advantages, such as large-area homogeneous thin film production and continuous line production and is a suitable method for smart window manufacturing[4]. However, sputtering requires high production cost per unit area and low productivity. Recently, nanotechnology has developed rapidly in recent years due to its ability to change and adjust its chemical composition and size and attempts to fabricate EC thin films using inkjet printing, roll-to-roll, and coating technologies, which are relatively inexpensive processes[5-7].

However, it still remains a challenge to find suitable nanomaterials that can be reliably used for various coating methods. Therefore, we aimed to synthesize a wet-coatable WO_3 NP dispersion ink to form an EC thin film and to propose a suitable design for synthesizing the ink with optimal physicochemical properties in this study. In this case, polyvinyl alcohol (PVA) was added to the ink as an additive to improve the film forming performance. PVA has been widely studied as an additive for coating ink due to its good physical properties, excellent processability, optimum chemical resistance and easy film properties[8-12]. In addition, it has the high potential to be applied to a large area by using the slit coating method, which is one of the commercial coating technologies, by improving adhesion and wettability. However, a non-optimized amount of PVA in the ink causes agglomeration of WO_3 NPs, which deteriorates the uniformity of the thin film and greatly affects the electrochemical properties. Therefore, in this study, the effect of PVA addition amount on dispersibility and wettability of WO_3 NP dispersion ink was investigated. In addition, the physical properties and EC performance of the WO_3 films prepared by spin coating method using the synthesized inks were comprehensively investigated.

Therefore, in this study, we focused on the spin-coating method to fabricate WO_3 thin films, optimized the amount of PVA added to the WO_3 NP dispersed ink, which has not been studied to date, and evaluated the physical properties such as the wettability and dispersibility of the resulting ink. Moreover, we comprehensively examined the physical properties of thin films formed from the ink and their EC performance.

3. 2 Experimental

1) Chemicals

The following chemicals were purchased and used without additional purification: Potassium bis(trifluoromethanesulfonyl)imide (KTFSI, FUJIFILM Wako Pure Chemicals Co.), propylene carbonate (PC, 99 %, Kanto Chemicals Co., Inc.), and PVA (99 %, Japan Vam & Poval, Japan). Indium tin oxide (ITO)-coated glass with a surface resistivity of 10 Ω/sq was purchased form Geomatec Co.

2) Fabrication of WO_3 NP dispersed inks

WO_3 NPs (diameter: ~10 nm) used in thin study were obtained from Toshiba Materials Co. Ltd. We dispersed WO_3 NPs in deionized water by stirring at 1000 rpm at room temperature (~20 °C) for 48 h to prepare a WO_3 NP content of 25 wt.% of the total ink weight. The ink for film fabrication was prepared by mixing the 25wt.% WO_3 NP suspension with PVA in the range of 0 to 10 wt.%, and then filtering the ink through a 7 μm syringe filter (Kiriyama Glass Works Co.).

3) Surface tension, viscosity, density, and pH of the WO_3 NP inks

Surface tension and viscosity decreased with increasing PVA content of WO_3 NP ink from 0 to 10 wt.% (Table 3. 1). Figure 3. 1 shows a photograph of the prepared WO_3 NP dispersion ink, in which the pH of the suspension remains constant at 3.0 regardless of the PVA content, while the density of the ink decreases from 4.203 to 3.254 g/cm^2 with increasing PVA content.

Physical properties play an important role in the fabrication of inks with optimal coating performance, but they are not limiting; this means that thin films can be coated on substrates with these inks even when the ink properties are not optimal, but in such cases, the desired reliability and wettability of the coated inks may not be achieved[13].

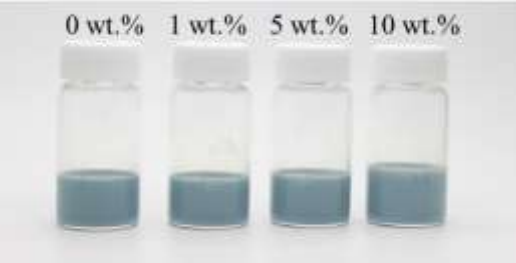

Figure 3. 1 Photograph of the WO_3 NP dispersed inks containing 0, 1, 5, and 10 wt.% of PVA[13].

Table 3. 1 Properties of the WO_3 NP dispersed inks with different PVA contents of 0, 1, 5, and 10 wt.%[13]

	0 wt%. PVA ink	**1 wt%. PVA ink**	**5 wt%. PVA ink**	**10 wt.% PVA ink**
Surface tension (mN/m)	61	59	44	41
Viscosity (cP)	16	19	17	11
Density (g/cm^3)	4.203	4.071	3.642	3.254
pH	3.0	3.0	3.0	3.0
Particle diameter (nm)	53	79	91	105
Contact angle (° ; without plasma treatment)	72.4	73.3	59.9	59.3
Contact angle (° ; with plasma treatment)	36.5	27.6	31.9	21.6

4) Particle size

The volume diameter of the prepared WO_3 NP inks was measured by dynamic light scattering (DLS; Delsa Nano Submicron, Beckman Coulter Inc.).

5) Film preparation

WO_3 NP thin films were prepared on ITO/glass substrates (size: 25 cm^2) by a spin coater (ACT-300Aα, Active Inc.). To improve the wettability, plasma treatment was

performed using a plasma cleaner (PDC-001, Harrick Plasma Inc.) for 3 min to hydrophilize the ITO/glass substrate surface before thin film preparation[14]. For plasma treatment, RF glow discharge was performed by applying power of 30 W in a low pressure environment of 1×10^{-3} Torr using a pump. The contact angle of WO_3 ink was measured after 50 s after it was dropped onto the ITO/glass substrate using a contact angle meter (DMs-400, Kyowa). In particular, the speed (rpm) of the spin coating process was controlled as the wettability of the ink was changed according to the PVA content to prepare a WO_3 thin film with a film thickness of ~1 μm (spin coating parameters are described in Table 3. 2).

Table 3. 2 Spin-coating conditions for the preparation of 1 μm thick WO_3 films[13].

Viscosity (cP)	Revolution (rpm)	Time (s)
10–14	360	10 min
14–17	400	10 min
17–35	400	10 s
	800	10 s

The film thickness was estimated using following equation:

$$d = m/(A \times \rho) \quad (3\text{-}1)$$

where ρ is the density of the ink, A is the area of the ITO/glass substrate, m is the weight of the coated WO_3 NP ink, and d is the film thickness (Table 3. 3 lists the weight of the deposited WO_3 ink and the area of the ITO/glass substrate).

Table 3. 3 Weights of the ITO substrate and coated WO_3, and the calculated WO_3 film thickness[13].

ITO substrate size (cm^2)	ITO substrate before spin coating (g)	ITO substrate after spin coating (g) (evaporated suspension)	Amount of coated WO_3 (g)	Calculated Film thickness (μm)
25	4.3950	4.4057	0.0107	1.02
25	4.2215	4.2346	0.0131	1.29
25	4.2938	4.3048	0.0110	1.21
25	4.2651	4.2787	0.0136	1.67

6) Film characterization

X-ray diffraction (XRD; D8 ADVANCE, Bruker AXS Inc.) was used to investigate the crystal structure of WO_3 nanopowders obtained from solvent (water) was evaporated at 120 °C in a drying oven WO_3 NP inks. XRD patterns were recorded in the 2θ range of 20-60°, measured at 40 kV and 40 mA using Cu-Kα radiation (λ = 1.5418 Å), and size of primary crystallites of WO_3 NPs was measured by the Pawley method using TOPAS V5.0 software.

X-ray photoelectron spectroscopy (XPS; Ulvac Inc. PHI 5000 Versaprobe) was employed for component irradiation of the thin film surface and was performed using Al-Kα radiation. A total irradiation scan of the sample was performed with a pass energy of 117.4 eV at a resolution of 0.2 eV in the 0–1000 eV range. High-resolution scans for W, O, and C were performed at a pass energy of 23.5 and a resolution of 0.025 eV, and a neutralizer filament was used to prevent sample charging. C 1s peak at 248.8 eV was used to correct for peak shift due to charging and calibrate the XPS spectrum. The W 4f spectra were analyzed using MultiPak version 9.6 software (a curve fitting program) and Shirley background was selected for spectral deconvolution. The peak of WO_3 was analyzed based on information from the past literature:

The Peaks were analyzed with a mixture of 80% Gaussian and 20% Lorentzian, constrained by a W $4f^{7/2}$-W $4f^{5/2}$ spin-orbit separation of 2.15 eV. XPS scans of the WO_3 film were performed in the range of binding energies (Eb) of 32-42 eV, and the area ratio of the two peaks in each doublet was 0.75. Field emission scanning electron microscope (FESEM, S-4800, Hitachi) was used for the films in a voltage range of 1-3

kV to investigate and thickness the surface and cross-sectional morphology of the film; Pt-Pd was coated on the films using an ion sputter coater (E-1030; Hitachi Ltd., Japan) to prevent charge of the films before measurement. In addition, energy dispersive X-ray spectroscopy (EDX; INCA X, Oxford) was performed to investigate the chemical composition of the film. Crosscut and scratch tests were used to test the adhesion between the ITO substrate and the WO_3 particles. For the cross-cut test, a thin film was cut in a grid shape with an interval of 1 mm, and the adhesiveness of the thin film was tested using a JIS Z 1522 standard test tape.

7) Electrochemical and electrochromic analysis

The electrochemical and EC properties of the film were measured using CV, chronoamperometry (CC), and multiple potential step (MPS) measurements, and the investigation was conducted using an electrochemical measurement system (6115D, ALS/HCH) using aqueous 1.5 mol/kg KTFSI/PC solution as an electrolyte. The WO_3 films prepared on ITO/glass, Pt, and Ag/AgCl were used as the working, counter, and reference electrodes, respectively. A multi-channel charge-coupled device detector (DH-2000, Ocean Optics) was used to measure in-situ transmittance changes. The EC switching time is defined as the time required for the total transmittance to exhibit a 90% change.

3. 3 Results and discussion

1) Properties of the WO_3 NP inks

Figure 3. 2 shows the volume diameter of WO_3 NPs in ink using DLS measurement. 53, 79, 91 and 105 nm were observed for the WO_3 NPs inks with PVA content of 0, 1, 5 and 10 wt.%, respectively. This can be attributed to the agglomeration of WO_3 particles in diameter with increasing PVA content. Figure 3. 3 shows the contact angle of WO_3 NP ink on plasma-treated or untreated ITO/glass substrates. Contact angles of 72.4, 73.3, 59.9 and 59.3° were obtained on untreated ITO/glass substrates with increasing PVA addition amount, respectively. In contrast, it decreased to 36.5, 27.6, 31.9 and 21.6° on plasma treated ITO/glass substrates, respectively. This is because plasma treatment has a beneficial effect on the coating process by improving the surface wettability.

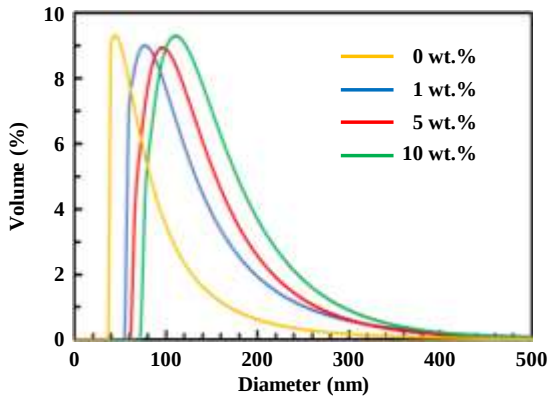

Figure 3. 2 Mean particle diameters of the synthesized WO_3 NP inks with PVA contents of 0 (yellow), 1 (blue), 5 (red), and 10 wt.% (green)[13].

2) Film structure, morphology, and chemical composition

Figure 3. 4 shows the XRD pattern of WO_3 NPs obtained after solvent evaporation by drying the ink at 120 °C in an oven. The WO_3 NPs exhibited broad peaks observed at approximately $2\theta = 23.9°$, which are corresponding to the envelope of the three characteristic peaks usually observed for the various forms of WO_3[15-17], and 7 broad

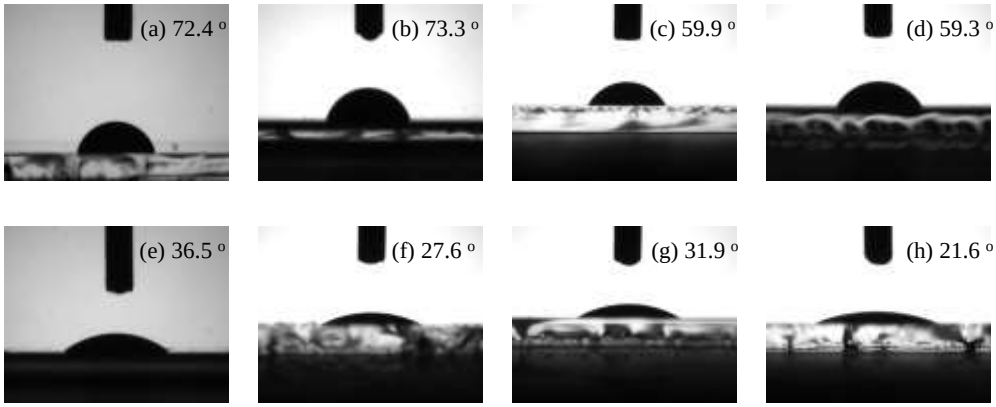

Figure 3. 3 Contact angles of WO_3 NP dispersed inks on ITO/substrates (a–d) before and (e–h) after plasma treatment of the substrate: (a, e) no PVA, (b, f) 1 wt.% PVA, (c, g) 5 wt.% PVA, and (d, h) 10 wt.% PVA[13].

peaks observed at approximately 2θ = 26.6, 29.9, 33.9, 41.7, 45.3, 50.5 and 55.3°. The crystallite size of the primary particles calculated by the Pawley method was ~11 nm, and it is thought that very small WO_3 crystallite size caused a broad peak[18].

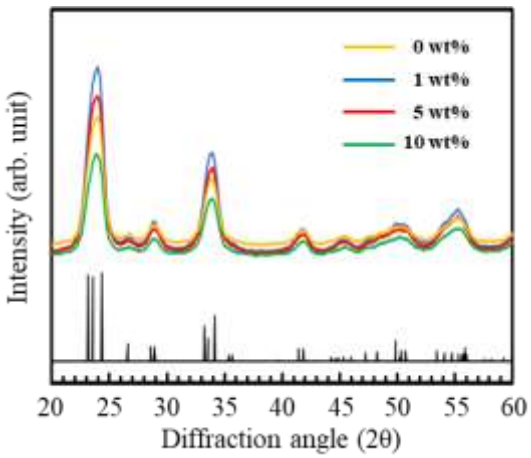

Figure 3. 4 XRD patterns of WO_3 nanopowders obtained from WO_3 NP dispersed inks containing (yellow) 0, (blue) 1, (red) 5, and (green) 10 wt.% of PVA. JCPDS card no. 72-0677 (black) is introduced in the figure for reference[13].

FE-SEM was used to investigate the effect of PVA on the film-forming properties of WO_3 NP inks. FE-SEM images of WO_3 films coated with 0, 1, 5, and 10 wt.% PVA-added inks (hereafter denoted as WO_3-0, 1, 5, and 10 wt.% PVA films, respectively) are

shown in Figure 3. 5.

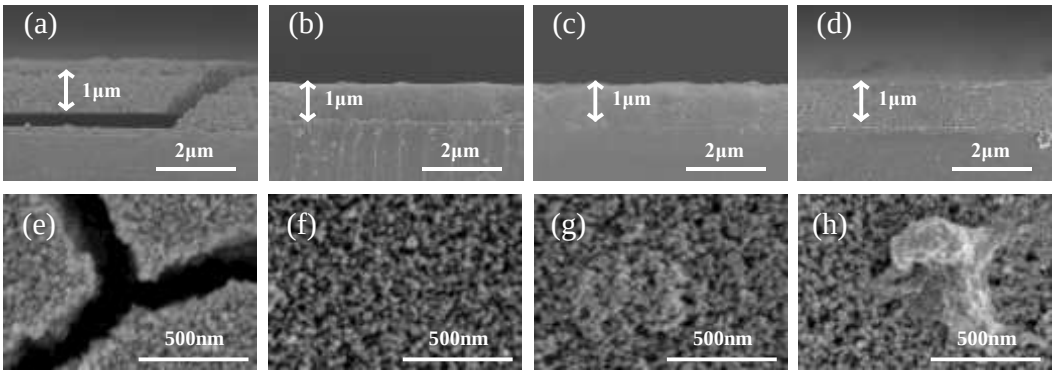

Figure 3. 5 FESEM (a–d) cross-sectional images and (e–h) surface morphologies of WO_3 thin films with (a, e) 0, (b, f) 1, (c, g) 5, and (d, h) 10 wt.% of PVA addition[13].

The cross-sectional images of all films had mesoporous structures as shown in Figure 3. 5 (a–d), which are considered to enhance K^+ diffusion in the films and contribute to the ionic conductivity. In addition, it was confirmed that the films with different PVA addition amounts had a thickness of about 1 μm, and excellent adhesion was observed between the ITO/glass substrate and the WO_3 coating regardless of the PVA addition amount of 1 to 10 wt.%. However, many cracks were observed for the WO_3 film without PVA addition, i.e., WO3-No PVA film, which exhibits poor film formation on the ITO/glass substrate as shown in Figure 3. 5 (a, e). The defects in the film are thought to be caused by the effect of stress that occurs when the ink is dried in the air due to the absence of PVA, which rolls as a binder between the substrate and the thin film. The surface image of the thin film in Figure 3. 5 (e–h) shows that the WO_3 film is composed of small NPs. No agglomeration of WO_3 NPs was observed in WO_3-1 wt.% PVA films. In contrast, many aggregations were observed at low magnifications (<×10000) for WO_3-5 and 10 wt.% PVA films. EDX analysis was performed on all thin films to investigate the chemical composition of the aggregates found. The agglomerates found in WO_3-5 and 10 wt.% PVA films were found to be mainly composed of carbon (Figure 3. 6) and this agglomeration may have occurred by resulting in the formation of nonuniform WO_3 film due to the increase in the PVA content.

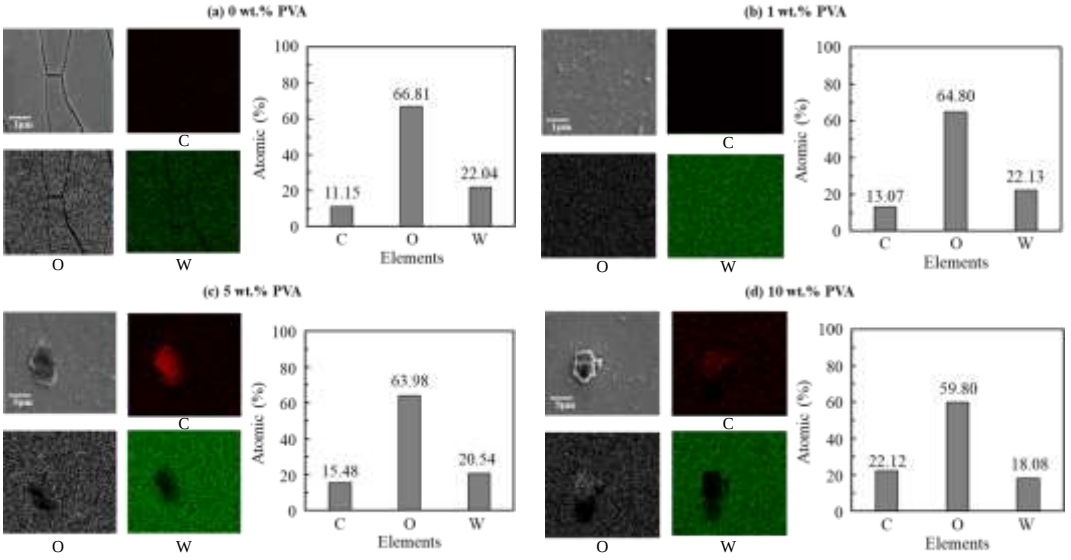

Figure 3. 6 FE-SEM images of WO_3 thin films containing different amounts of PVA: (a) 0, (b) 1 (c) 5, and (d) 10 wt.% PVA. The corresponding EDS maps show the distribution of C, O, and W[13].

Further, the chemical composition of the surface of the WO_3 film deposited on the

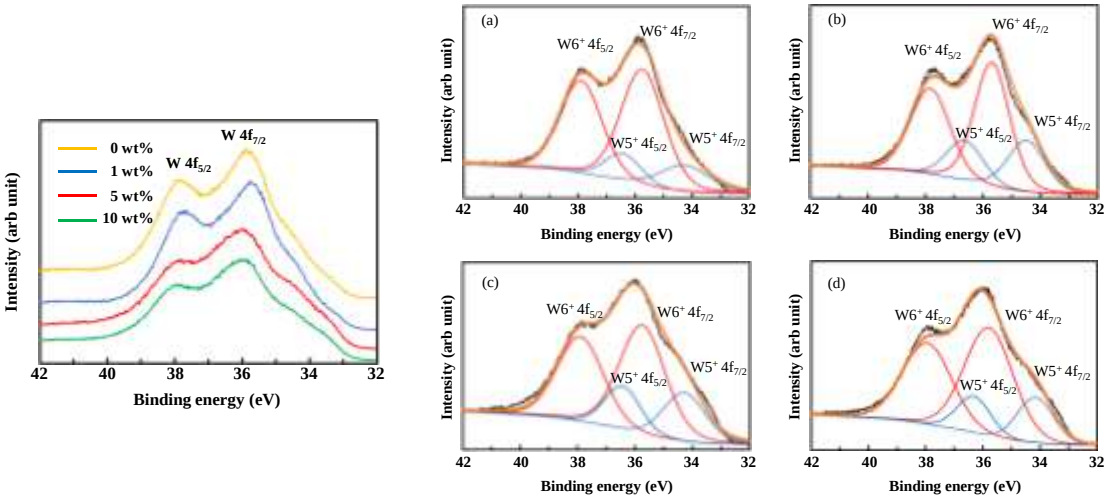

Figure 3. 7 W 4f doublet core-level spectra of WO_3 thin films with (yellow) no PVA, (blue) 1 wt.% PVA, (red) 5 wt.% PVA, and (green) 10 wt.% of PVA. Fitted XPS W 4f profiles of the as-deposited WO_3 films with PVA contents of (a) 0, (b) 1, (c) 5, and (d) 10 wt.%. The fitted doublets are shown for (blue) W^{5+} and (red) W^{6+}. The dotted peaks correspond to the sum of the two different tungsten species in the films[13].

ITO/glass substrate was investigated using XPS to investigate (Figure 3. 7). The peaks other than W, O, and C were not observed for the prepared WO_3 thin films in the XPS profile, which indicates that no contaminants were included in the thin film.

The W 4f and O 1s XPS profiles of WO_3 films containing different amounts of PVA are shown in Figures 3. 7 and 3. 8. Peaks at Eb = 35.8 and 37.9 eV, corresponding to W $4f^{7/2}$ and W $4f^{5/2}$, respectively. The XPS peaks which correspond to tungsten trioxide (VI) were mainly observed for the as-prepared WO_3 film as shown in Figure 3. 7 [19,20]. Thus, it is evident that tungsten is present in W^{6+} in the WO_3 film prepared in this study. In addition, a small amount of W^{5+} was observed for the films in the peak fitting analysis of W 4f, indicating that the prepared film was not completely oxidized. We thought that this oxygen deficiency contributed to the generation of the K^+ conduction pathway[21].

A characteristic peak of O 1s at about 530.3 eV appeared in the WO_3 thin film, which is consistent with the results of previous studies[22]. Low-intensity peaks corresponding to water bound to the film structure and water molecules adsorbed to the sample surface were obtained at about 532.2 eV (Figure 3. 8).

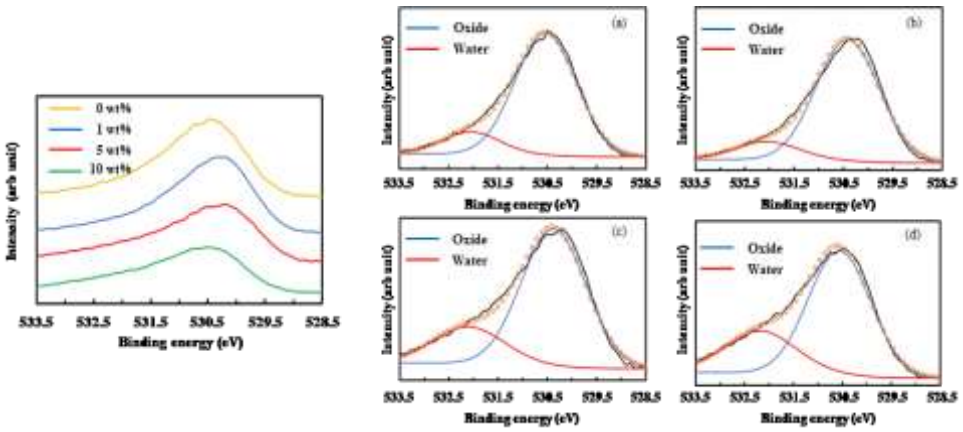

Figure 3. 8 O 1s core-level spectra of WO_3 films containing with (yellow) 0, (blue) 1, (red) 5, and (green) 10 wt.% of PVA addition. Fitted XPS O 1s profiles of the as-deposited WO_3 films with PVA contents of (a) 0, (b) 1, (c) 5, and (d) 10 wt.%. The fitted doublets are shown for (blue) oxide and (red) adsorbed water. The dotted peaks correspond to the sum of the two types of oxygen species in the films[13].

The carbon, oxygen and tungsten concentrations of the prepared WO_3 films were

calculated from the XPS spectra and are summarized in Table 3. 4 along with the core-level binding energies. The C1s signal for the WO_3 film observed at 284.8 eV could be attributed to the C–C bonding of PVA, and the carbon content of the film increased with increasing PVA amount (Figure 3. 9).

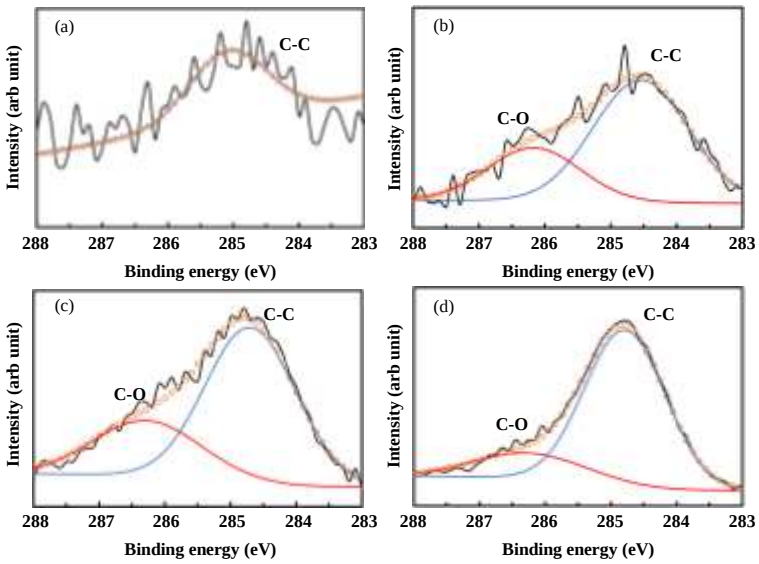

Figure 3. 9 Fitted XPS C 1s profiles of the as-deposited WO_3 films at PVA contents of (a) 0, (b) 1, (c) 5, and (d) 10 wt.%. The fitted doublets are shown for (blue) C–C and (red) C–O linkages. The dotted peaks correspond to the sum of the two types of carbon in the films[13].

Table 3. 4 XPS curve-fitting analysis of the C 1s, O 1s, and W 4f core levels in WO_3 thin films containing with 0, 1, 5, and 10 wt.% of PVA addition, and comparison with previously reported values[13].

		Binding energy (eV)					Atomic concentration (at%)			
Atomic orbital		**0wt%**	**1wt%**	**5wt%**	**10wt%**	**Reference**	**0wt%**	**1wt%**	**5wt%**	**10wt%**
C 1s				284.8			4.0	9.5	20.6	39.7
O 1s		530.5	530.3	530.4	530.4	530.5[52]	71.6	67.6	59.5	45.4
W 4f							24.4	22.9	19.9	14.9
W^{5+}	$4f_{5/2}$	34.3	34.4	34.3	34.2	34.4[51]				
	$4f_{7/2}$	36.4	36.6	36.4	36.3	36.5[51]				
W^{6+}	$4f_{5/2}$	35.7	35.7	35.7	35.8	35.8[49,50]				
	$4f_{7/2}$	37.9	37.8	37.9	37.9	37.9[49, 50]				

Figure 3. 10 shows the photos of the thin film before and after the cross-cut test. In the WO_3-0 wt.% film, it was observed that a large part of the thin film was peeled off in the photos before and after the test. By contrast, the adhesion between the WO_3 particles and the substrate was improved by adding 1 wt% or more of PVA.

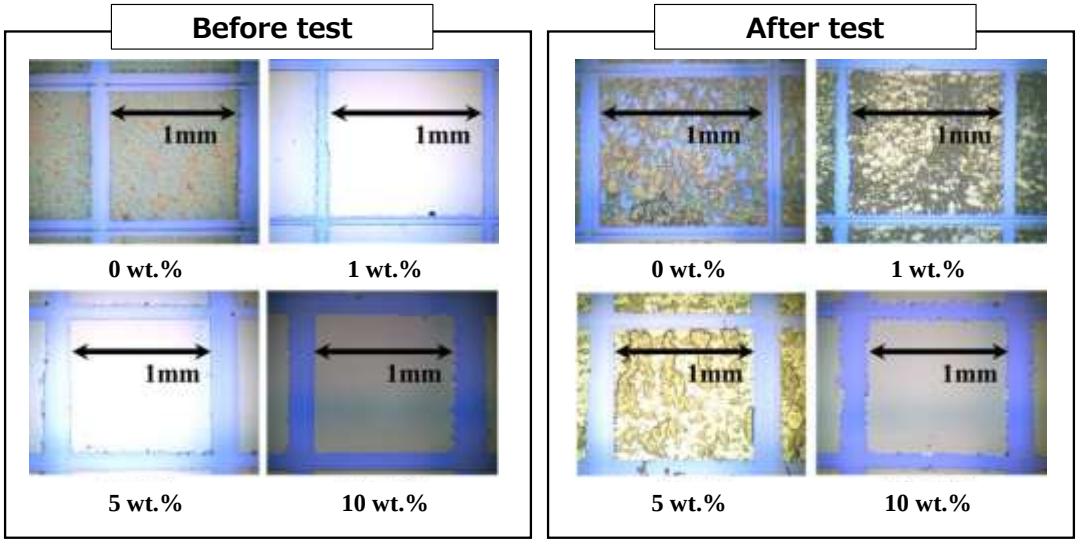

Figure 3. 10 Photos of the thin film before and after the cross-cut test.

In the scratch test, peeling occurred at a low load in the 0 wt.% thin film. However, it was observed that the scratch resistance was improved by adding 1 wt.% or more of PVA (Figure 3. 11).

3) Electrochemical and electrochromic properties

The electrochemical and EC properties of WO_3-0, 1, 5 and 10 wt.% PVA films deposited on ITO/glass substrates were measured in a 1.5 mol/kg KTFSI/PC solution as electrolyte. Cyclic voltammograms were recorded by measuring WO_3 films over a potential range of –1.2 to +1.0 V (vs. Ag/AgCl) with a sweep rate of 5 mV/s (Figure 3. 12). Typical CV curves were obtained for WO_3-1 and 5 wt.% PVA films, and the cathode current peak corresponding to the K^+ insertion was observed at –1.20 V[23]. Furthermore, the anode current peak corresponding to the injection of K^+ gradually shifted toward the positive potential as the PVA content decreased. In contrast, no peaks

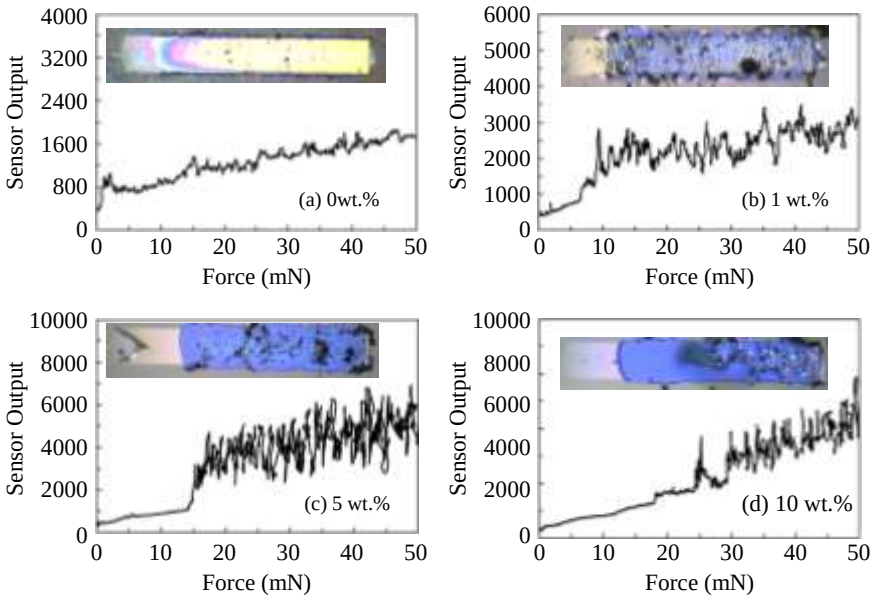

Figure 3. 11 Scratch test of WO_3 thin film with (a) 0, (b) 1, (c) 5, and (d) 10 wt.% PVA addition.

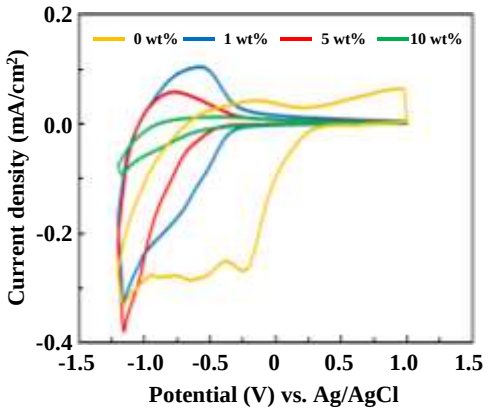

Figure 3. 12 CV profiles of the WO_3 thin films containing with (yellow) 0, (blue) 1, (red) 5, and (green) 10 wt.% of PVA addition. The potential scan rate was 5 mV/s[13].

and no performance as an EC material were obtained for the WO_3-10 wt.% PVA film in the potential range. This is possible because increasing PVA content affects the ionic conductivity of the film and the XPS results support this. In addition, several cathodic current peaks were observed for the WO_3 film without PVA addition. The peaks corresponding to the $W^{6+} \rightarrow W^{5+}$ and $W^{5+} \rightarrow W^{4+}$ transitions[24] were observed at approximately –0.25 V and –0.65 V, respectively, and the peak observed at –1.2 V may

have occurred because of H_2 evolution at high negative potentials[25]. However, no anode current peak was observed. In addition, to measure the cycling durability test, it was performed for 5 cycles on WO_3-1 wt.% PVA film, and a fast potential sweep rate of 25 mV/s was used for the cycling test to reduce the measurement time. No differences were observed in the areas of the CV curves recorded in the first and fifth cycles (Figure 3. 13).

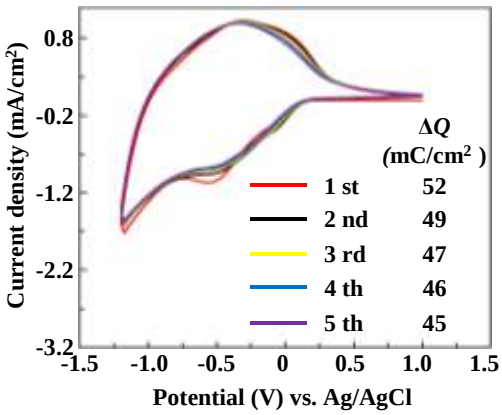

Figure 3. 13 CV profiles and Q of the WO_3 film with a PVA content of 1 wt.% in 1.5 mol/kg KTFSI/PC. The potential scan rate and sample interval were 25 mV/s and 20 mV, respectively[13].

The transferred charge density (Q) was determined by charge amount obtained by applying constant potentials of –1.2 and +1.0 V for 5 and 120 s, respectively, for a complete redox reaction and the resultant current densities are exhibited with respect to time (Figure 3. 14). The reversible K^+ charge/discharge process obtained for the WO_3-1, 5, and 10 wt.% PVA films. In contrast, the process of discharge after charge was not observed for the WO_3 film without PVA. This is thought to be related to the absence of the anodic current peak in the CV curve. The WO_3-1 wt.% PVA film exhibited the largest Q of 24 mC/cm^2 (Table 3. 5).

The light transmittance changes of WO_3 thin films in colored and bleached states were studied by UV-vis spectroscopy during CC and the spectra are shown in Figure 3. 15. Redox reaction by K^+ cations changes the transmittance of the film in the visible region and induces a reversible color transition from transparent (discharge) to blue

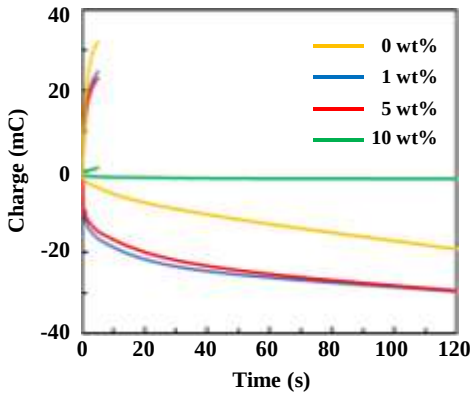

Figure 3. 14 CC of the WO_3 thin films containing with (yellow) 0, (blue) 1, (red) 5, and (green) 10 wt.% of PVA addition. Constant voltages of –1.2 to +1.0 V (vs. Ag/AgCl) were applied for 5 and 120 s, respectively[13].

Table 3. 5 Transmittance (*T*), optical density (Δ*OD*), coloration efficiency (*CE*), and optical switching time of the WO_3 thin films containing with 0, 1, 5, and 10 wt.% of PVA addition at 550 and 633 nm in the colored and bleached states in a 1.5 mol/kg KTFSI/PC electrolyte solution[13].

Amount of PVA (wt.%)	Film area (cm^2)	Wavelength (nm)	$T_{bleached}$ (%)	$T_{colored}$ (%)	Charge (C)	Q (C/cm^2)	ΔOD	CE (cm^2/C)	$t_{colored}$ (s)	$t_{bleached}$ (s)
0	1	550	66	25	0.032	0.032	0.42	13.1	4.11	-
1	1		89	31	0.024	0.024	0.46	19.1	4.11	3.18
5	1		88	33	0.023	0.023	0.42	18.5	4.21	7.18
10	1		88	88	0.010	0.010	-	-	-	-
0	1	633	54	8	0.032	0.032	0.81	25.3	4.13	-
1	1		90	13	0.024	0.024	0.84	35.0	3.15	4.16
5	1		89	15	0.023	0.023	0.77	33.6	3.19	9.22
10	1		88	87	0.010	0.010	0.01	0.5	-	-

(charge), and the related color change in the films is demonstrated in Figure 3. 15. In particular, it was observed that the film without PVA showed no discoloration because there was no deintercalation, and the film was damaged. This is thought to be due to the many cracks in the film in the surface FE-SEM image of this sample.

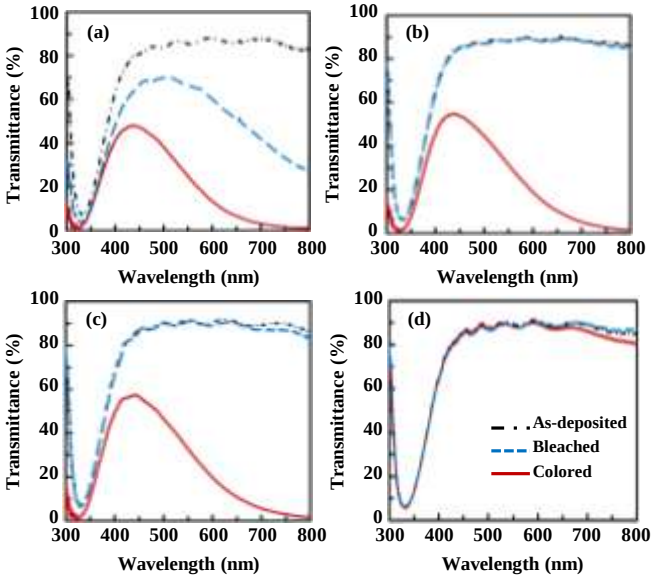

Figure 3. 15 Transmittance spectra of the WO_3 thin films containing with (a) 0, (b) 1, (c) 5, and (d) 10 wt.% of PVA addition in bleached (blue), colored (red), and as-deposited (black) states. Constant voltages of –1.2 and +1.0 V (vs. Ag/AgCl) were applied for 5 and 120 s, respectively[13].

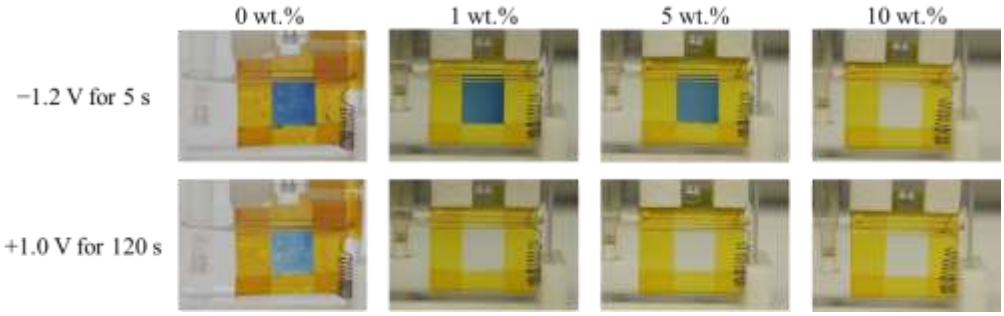

Figure 3. 16 Photographs of the films in colored and bleached states, captured after applying constant voltages of −1.2 and +1.0 V (vs. Ag/AgCl) for 5 and 120 s, respectively[13].

The film transmittance spectral changes in the colored and bleached state (Figure 3. 16) indicate that WO_3-1 and 5 wt.% PVA films are suitable for EC smart window applications. The stability test of the WO_3-1 wt.% film was performed up to 100 cycles as shown in Figure 3. 17. Degradation was observed as the number of cycles increased. This is because the ion trapping/de-trapping process of the WO_3 film is not smooth, and

there is a possibility that the optical modulation characteristics of the film may be deteriorated.

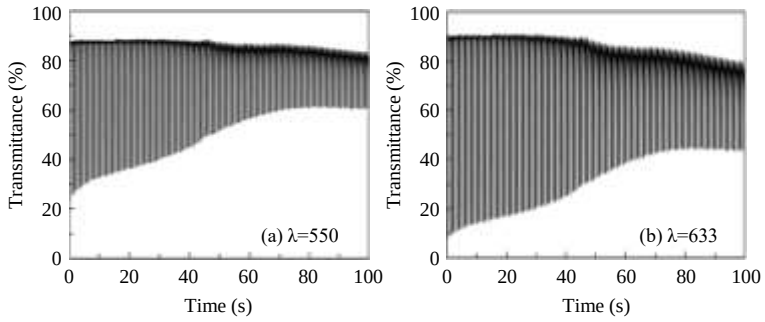

Figure 3. 17 Transmittance changes in the WO_3 film having a PVA content of 1 wt.% with cycle number during the multipotential step for 100 cycles at wavelengths of 550 and 633 nm.

There is a possibility that the process of ion trapping/detrapping due to redox reactions is not smooth in WO_3 films, and hence these processes degrade the optical modulation characteristics of the films[26]. However, in a previous study[27], we used WO_3 to develop an EC device with no degradation in transmittance change properties even after 100 cycles. Therefore, we believe that WO_3 films can be used to solve the ion trapping/de-trapping problem when preparing EC devices. Therefore, we are planning to fabricate and combine individual EC devices and verify their stability with similar tests in future studies.

The optical switching rate of the WO_3 films in colored and bleached states was calculated based on the time required for 90% change in the transmittance (Figure 3. 18). Very fast switching times of less than 5 s was observed at wavelengths of 550 and 633 nm for the WO_3-1 and 5 wt.% PVA films. These EC properties of the WO_3 film were comparable to that reported in previous studies[28-34], as shown in Table 3. 6. These large values are thought that the number of W atoms contributing to the redox reaction increases as the amount of PVA addition decreases and becomes an electrochemically active state.

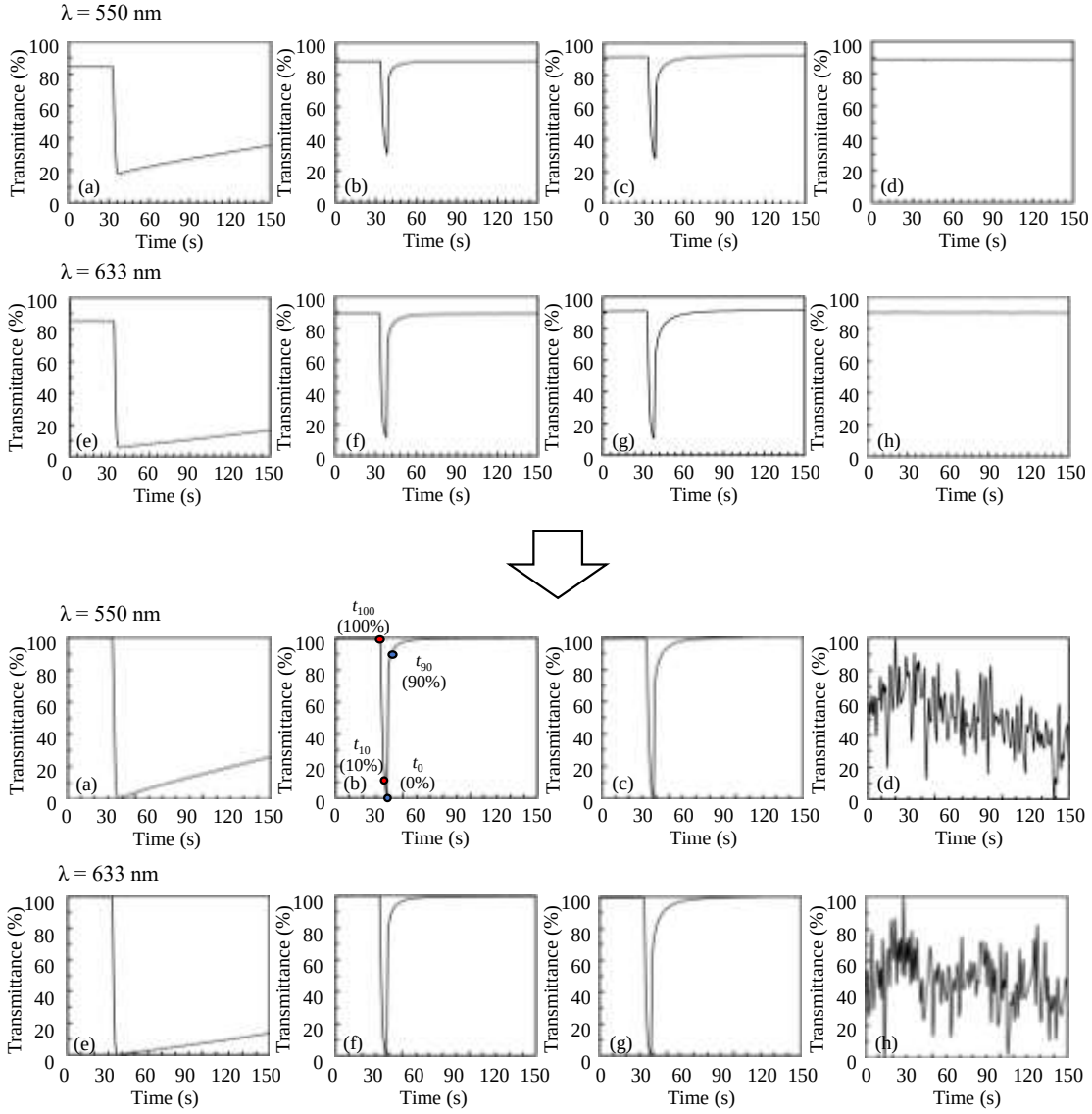

Figure 3. 18 Change in transmittance with time at visible wavelengths of 550 and 633 nm under constant voltages of −1.2 and +1.0 V (vs. Ag/AgCl) applied for 5 and 120 s, respectively. The switching time of the coloring (red circle; t_{100} to t_{10}) and bleaching (blue circle; t_0 to t_{90}) reaction was measured by converting the transmittance changes into percentage using the following equation: $T\% = \frac{(T_{\lambda t} - T_{min})}{\Delta T} \times 100\ \%$.

Table 3. 6 Performance summary of the WO_3 electrochromic materials[28-34].

Materials	Fabrication method	Transmittance modulation	Switching speed t_c/t_b (s)	Used electrolyte	Ref.
Adhesive WO_3	Spin coating	77 %@633 nm	3.15/4.16	K^+ ion	This work
Self-doped WO_{3-x}	Spin coating	70 %@680 nm	7/15	Li^+ ion	60
WO_3	Reactive sputtering	74 %@630 nm	5.7/2.2	Li_xAlO_z	61
WO_3	Hydrothermal	78 %@630 nm	5/6	Li^+ ion	62
Ti-doped WO_3	Wet bath	68 %@633 nm	15/5	H^+ ion	63
Co-doped WO_3	Hydrothermal	75 %@680 nm	27.6/11.8	Li^+ ion	64
WO_3/rGO	Spin coating	64 %@633 nm	9.5/4.5	Li^+ ion	65
2D WO_3	Solution-phase synthesis	63 %@700 nm	10.7/7	Li^+ ion	66

Furthermore, the optical density (ΔOD) and EC staining efficiency (CE), which are important EC parameters controlling the electrochemical performance of the film, were calculated using the following equations.

$$\Delta OD = \log_{10}(T_{\lambda b}/T_{\lambda c}) \quad (3\text{-}2)$$

$$\eta = \Delta OD/Q \quad (3\text{-}3)$$

where $T_{\lambda b}$ and $T_{\lambda c}$ represent the transmittances of the bleached and colored WO_3 films, respectively.

ΔOD and CE values of the WO_3 films containing with 0, 1, 5, and 10 wt.% of PVA addition are listed in Table 3. 5. The WO_3-1 wt.% PVA film exhibited the highest ΔOD and CE of 0.84 and 35.0 cm^2/C, respectively, and these largest values obtained in this study using an electrolyte containing K^+, is comparable to these previously reported the WO_3 thin films values (Table 3. 6).

3. 4 Conclusions

Wet-coatable WO_3 NP inks were successfully prepared with 0, 1, 5, and 10 wt.% of PVA addition and EC films was prepared by spin-coating method on the ITO/glass substrates. The highest transmittance change in the visible and NIR regions was observed for the WO_3-1 wt.% PVA film. Such behavior might be utilized in the future to construct an EC device that can control the transmittance of light in the NIR or NIR/visible region of smart windows. Therefore, we believe that the preparation of wet-coatable WO_3NP dispersions and the understanding of EC properties in this study will be useful for developing materials and processes for smart windows in the future. In addition, the prepared WO_3 films had a mesoporous structure, which allows potassium to be easily diffuse into the films while having a larger ionic radius than lithium. These results will give an advantage to the R&D of secondary batteries using potassium, which are relatively safer, cheaper than lithium, and have excellent market availability. Further, the coating technology of the WO_3 thin film investigated in this study can be extended to other electrochemically active thin films such as sensing films, cathodes of thin-film batteries, photocatalysts, and others, as well as to EC films fabrication.

Reference

[1] S.K. Deb, J.A. Chopoorian, Optical properties and color-center formation in thin films of molybdenum Trioxide, J. Appl. Phys. 34 (1966) 4818. https://doi.org/10.1063/1.1708145

[2] T.D. Nguyen, L.P. Yeo, T.C. Kei, D. Mandler, S. Magdassi, A.I.Y. Tok, Efficient near infrared modulation with high visible transparency using SnO_2–WO_3 nanostructure for advanced smart windows, Adv. Opt. Mater. 7 (2019) 1801389. https://doi.org/10.1002/adom.201801389

[3] R. Todo, Y. Abe, M. Kawamura, K.H. Kim, Effects of electrolyte solutions and their pH on the electrochromic cycling stability of reactively sputtered WO_3 thin films, ECS Trans. 58 (2014) 125. https://doi.org/10.1149/05825.0125ecst

[4] R. Parsons, Sputtering deposition processes, J.V. Vossen, W. Kern (Eds.), Thin Film Processes II, Academic Press, San Diego (1991), pp. 177-208.

[5] M. Layani, P. Darmawan, W.L. Foo, L. Liu, A. Kamyshny, D. Mandler, S. Magdassi, P.S. Lee, Nanostructured electrochromic films by inkjet printing on large area and flexible transparent silver electrodes, Nanoscale 6 (2014) 4572. https://doi.org/10.1039/C3NR06890K

[6] S. Lin, X. Bai, H. Wang, H. Wang, J. Song, K. Huang, C. Wang, N. Wang, B. Li, M. Lei, H. Wu, Roll-to-roll production of transparent silver-nanofiber-network electrodes for flexible electrochromic smart windows, Adv. Mater. 29 (2017) 1703238. https://doi.org/10.1002/adma.201703238

[7] K. Tajima, C.Y. Jeong, T. Kubota, T. Ito, K. Araki, T. Kamei, M. Fukui, Mass-producible slit coating for large-area electrochromic devices, Sol. Energy Mater. Sol. Cells 232 (2021) 111361. https://doi.org/10.1016/j.solmat.2021.111361

[8] Z. Guo, D. Zhang, S. Wei, Z. Wang, A.B. Karki, Y. Li, P. Bernazzani, D.P. Young, J.A. Gomes, D.L. Cocke, T.C. Ho, Effects of iron oxide nanoparticles on polyvinyl alcohol: interfacial layer and bulk nanocomposites thin film, J. Nanopart. Res. 12 (2009) 2415. https://doi.org/10.1007/s11051-009-9802-z

[9] S. Sathish, B.C. Shekar, B.T. Bhavyasree, Nano composite PVA-TiO_2 thin films for OTFTs, Adv. Mat. Res. 678 (2013) 335. https://doi.org/10.4028/www.scientific.net/AMR.678.335

[10] S. Sugumaran, C.S. Bellan Transparent nano composite PVA–TiO_2 and PMMA–TiO_2 thin films: optical and dielectric properties, Optik 125 (2014) 5128. https://doi.org/10.1016/j.ijleo.2014.04.077

[11] R. Devi, P. Purkayastha. P.K. Kalita, B.K. Sarma, Synthesis of nanocrystalline CdS

thin films in PVA matrix, Bull. Mater. Sci. 30 (2007) 123. https://doi.org/10.1007/s12034-007-0022-9
[12] P.J. Wojcik, L. Santos, L. Pereira, R. Martins, E. Fortunato, Tailoring nanoscale properties of tungsten oxide for inkjet printed electrochromic devices, Nanoscale 7 (2015) 1696. https://doi.org/10.1039/C4NR05765A
[13] C.Y. Jeong, H. Watanabe, K. Tajima, Adhesive electrochromic WO_3 thin films fabricated using a WO_3 nanoparticle-based ink, Electrochim. Acta, 389 (2021) 138764. https://doi.org/10.1016/j.electacta.2021.138764
[14] R. Wolf, A.C. Sparavigna, Role of plasma surface treatments on wetting and adhesion, Engineering, 2 (2010) 397. https://doi.org/10.4236/eng.2010.26052
[15] C. Costa, C. Pinheiro, I. Henriques, C.A.T. Laia, Inkjet printing of sol–gel synthesized hydrated tungsten oxide nanoparticles for flexible electrochromic devices, ACS Appl. Mater. Interfaces 4 (2012) 1330. https://doi.org/10.1021/am201606m
[16] W. Cheng, E. Baudrin, B. Dunna, J.I. Zink, Synthesis and electrochromic properties of mesoporous tungsten oxide, J. Mater. Chem. 11 (2001) 92. https://doi.org/10.1039/B003192P
[17] J. Wang, E. Khoo, P.S. Lee, J. Ma, Controlled synthesis of WO_3 nanorods and their electrochromic properties in H_2SO_4 electrolyte, J. Phys. Chem. C 113 (2009) 9655. https://doi.org/10.1021/jp901650v
[18] N.L. Houx, G. Pourroy, F. Camerel, M. Comet, D. Spitzer, WO_3 Nanoparticles in the 5-30 nm range by solvothermal synthesis under microwave or resistive heating, J. Phys. Chem. C 114 (2010) 155. https://doi.org/10.1021/jp908669u
[19] G. Leftheriotis, S. Papaefthimiou, P. Yianoulis, A. Siokou, D. Kefalas, Structural and electrochemical properties of opaque sol–gel deposited WO_3 layers, Appl. Surf. Sci. 218 (2003) 276. https://doi.org/10.1016/S0169-4332(03)00616-0
[20] G. Cai, X. Wang, D. Zhou, J. Zhang, Q. Xiong, C. Gu, J. Tu, Hierarchical structure Ti-doped WO_3 film with improved electrochromism in visible-infrared region, RSC Adv. 3 (2013) 6896. https://doi.org/10.1039/C3RA40675J
[21] G. Leftheriotis, S. Papaefthimiou, P. Yianoulis, A. Siokou, Effect of the tungsten oxidation states in the thermal coloration and bleaching of amorphous WO3 films, Thin Solid Films 384 (2001) 298. https://doi.org/10.1016/S0040-6090(00)01828-9
[22] C. Cantalini, W. Wlodarski, Y. Li, M. Passacantando, S. Santucci, E. Comini, G. Faglia, G. Sberveglieri, Investigation on the O_3 sensitivity properties of WO_3 thin films prepared by sol–gel, thermal evaporation and R.F. sputtering techniques, Sens. Actuators B Chem. 64 (2000) 182. https://doi.org/10.1016/S0925-4005(99)00504-3
[23] Z. Jiao, X.W. Sun, J. Wang, L. Ke, H.V. Demir. Hydrothermally grown

nanostructured WO_3 films and their electrochromic characteristics, J. Phys. D Appl. Phys. 43 (2010) 285501. https://doi.org/10.1088/0022-3727/43/28/285501
[24] S. Darmawi, S. Burkhardt, T. Leichtweiss, D.A. Weber, S. Wenzel, J. Janek, M.T. Elm, P.J. Klar, Correlation of electrochromic properties and oxidation states in nanocrystalline tungsten trioxide, Phys. Chem. Chem. Phys. 17 (2015) 15903. https://doi.org/10.1039/c5cp02482j
[25] Y.E. Firat, A. Peksoz, Efficiently two-stage synthesis and characterization of CuSe/Polypyrrole composite thin films. J. Alloy. Compd. 727 (2017) 177. https://doi.org/10.1016/j.jallcom.2017.08.095
[26] R.T. Wen, C.G. Granqvist, G.A. Niklasson, Eliminating degradation and uncovering ion-trapping dynamics in electrochromic WO_3 thin films, Nat. Mater. 14 (2015) 996. https://doi.org/10.1038/nmat4368
[27] K. Tajima, H. Watanabe, M. Nishino, T. Kawamoto Green fabrication of a complementary electrochromic device using water-based ink containing nanoparticles of WO3 and Prussian blue
RSC Adv. 10 (2020) 2562. https://doi.org/10.1039/C9RA09153J
[28] L. Zhou, P. Wei, H. Fang, W. Wu, L. Wu, H. Wang, Self-doped tungsten oxide films induced by in situ carbothermal reduction for high performance electrochromic devices, J. Mater. Chem. C 8 (2020) 13999. https://doi.org/10.1039/D0TC03103H
[29] L. Xie, S. Zhao, Y. Zhu, Q. Zhang, T. Chang, A. Huang, P. Jin, S. Ren, S. Bao, High Performance and excellent stability of all-solid-state electrochromic devices based on a $Li_{1.85}AlO_z$ ion conducting layer, ACS Sustain. Chem. Eng. 7 (2019) 17390. https://doi.org/10.1021/acssuschemeng.9b04501
[30] J.B. Pan, Y. Wang, R.Z. Zheng, M.T. Wang, Z.Q. Wan, C.Y. Jia, X.L. Weng, J.L. Xie, L.J. Deng, Directly grown high-performance WO_3 films by a novel one-step hydrothermal method with significantly improved stability for electrochromic applications, J. Mater. Chem. A 7 (2019) 13956. https://doi.org/10.1039/C9TA01333D
[31] Y. Zhan, M.R.J. Tan, X. Cheng, W.M.A. Tan, G.F. Cai, J.W. Chen, V. Kumar, S. Magdassi, P.S. Lee, Ti-Doped WO_3 synthesized by a facile wet bath method for improved electrochromism, J. Mater. Chem. C 5 (2017) 9995. https://doi.org/10.1039/C7TC02456H
[32] K. Shen, K. Sheng, Z.T. Wang, J.M. Zheng, C.Y. Xu, Cobalt ions doped tungsten oxide nanowires achieved vertically aligned nanostructure with enhanced electrochromic properties, Appl. Surf. Sci. 501 (2020) 144003. https://doi.org/10.1016/j.apsusc.2019.144003
[33] B.W. Zhao, S.J. Lu, X. Zhang, H. Wang, J.B. Liu, H. Yan, Porous WO_3/reduced

graphene oxide composite film with enhanced electrochromic properties, Ionics 22 (2016) 261. https://doi.org/10.1007/s11581-015-1547-3
[34] A. Azam, J. Kim, J. Park, T.G. Novak, A.P. Tiwari, S.H. Song, B. Kim, S. Jeon, Two-dimensional WO_3 nanosheets chemically converted from layered WS_2 for high-performance electrochromic devices, Nano Lett. 18 (2018) 5646. https://doi.org/10.1021/acs.nanolett.8b02150

Chapter 4

Fabrication of Electrochromic Devices Using a Wet-Coatable WO_3 Nanoparticle Dispersion ink

4. 1 Introduction

Smart windows are promising in terms of energy saving and environmental impact by efficiently controlling the amount of light coming from outside such as buildings, houses and automobiles even with low electrical energy[1-4]. In particular, smart windows for next-generation automobiles are expected to require high optical modulation along with flexibility in terms of application in multi-purpose intelligent design[5]. We have successfully fabricated a wet-coatable WO_3 ink in previous study[6]. In addition, the coated WO_3 thin film was successfully prepared on an ITO/glass substrate by spin coating as laboratory level, and excellent electrochemical and EC properties (optical modulation, cyclic durability, and coloration efficiency, etc.) were obtained from the WO_3 thin film containing 1 wt.% of PVA. Although, glass substrates have advantages such as high transmittance and electrical conductivity, they are difficult to deform and have heavy weight. Thus, it is necessary to develop the next-generation EC smart window (i.e., automobile, aircraft, building, etc.) that exhibits excellent EC characteristics while having various shape changes and strong strength. Therefore, in this study, EC devices were fabricated using a flexible PET substrate for the production of next-generation EC devices. For the preparation of flexible ECDs, a wet-coatable WO_3 and PB NPs water dispersed ink investigated in our previous research[6-8] was used, and chromaticity and haze were investigated in detail as evaluation indicators to confirm the specifications for actual use in the automotive field. In addition, the fabricated PET EC devices was compared with the EC device prepared using conventional glass substrates.

4. 2 Experimental

1) Water-dispersed WO_3 and PB NP inks

The preparation of the water-dispersed PB NP ink was prepared as follows[6-8]. $Fe(NO_3)_3 \cdot 9H_2O$ and $Na_4[Fe(CN)_6] \cdot 10H_2O$ were mixed and stirred to prepare PB ink. PB and water were separated from this PB ink using a centrifuge, and the PB was washed through repeated operations. $Na_4[Fe(CN)_6].10H_2O$ was added to the washed PB to improve the dispersibility of the precipitate in water, and the suspension was stirred at room temperature for 1 week to prepare an aqueous dispersion PB NP ink. In addition, polyvinyl alcohol (PVA; 10wt%) was added to the PB ink to increase viscosity and adhesion of the ink to form a uniform PB film. WO_3 NPs (diameter: ~10 nm) used in thin study were obtained from Toshiba Materials Co. Ltd. Adhesion and Interface Research Group at National Institute of Advanced Industrial Science and Technology (AIST) dispersed WO_3 NPs in deionized water by stirring at 1000 rpm at room temperature (~20 °C) for 48 h to prepare a WO_3 NP content of 25 wt.% of the total ink weight. The ink for film fabrication was prepared by mixing the 25wt.% WO_3 NP suspension with PVA in the range of 1 wt.%, and then filtering the ink through a 7 μm syringe filter (Kiriyama Glass Works Co.). The details are listed in Table 4. 1.

Table 4. 1 Properties of the PB- and WO_3-NP dispersible inks with varying PVA contents of 10 and 1 wt.%, respectively[9].

	PB-10 wt%. PVA ink	**WO_3-1 wt%. PVA ink**
Surface tension (mN/m)	45.1	52.3
Viscosity (cP)	19.4	7.3
Density (g/cm^3)	1.08	4.07
pH	6.7	4.9
Contact angle(°) (before UV treatment)	93.6	48.8
Contact angle(°) (after UV treatment)	48.8	46.4

2) Surface treatment of substrates

ITO/glass and ITO/PET substrates were prepared with an area of 25 cm^2, and both substrates were surface-treated to improve ink coating efficiency and thin film adhesion. UV treatment was adopted for the surface treatment of the substrate. After setting the moving distance of the conveyor to 50 mm, the distance between the substrate and the lamp was set to 10 mm, and the surface was repeatedly irradiated with ultraviolet (UV) light (λ = 365 nm) for 25 minutes at a conveyor speed of 10 mm/min (HLDL-375X10U6-SP, CCS Inc.; Figure. 4. 1).

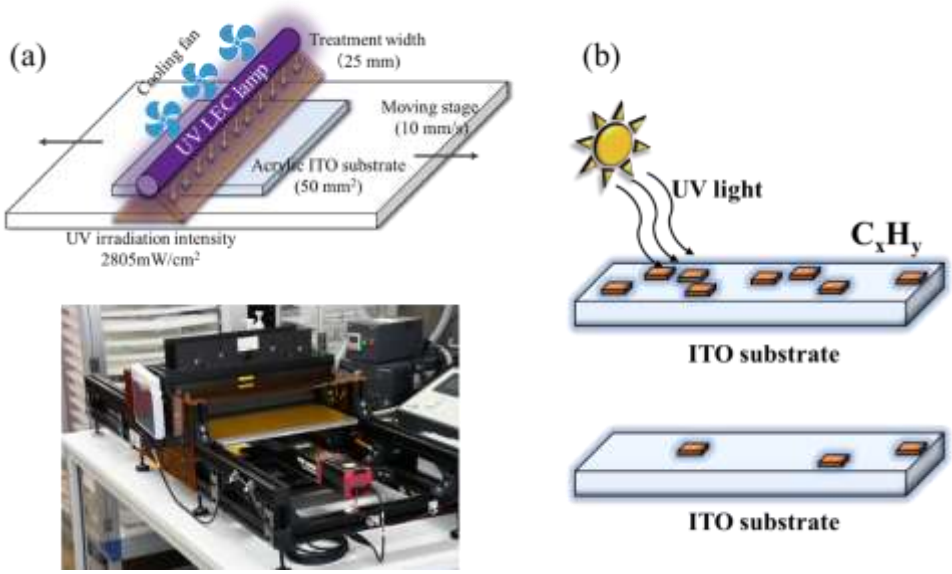

Figure 4. 1 Illustration, photograph (a), and mechanism (b) of the UV light treatment[9].

The UV dose was adjusted between 0 and 2805 $mW \cdot s \cdot cm^{-2}$, and the temperature was controlled using a cooling fan and monitored using a temperature label. The contact angles of water, PB, and WO_3 NP inks were measured 60 seconds after dropping on the ITO/glass and flexible substrate surface (DMs-400, Kyowa Interface Science Co., Ltd).

3) Electrochromic thin films prepared using water-dispersible NP inks

Spin coating (POLOS Spin150i, SPS Europe, Inc.) was used to prepare WO_3 and PB thin films on surface-treated ITO/glass and ITO/PET substrates (Figure 4. 2).

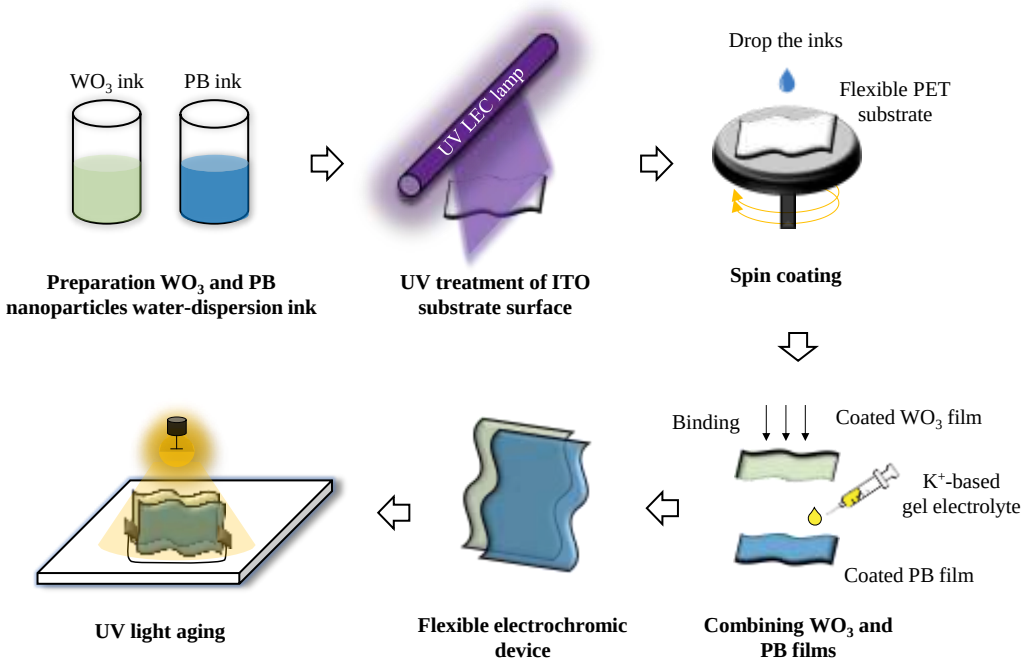

Figure 4. 2 Illustrations of ECD preparation[9].

Spin parameters are described in Table 4. 2. The speed (rpm) of the spin coating process was controlled to make a film with a thickness of about 1 μm, and the film thickness (d) was calculated as follows[10]

$$d = m/(A \times \rho) \quad (4\text{-}1)$$

where ρ is the density of the ink, A is the area of the substrate, and m is the weight of the coated WO_3 or PB NP-water-dispersible ink.

The weights of the ITO/glass and PET substrates and WO_3 and PB inks are shown in Table 4. 3.

Table 4. 2 Spin-coating conditions for the preparation of 1 μm-thick WO_3 and PB thin films[9].

Viscosity (cP)	Revolution (rpm)	Time (s)
1–10	300	600 s
10–14	360	600 s
14–17	400	600 s
17–35	500	10 s
	1000	10 s

Table 4. 3 Estimated thicknesses of the WO_3 and PB thin films[9].

Substrate	Sample	substrate area (cm^2)	substrate before spin coating (g)	substrate after spin coating (g) (evaporated suspension)	Amount of coated (g)	Estimated film thickness (μm)
ITO/PET	WO_3	25	0.3722	0.3823	0.0101	1.24
	PB	25	0.3740	0.3770	0.0031	1.11
ITO/glass	WO_3	25	4.4302	4.4394	0.0092	1.13
	PB	25	4.3854	4.3882	0.0028	1.04

4) Fabrication of electrochromic devices (ECDs)

The electrolyte solution was prepared by mixing polycarbonate (PC, 99%; Kanto Chemicals Co., Inc.) and potassium bis(trifluoromethanesulfonyl)imide (KTFSI, 1.5 mol kg^{-1}; FUJIFILM Wako Pure Chemicals Co.). Viscosity of the electrolyte solution was adjusted by adding 30 wt.% polymethyl methacrylate (PMMA; FUJIFILM Wako Pure Chemicals Co.) to prepared gel electrolyte. After the electrolyte was applied to the PB thin film, a UV sealing material was applied to each corner to prevent electrolyte leakage, and the weight of the two materials was adjusted so that the gap between WO_3 of ECD and PB was 50 μm. Next, the WO_3 thin film was bonded to the PB thin film under vacuum, and the effective area of the finished EC device was 16 cm^2. The ECDs prepared in this study are referred to as either a PET-based ECD and a glass-based ECD.

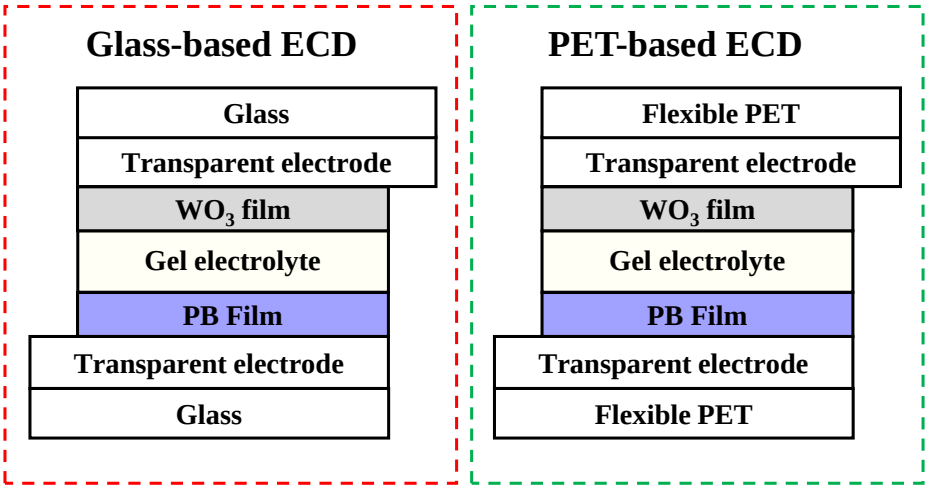

Figure 4. 3 Structure of glass- and PET-based ECDs[9].

5) ECD characterization

The ECDs were evaluated in accordance with protocols used in our previous studies[6,11]. The chromaticity was measured using a UV-visible (UV-vis) spectrophotometer(DH-2000, Ocean Optics), and the luminance (L*) and chromaticity coordinates (a* and b*) data of colored and bleached glass- and PET-based ECDs are transmittance. calculated from the spectrum. Luminance (L*) represents the change in brightness between 0 (black) and 100 (white), and the color of the film is determined by the a* and b* coordinates: Positive values of a* tend to be red and negative values are green, while b* values tend to be yellow in positive numbers and blue in negative values. Haze was measured using a haze meter (NDH 7000, Nippon Denshoku Industries Co. Ltd). The electrochemical and EC properties of the film were measured using CV, CC, and MPS measurements, and the investigation was conducted using an electrochemical measurement system (6115D, ALS/HCH), in combination with a multi-channel charge-coupled device detector (DH-2000, Ocean Optics) to measure in-situ transmittance changes. Multiple potential step (MPS) measurements, transmission spectra, and time strip charts were obtained based on estimated response times. The EC switching time is defined as the time required for the total transmittance to exhibit a 90% change. CC measurements were used to estimate the transferred charge density (Q).

4. 3 Results and discussion

1) Surface treatment of ITO substrates

Although the vacuum plasma method is commonly used for the hydrophilization of substrate surfaces[12], this method can induce plasma damage in organic substrates. Therefore, in this study, UV treatment was adopted for surface treatment. The UV light surface treatment reduced the content of non-polar groups, while increasing the content of polar components, and the formation of various photo oxides on the ITO surface led to increased hydrophilicity[13-15]. These modifications increase the surface energy of ITO. The contact angles of the PB and WO_3 inks dropped on the surface-treated substrates were evaluated after treatment at various UV irradiation intensities (Figure 4. 4).

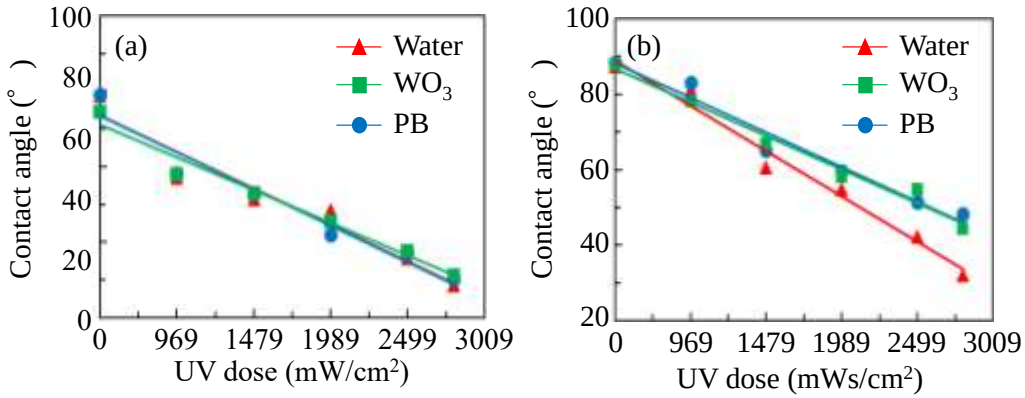

Figure 4. 4 Contact angles of the PB and WO_3 inks dropped on the (a) ITO/glass and (b) ITO/PET substrates after UV treatment at various UV irradiation intensities[9].

The contact angles of WO_3 and PB on the ITO/glass and PET substrates were found to decrease from 80° to 34° and from 85° to 45°, respectively, with increasing UV dose; the optimal effect without any damage to the flexible substrate was achieved at a UV dose of 2805 mW s cm^{-2}. The UV surface treatment shows a higher effect as increase the UV irradiation intensity.

2) Effect of light-ageing on ECD properties

Light-ageing of the ECDs with short-circuited electrodes afforded a transparent appearance due to presence of oxidised WO_3 and reduced PB. UV irradiation facilitated the injection of K+ into the electronic states of PB for the reduction of Fe^{III}–N to Fe^{II}–N as follows[16,17]

$$Fe_4^{III}[Fe_{II}(CN)_6(blue) + 4K^- + 4e^- \rightarrow K_4Fe_4^{II}[Fe^{II}(CN)_6(colorless) \quad (4\text{-}2)$$

The PB thin film in the sealed ECD was protected from oxidative degradation, thereby minimising its participation in the oxidation of PB[17,18].

3) Electrochemical and EC properties

The CV curve recorded at an applied potential ranging from −1.2 to +1.0 V at a sweep rate of 5 mV s^{-1} is shown in Figure 4. 5. The glass-based ECD exhibited a significantly larger CV area than that of PET-based ECD. It is thought that the sheet resistance of ITO/PET (~50 sq^{-1}) is about 4 times higher than that of ITO/glass substrates (~12 Ω sq^{-1}). In addition, 0.44 and 0.23 were obtained for glass- and PET-based ECDs, respectively, when potentials of −1.2 and +1.0 V were applied for 60 s (Figure 4. 5(b)). Thus, glass-based ECDs with lower electrical resistance compared to PET-based ECD had about twice the charge (C) for oxidation and reduction reactions. However, PET-based ECD showed that the estimated charge balance ($C_{transparent}/C_{colored}$) was greater than 98%, indicating that the reversible K^+ charge/discharge process occurred smoothly as described in equations (4-2) and (4-3)[19,20].

Cathodic reaction:

$$WO_3(colorless) + xK^+ + e^- = K_xWO_3\ (blue) \quad (4\text{-}3)$$

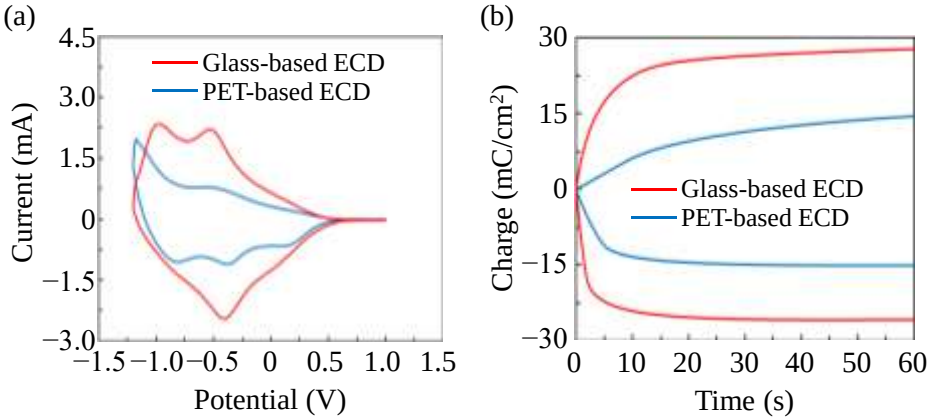

Figure 4. 5 (a) CV and (b) CC profiles of the glass-based (red) and PET-based (blue) ECDs[9].

Figure 4. 6(a-b) show the transmittance spectra of glass- and PET-based ECDs corresponding to the colored and bleached states using UV-vis spectroscopy during CC analysis. The transmittance change of 80% and 79% at a wavelength of 633 nm were obtained for glass- and PET-based ECDs, which showed excellent EC properties. MPS measurement was performed to determine the switching response of the film. The transmittance change at a wavelength of 633 nm was measured by applying constant voltages of +1.0, −1.2, and +1.0 V, as $V_{initial}$, V_{step1}, and V_{step2}, for 30, 60, and 60 sec, respectively (Figure 4. 6(c-d)).

The switching times of the ECDs between the colored ($t_{colored}$) and transparent ($t_{transparent}$) states was evaluated using the time in which 90% change in transmittance was achieved. The PET-based ECD exhibited $t_{colored}$ and $t_{transparent}$ values of 16.79 and 19.03 s, respectively, which were higher than those of the glass-based ECD. However, there was no significant difference in the response time between the two types of ECDs, as obtained in the CV and CC analyses (Figure 4. 5), despite the lower current values. This result shows promise for lower current drive in future applications, which could reduce the power consumption of a device. A shorter switching time is also expected if a substrate with a lower sheet resistance than ITO-coated substrates is used.

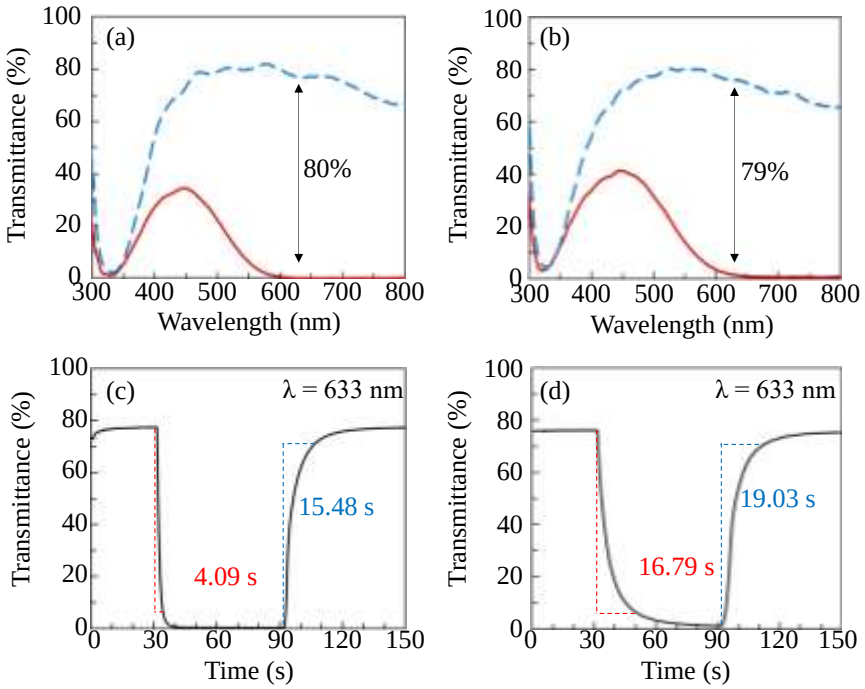

Figure 4. 6 Transmittance spectra of the transparent (blue lines) and colored (red lines) states of (a) glass-based, (b) PET-based ECDs. Optical switching speed between the transparent (blue lines) and colored (red lines) states of (c) glass-based and (d) PET-based ECDs.

4) Chromaticity and haze of ECDs

The chromaticity and haze of ECD are shown in Figure 4. 7, which is an important characteristic to comply with regulations related to automobile and aircraft window materials. (Table 4. 4 provides details on the haze and chromaticity values). The CIELAB color space is a system designed to be similar to human vision and was used to determine the color coordinate values (L*, a*, and b*) of all ECDs in the colored and bleached state (Figure 4. 7(a) and (b)). When a constant voltage of −1.2V was applied, the a* and b* values abruptly dropped below −15 corresponding to the blue color for all ECDs. By contrast, when +1.0 V was applied, the ECDs all changed from blue to transparent (L* > 85).

In addition, the haze values of both ECDs were as low as less than 5% in the transparent state. For application to windows and doors, visual transmittance >70% and haze <2% are desirable in a transparent state[21]. Moreover, the ECDs maintained

Table 4. 4 Chromaticity and haze of glass- and PET-based ECDs.

Substrate	colour states	Real colour	Haze	L*	a*	b*
PET	Coloured		3.61	47.67	-18.28	-38.89
	Transparent		2.93	91.35	-2.63	3.6
Glass	Coloured		3.06	41.99	-15.51	-42.96
	Transparent		4.19	88.94	-7.58	1.65

colored and bleached states even when power was removed, indicating a promising energy-efficient device.

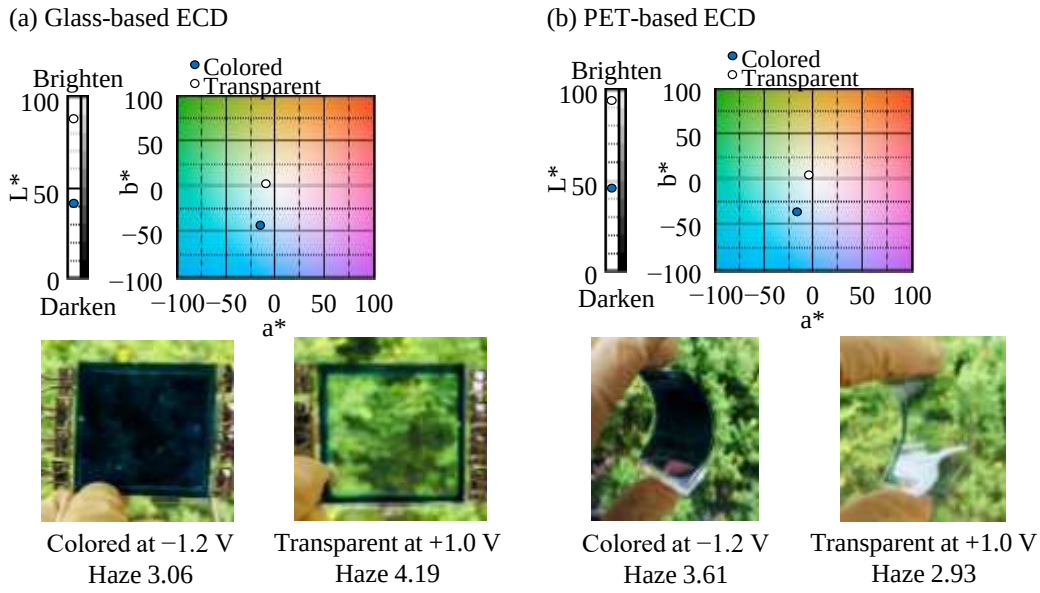

Figure 4. 7 Variation in CIELAB color coordinates (L*, a*, b*) and photographs of the (a) glass-based ECD and (b) PET-based ECD in the colored and transparent states.

The transmittance changes of ECDs in the colored and bleached states were evaluated up to 100 cycles at a wavelength of 633 nm using MPS measurements (Figure 4. 8). All ECDs showed no notable degradation in transmittance changes which indicate electrochemically very stable. In addition, the PET-based ECDs were mechanically robust to repeated bending and torsion experiments.

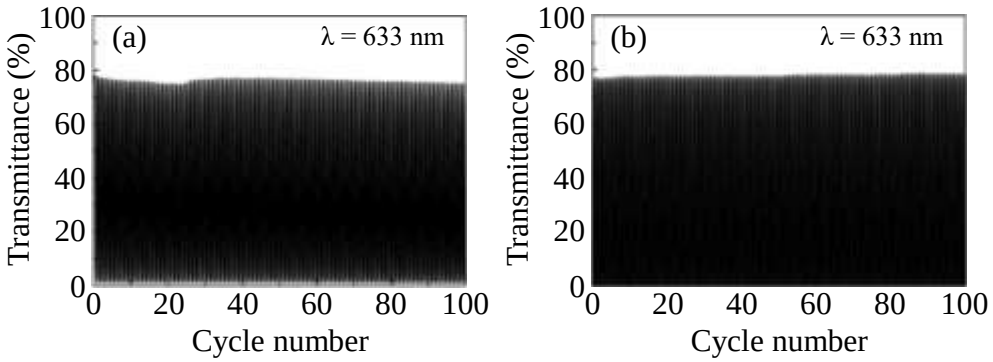

Figure 4. 8 Cycle durability at a wavelength of 633 nm up to 100 cycles of (a) glass-based ECD and (b) PET-based ECD. MPS measurements was conducted at constant voltages of −1.2 and +1.0 V.

The optical density (Δ*OD*) and EC staining efficiency (*CE*), which are important EC parameters controlling the electrochemical performance of the film, were calculated using the follows equations:

$$\Delta OD = \log_{10}(T_b/T_c) \quad (4\text{-}5)$$

$$\eta = \Delta OD/Q \quad (4\text{-}6)$$

where T_c and T_b are the transmittance in colored and bleached states of ECDs, respectively, and Q is the amount of injected charge (Table 4. 5).

Table 4. 5 Transmittance (*T*), optical density(Δ*OD*), coloration efficiency (*CE*), and optical switching time of ECDs with different substrate at 633 nm in their colored and bleached states.

Wavelength (nm)	Substrate	ECD area (cm^2)	$T_{bleached}$ (%)	$T_{colored}$ (%)	Charge (C)	Q (C/cm^2)	$A_{bleached}$	$A_{colored}$	Δ*OD*	*CE* (cm^2/C)
633	PET	16	79.89	1.31	0.23	0.01	0.10	1.88	1.78	123.32
	Glass	16	80.00	0.32	0.44	0.03	0.10	2.50	2.40	86.44

Figure 4. 9 shows a plot of the Δ*OD* at 633 nm versus the charge density observed in the colored state at a potential of −1.2 V, and *CE* was calculated the slope of the line that fits the linear region. The glass-based ECD exhibited a higher Δ*OD* of 2.40 than the

other ECDs due to the largest change in transmittance. However, small value of Q of the PET-based ECD caused exhibiting the largest *CE* value of 123.32 cm^2 C^{-1}. This value was higher than other ECDs using Li^+ of cations smaller than K^+. Therefore, we strongly believe that the results of this study will provide a new comprehensive foundation for the development of ECDs for applications in next-generation smart windows (automobiles, airplanes, buildings, etc.) that require greater flexibility than glass.

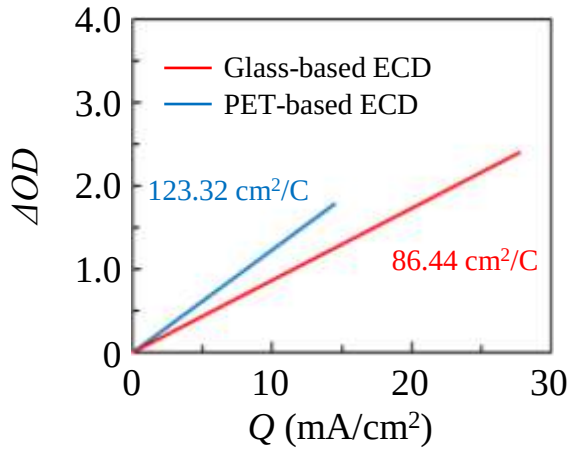

Figure 4. 9 The *in situ* optical density change with respect to the charge density of the (red) glass and (blue) flexible-based ECDs.

4. 4 Conclusions

ECD with higher flexibility than glass was prepared by spin coating methods using water-based inks well-dispersed WO_3 and PB NPs on an ITO/PET substrates. The surface of ITO substrates was UV treated to improve the adhesion properties of WO_3 and PB inks to the film. PET-based ECD were fabricated using K^+-based gel electrolytes. The PET-based ECD showed the highest *CE* (123.32 cm^2 C^{-1}) and excellent EC performance, including good cycling stability. CIE diagrams (L*, a*, and b*) were used to describe the color changes of the fabricated ECDs, and PET-based ECD showed dramatic color changes from blue to transparent. In addition, the haze of PET-based ECD in the bleached state was less than 3%, indicating clear transparency. Therefore, the excellent EC properties of ECD prepared by combining the WO_3 and PB thin films prepared on flexible transparent PET substrates show their potential as candidate materials for next-generation smart windows such as automotive applications. However, several problems remain, such as environmental stability (e.g., resistance to temperature, humidity, UV rays) and the method of introduction, for the application of this device as automotive window materials. Thus, Adhesion and Interface Research Group at AIST will work with the company to conduct research and development to produce field-applicable samples as the next step.

Reference

[1] C.G. Granqvist, Electrochromism and smart window design, Solid State Ionics, 53 (1992) 479. https://doi.org/10.1016/0167-2738(92)90418-O

[2] C.G. Granqvist, M.A. Arvizu, İ. Bayrak Pehlivan, H.-Y. Qu, R.-T. Wen, G.A. Niklasson, Electrochromic materials and devices for energy efficiency and human comfort in buildings: A critical review, Electrochim. Acta, 259 (2018) 1170. https://doi.org/10.1016/j.electacta.2017.11.169

[3] A. Azens, C.G. Granqvist, Electrochromic smart windows: energy efficiency and device aspects, J. Solid State Electrochem. 7 (2003) 64. https://doi.org/10.1007/s10008-002-0313-4

[4] P.R. Somani, S. Radhakrishnan, Electrochromic materials and devices: present and future, Mater. Chem. Phys., 77 (2003) 117. https://doi.org/10.1016/S0254-0584(01)00575-2

[5] A.K. Sethi, S.P. Sethi, Flexibility in manufacturing: A survey, Int. J. Flex. Manuf. Syst. 2 (1990) 289. https://doi.org/10.1007/BF00186471

[6] C.Y. Jeong, H. Watanabe, K. Tajima, Adhesive electrochromic WO_3 thin films fabricated using a WO3 nanoparticle-based ink, Electrochim. Acta, 389 (2021) 138764. https://doi.org/10.1016/j.electacta.2021.138764

[7] M. Ishizaki, K. Kanaizuka, M. Abe, Y. Hoshi, M. Sakamoto, T. Kawamoto, H. Tanaka, M. Kurihara, Preparation of electrochromic Prussian blue nanoparticles dispersible into various solvents for realisation of printed electronics, Green Chem. 14 (2012) 1537. https://doi.org/10.1039/C2GC35079C

[8] M. Ishizaki, Y. Sajima, S. Tsuruta, A. Gotoh, M. Sakamoto, T. Kawamoto, H. Tanaka, M. Kurihara, Preparation of yellow core–blue shell coordination polymer nanoparticles using active surface coordination sites on a prussian-blue analog, Chem. Lett. 39 (2009) 1058. https://doi.org/10.1246/cl.2009.1058

[9] C.Y. Jeong, T. Kubota, K. Tajima, Flexible electrochromic devices based on tungsten oxide and Prussian blue nanoparticles for automobile applications, RSC Adv. 11 (2021) 28614. https://doi.org/10.1039/D1RA05280B

[10] H.-F. Xiang, Z.-X. Xu, V. A.L. Roy, C.-M. Che, P.T. Lai, Method for measurement of the density of thin films of small organic molecules, Rev. Sci. Instrum. 78 (2007) 034104. https://doi.org/10.1063/1.2712932

[11] K. Tajima, H. Watanabe, M. Nishino, T. Kawamoto, Green fabrication of a complementary electrochromic device using water-based ink containing nanoparticles of WO3 and Prussian blue, RSC Adv. 10 (2020) 2562. https://doi.org/10.1039/C9RA09153J

[12] Y. Takata, S. Hidaka, A. Yamashita, H. Yamamoto, Evaporation of water drop on a plasma-irradiated hydrophilic surface, Int. J. Heat Mass Transfer 25 (2004) 320. https://doi.org/10.1016/j.ijheatfluidflow.2003.11.008
[13] Z. Xu, Z. Ao, D. Chu, A. Younis, C. M. Li, S. Li, Reversible hydrophobic to hydrophilic transition in graphene via water splitting induced by UV irradiation, Sci. Rep. 4 (2014) 6450. https://doi.org/10.1038/srep06450
[14] E. Bormashenko, R. Pogreb, G. Whyman, Y. Bormashenko, R. Jager, T. Stein, A. Schechter, D. Aurbach, The reversible giant change in the contact angle on the polysulfone and polyethersulfone films exposed to UV irradiation, Langmuir 24 (2008) 5977. https://doi.org/10.1021/la800527q
[15] H. Y. Nie, M. J. Walzak, B. Berno, N. S. McIntyre, Atomic force microscopy study of polypropylene surfaces treated by UV and ozone exposure: modification of morphology and adhesion force, Appl. Surf. Sci. 144 (1999) 627. https://doi.org/10.1016/S0169-4332(98)00879-4
[16] C. Gervais, M.A. Languille, S. Reguer, M. Gillet, E.P. Vicenzi, S. Chagnot, F. Baudelet and L. Bertrand, “Live” Prussian blue fading by time-resolved X-ray absorption spectroscopy, Appl. Phys. A: Mater. Sci. Process. 111 (2013) 15. https://doi.org/10.1007/s00339-013-7581-y
[17] C. Gervais, M.A. Languille, S. Reguer, C. Garnier, M. Gillet, Light and anoxia fading of Prussian blue dyed textiles, Heritage Sci. 2 (2014) 26. https://doi.org/10.1186/s40494-014-0026-x
[18] C. Y. Jeong, T. Kubota, K. Tajima, M. Kitamura, H. Imai, Complementary electrochromic devices based on acrylic substrates for smart window applications in aircrafts, Mater. Chem. Phys. 277 (2022) 125460. https://doi.org/10.1016/j.matchemphys.2021.125460
[19] F. Ricci, F. Arduini, A. Amine, D. Moscone, G. Palleschi, Characterisation of Prussian blue modified screen-printed electrodes for thiol detection, J. Electroanal. Chem. 563 (2004) 229. https://doi.org/10.1016/j.jelechem.2003.09.016
[20] M. Hepel, L. I. Dela-Moss, H. Redmond, Lattice polarization effects in electrochromic switching in WO_{3-x} films studied by pulse-nanogravimetric technique, J. Solid State Electrochem. 18 (2014) 1251. https://doi.org/10.1007/s10008-013-2219-8
[21] R. Koua, Y. Zhonga, J. Kim, Q. Wang, M. Wang, R. Chen, Y. Qiao, Elevating low-emissivity film for lower thermal transmittance, Energy Build. 193 (2019) 69. https://doi.org/10.1016/j.enbuild.2019.03.033

Chapter 5

Preparation of WO_3 Nanoparticle Dispersion Ink Using Machine Learning

5. 1 Introduction

Adhesion and Interface Research Group at National Institute of Advanced Industrial Science and Technology (AIST) has been working on the development of coated EC devices, which are expected to have lower cost for application in smart window technology as described in Chapters 4 and 5[1-5]. This device uses a thin film material prepared by a wet-coating methods using a functional nanoparticle dispersion ink, and various additives are being studied to improve the adhesion to the substrate, lifespan, and stability. However, the synthesis of functional nanoparticle dispersion inks involves a wide range of parameters, such as the number of additional materials, thickness of thin films, chemical composition and structure, synthesis method, or film-forming processes. Therefore, a lot of time and labor is required for the optimal ink preparation and thin film production process which shows good EC properties. Thus, in this chapter, Adhesion and Interface Research Group at AIST aimed to derive the optimal ink composition in a short time using machine learning (ML) which is one of the data-based research and development methods[6-10]. These various parameters were informatized through data processing of the results obtained through previous experiments, and a simulation model with predictable results was proposed using Python.

The optical density (ΔOD) coloration efficiency (CE) is very important information for EC materials, and they can be calculated using the following equations.

$$\Delta OD = \log_{10}(T_b/T_c) \quad (5\text{-}1)$$

$$CE = \Delta OD/Q \quad (5\text{-}2)$$

where T_c and T_t are the transmittance in colored and bleached states of ECDs, respectively.

If the ΔOD and CE can be predicted by simulation, the change in transmittance (absorption) and electrochemical properties; transferred charge density (Q) according to the oxidation-reduction reaction of the EC materials can be predicted. Therefore, in this study, we focused on deriving the optimal ink production conditions in a short time by predicting the ΔOD and CE (output) from the preparation parameters of WO_3 NPs

dispersion ink (input) using Python. In addition, in the field of EC materials, there are very few applied studies on machine learning. Therefore, finding the optimum WO_3 NPs dispersed ink preparation conditions in a short time by constructing an appropriate model will have a great impact as a proposal for a new EC material research method.

5. 2 Experimental

1) Machine learning

Figure 5. 1 shows the schematic diagram of the ML method in this study. The amount of water, WO_3 NPs and PVA were used as parameters for the synthesis of enhanced WO_3 ink through ML and those were optimized for EC material production. First, various production conditions of previous experiments (input) and obtained results (output) were converted into a database for ML. Then, to obtain the optimal conditions for the EC materials preparation, the prepared parameter data values are input to the simulation model to predict the results. Finally, the accuracy of ML is verified by comparative analysis with the EC properties of WO_3 ink obtained through simulation and experimental under the same conditions.

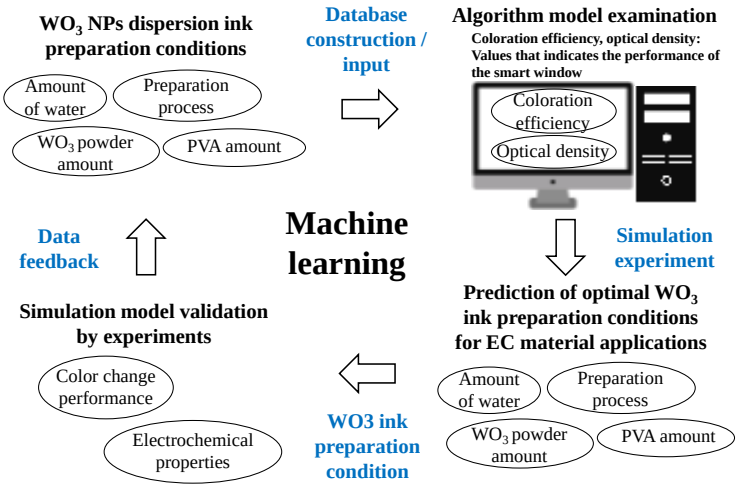

Figure 5. 1 Schematic of machine learning in this study.

2) Support Vector Machine (SVM)

SVM, developed by Vapnik[11], is a relatively new machine learning technique for materials optimizations[12,13]. It has been shown to perform well for classification and regression[14,15]. SVM has two distinct features that are useful for materials optimization. Firstly, it has high generalization ability. Secondly, it is especially suitable for small size of training sets[14]. The scikit-learn libraries for SVM in Python are listed as shown in Figure 5. 2.

```
from sklearn import svm
from sklearn import ensemble

from sklearn.model_selection import train_test_split
import pandas as pd
from pandas import DataFrame
import numpy as np
import matplotlib.pyplot as plt
from sklearn.metrics import mean_squared_error
from sklearn.metrics import r2_score
import pickle
import os
```

Figure 5. 2 Terms of Skit-learn libraries for the ML in this study.

3) Support Vector Regression (SVR) and Gaussian process regression

The basic concept of SVR is to map nonlinearly the original data x into a higher dimensional feature space and solve a linear regression problem in this feature space[15-19]. The feature space is determined by kernel functions. Popular kernel functions include the Linear kernel, Polynomial kernel, and Gaussian kernel, among many others[20]. In this study, we chose the radial basis function (RBF) kernel function, also called Gaussian kernel, to predict the EC properties of WO_3 NPs dispersed ink (Figure 5. 3). The RBF kernel outperforms others for simple modelling process, high computation efficiency and easy realization[21].

```
if M == 0:
    model = svm.SVR(C=100.0, kernel='rbf',  gamma='auto', epsilon=0)
elif M ==1:
    model = ensemble.RandomForestClassifier(n_estimators=100,
random_state=1)
elif M ==2:
    pass
else:
    print("error")
```

Figure 5. 3 RBF kernel for machine learning in this study.

The RBF kernel is defined as follows[22].

$$K(X, X_i) = \exp(-\gamma \parallel X_1 - X_{new} \parallel^2) \quad (5\text{-}3)$$

where, γ is the RBF kernel parameters, and $||X_1 - X_{new}||$ is distance between two points X_1 and X_i.

γ can be described as: $\frac{1}{2\sigma^2}$

Thus,

$$K(X, X_i) = \exp(-\frac{\|X-X_i\|^2}{2\sigma^2}) \quad (5\text{-}4)$$

where, σ is the variance and our hyperparameter.

The regularization parameter (*C*) determines the degree to which misclassification is acceptable, and is expressed as:

$$\min_{\beta} \frac{1}{2} \| \beta \|^2 + C \sum_{i=1}^{N} \xi_i \quad (5\text{-}5)$$

where, β denotes the normal vector, ξ_i denotes the distance to the current margin with $\xi_i \geq 0$, i =1, …, n,

RBF kernel support vector machines (SVM) are implemented in the scikit-learn library and have two hyperparameters associated with them ('*C*' for SVM and 'γ' for RBF kernel). where γ is inversely proportional to σ.

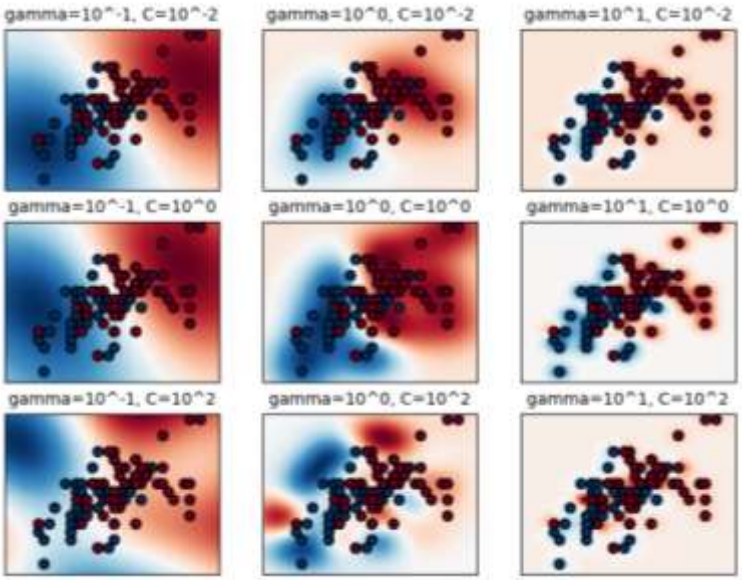

Figure 5. 4 RBF kernel support vector machines according to the change of γ or σ and *C* values[23].

Figure 5. 4 shows that as γ increases (σ decreases), the model overfits; overfitting is a modeling error in statistics that occurs when a function is too closely aligned to a limited set of data points. Therefore, it is significant to find the correct γ or σ along with the C value to achieve the best bias-variance trade-off; the bias–variance tradeoff is the property of a model that the variance of the parameter estimated across samples can be reduced by increasing the bias in the estimated parameters..

4) WO_3 NPs dispersed inks and films preparation

Table 5. 1 shows the experimental data provided for machine learning. Table 5. 2 and Figure 5. 5 shows the conditions of WO_3 inks preparation and *CE* obtained from simulation.

$$d = m/(A \times \rho) \tag{5-6}$$

where ρ is the density of the ink, A is the area of the substrate, and m is the weight of the coated WO_3 NPs dispersed ink.

The weights of the ITO/glass substrates and WO_3 inks are shown in Table 5. 3.

Table 5. 1 The experimental data provided for machine learning.

No	CE (cm^2/C)	H_2O_wt.%	WO_3_wt.%	PVA_wt.%
1	0.873313	74.81297	24.93766	0.249377
2	0.773333	74.07407	24.69136	1.234568
3	0.005657	73.17073	24.39024	2.439024
3	1.660732	79.84032	19.96008	0.199601
4	0.902243	79.20792	19.80198	0.990099
5	0.141647	78.43137	19.60784	1.960784
6	0.525778	84.87269	14.97753	0.149775
7	0.367506	84.36725	14.88834	0.744417
8	0.204342	83.74384	14.77833	1.477833
9	0.472268	89.91009	9.99001	0.0999
10	0.521543	89.55224	9.950249	0.497512
11	0.160329	89.10891	9.90099	0.990099
12	0.06633	94.95252	4.997501	0.049975
13	0.116861	94.76309	4.987531	0.249377
14	0.098174	94.52736	4.975124	0.497512
15	0.007951	69.79063	29.91027	0.299103

Table 5. 2 The condition of WO_3 NPs dispersed inks and *CE* values obtained from simulated.

No	CE (cm^2/C)	H_2O_wt.%	WO_3_wt.%	PVA_wt.%
0	8.805386	95	5	0
1	9.195912	94.98	5	0.02
2	9.591482	94.96	5	0.04
…	…	…	…	…
69340	35.06985	74.4	24.8	0.8
…	…	…	…	…
104998	14.91341	58.14	34.9	6.96
104999	14.91341	58.12	34.9	6.98

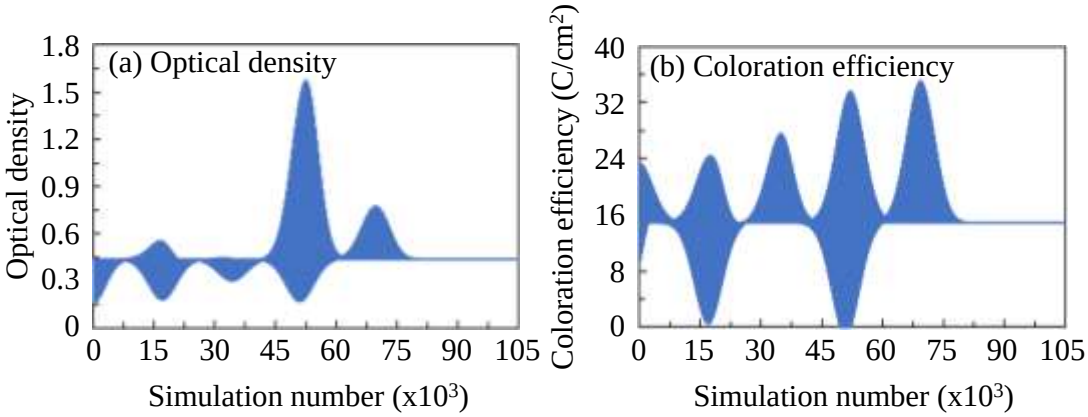

Figure 5. 5 Plot of (a) Δ*OD* and (b) *CE* values obtained according to the simulation number.

Table 5. 3 Randomly selected WO_3 NPs dispersed ink preparation condition.

No.	CE (cm^2/C)	H_2O_wt.%	WO_3_wt.%	PVA_wt.%
3508	18.151	93.84	6	0.16
9571	13.63848	89.88	7.7	2.42
36809	17.00239	83.32	15.5	1.18
50099	30.9531	79.72	19.3	0.98
58099	14.91341	71.52	21.5	6.98
69340	35.06985	74.4	24.8	0.8

Table 5. 4 Weights of the ITO substrate and coated WO_3, and the calculated WO_3 film thickness.

No.	ITO substrate size (cm^2)	ITO substrate before spin coating (g)	ITO substrate after spin coating (g) (evaporated suspension)	Amount of coated WO_3 (g)	Calculated films thickness
3508	25	4.3094	4.3203	0.0107	1.24
9571	25	4.2988	4.3094	0.0106	1.23
36809	25	4.3710	4.3830	0.0120	1.39
50099	25	4.2822	4.2944	0.0122	1.41
58099	25	4.2866	4.2992	0.0140	1.46
69340	25	4.2558	4.2672	0.0114	1.32

5) Electrochemical and EC characteristics of the WO_3 films

The electrochemical and EC properties of the film were measured using CV, CC, and MPS measurements, and the investigation was conducted using an electrochemical measurement system (6115D, ALS/HCH), in combination with a multi-channel charge-coupled device detector (DH-2000, Ocean Optics) to measure in-situ transmittance changes. Multiple potential step (MPS) measurements, transmission spectra, and time strip charts were obtained based on estimated response times. The EC switching time is defined as the time required for the total transmittance to exhibit a 90% change. CC measurements were used to estimate the transferred charge density (Q).

5. 3 Results and discussion

The electrochemical and EC properties of WO_3 films deposited on ITO/glass substrates were measured in a 1.5 mol/kg KTFSI/PC solution as electrolyte. Cyclic voltammograms were recorded by measuring WO_3 films over a potential range of –1.2 to +1.0 V (vs. Ag/AgCl) with a sweep rate of 10 mV/s (Figure 5. 6).

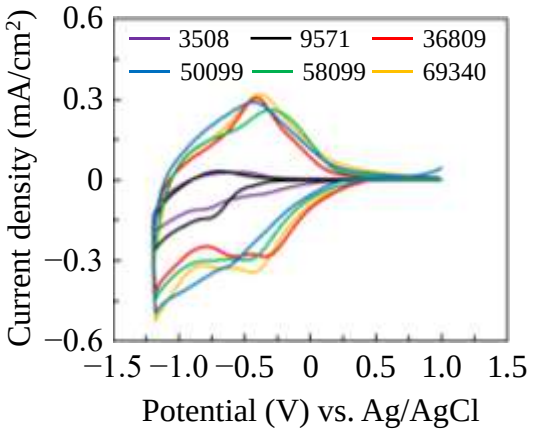

Figure 5. 6 CV curves of the WO_3 thin films prepared under condition of No. 3508 (purple), 9571 (black), 36809 (red), 50099 (blue), 58099 (green), and 69340 (yellow). The potential scan rate was 10 mV/s[13].

It was observed that the area of the CV curve which indicates the electrochemical characteristics increased as the amount of WO_3 NPs powder added increased. This is thought to be because the number of W atoms contributing to the redox reaction increases as the amount of WO_3 NPs powder increases. However, there was no significant difference in CV area in the thin film containing more than about 20 wt.% of WO_3 NPs powder.

The transferred charge density (ΔQ) was determined by charge amount obtained by applying constant potentials of –1.2 and +1.0 V for 5 and 120 s, respectively, for a complete redox reaction and the resultant current densities are exhibited with respect to time (Figure 5. 7). The reversible K^+ charge/discharge process obtained for the prepared WO_3 films. No. 58099 (green line) showed a lower ΔQ value than that of No. 36809 (red line), which contained a smaller amount of WO_3 NPs powder. It is thought that a large amount of PVA added deteriorated the electrochemical properties as described

Chapter 3. The No. 50099 exhibited the largest ΔQ of 38 mC/cm^2 (Table 5. 4).

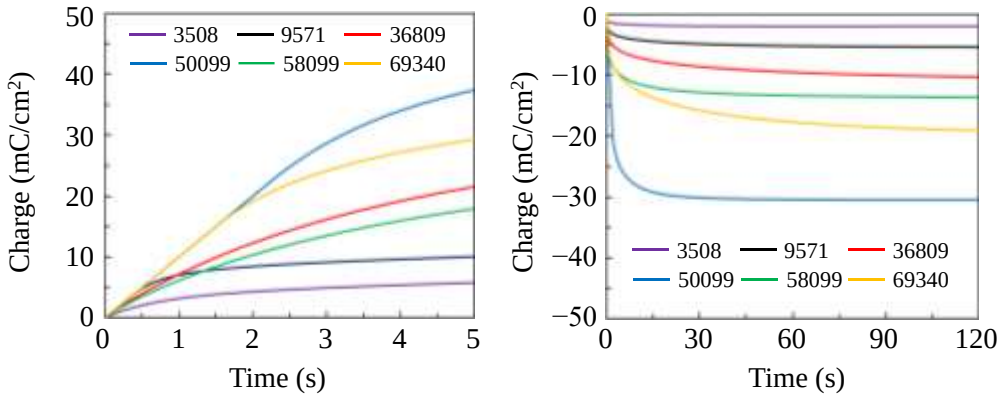

Figure 5. 7 CC of the WO_3 thin films prepared under condition of No. 3508 (purple), 9571 (black), 36809 (red), 50099 (blue), 58099 (green), and 69340 (yellow). Constant voltages of –1.2 to +1.0 V (vs. Ag/AgCl) were applied for 5 and 120 s, respectively.

Table 5. 5 Transmittance (T), optical density (ΔOD), coloration efficiency (CE), and optical switching time of the WO_3 thin films prepared under condition of No. 3508, 9571, 36809, 50099, 58099, and 69340 at 633 nm in the colored and bleached states in a 1.5 mol/kg KTFSI/PC electrolyte solution.

	633 nm					OD		CE (cm²/C)	
No.	$T_{bleached}$	$T_{colored}$	$A_{bleached}$	$A_{colored}$	ΔQ (C/cm²)	Experiment	Simulation	Experiment	Simulation
3508	93.14	74.34	0.031	0.129	0.006	0.098	0.310	16.97	18.15
9571	96.24	68.91	0.017	0.162	0.010	0.145	0.414	14.43	13.64
36809	91.22	39.58	0.040	0.403	0.022	0.363	0.336	16.82	17.00
50099	90.68	7.46	0.042	1.127	0.038	1.085	1.084	28.92	30.95
58099	90.80	44.66	0.042	0.350	0.018	0.308	0.439	17.20	14.91
69340	85.76	6.50	0.067	1.187	0.029	1.120	0.745	38.21	35.07

The light transmittance changes of WO_3 thin films in colored and bleached states were studied by UV-vis spectroscopy during CC and the spectra are shown in Figure 5. 8.

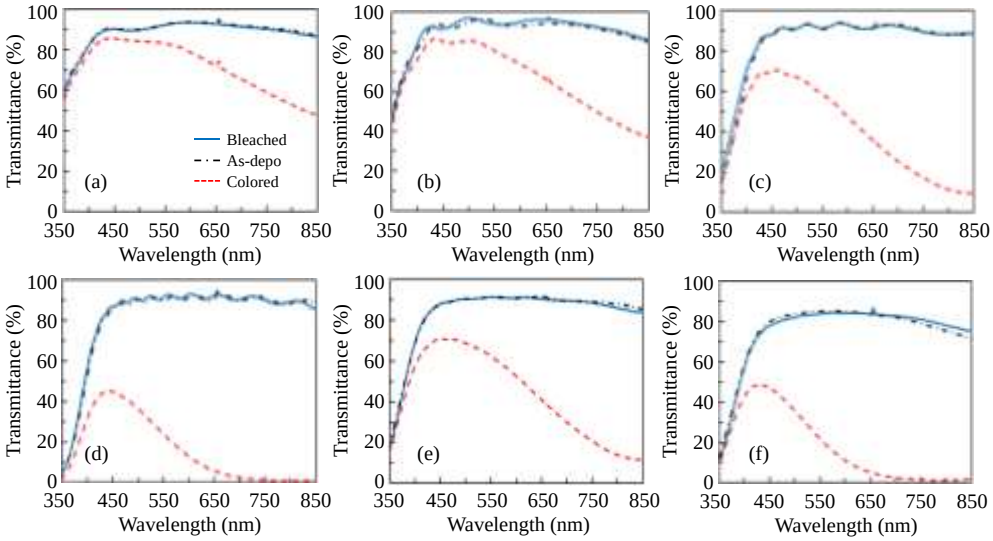

Figure 5. 8 Transmittance spectra of the WO_3 thin films prepared under condition of No. 3508 (a), 9571 (b), 36809 (c), 50099 (d), 58099 (e), and 69340 (f). Constant voltages of –1.2 to +1.0 V (vs. Ag/AgCl) were applied for 5 and 120 s, respectively.

The highest transmittance change (ΔT) of 83 % was observed for the No. 50099. Furthermore, ΔOD and CE, which are important EC parameters controlling the electrochemical performance of the film, were calculated using equations (1) and (2) and listed in Table 5. 5.

The largest ΔOD value of 1.085 was obtained for the No. 50099 and the experiment value was very similar to the simulation value (Table 5. 5). In contrast, A large error range in the ΔOD values was obtained for the experiments and simulations of No. 3508 and 9571. This is thought to be due to the sufficiently small ΔOD values. However, there is no problem in examining the conditions for producing the WO_3 ink exhibiting the optimum EC characteristics. Interestingly, the highest CE value of 38.21 cm^2/C was obtained for No. 69340, which was consistent with the simulation results (Table 5. 5). This is thought to be because, although No. 50099 showed a higher transmittance change than No. 69340, it showed a similar transmittance change at 633 nm at a low charge amount. Figure 5. 9 (a), (b) shows the plots of the results obtained through the experiments in Chapter 3 and this chapter and the results obtained through the simulations. As a result, ΔOD and CE values showed high accuracy of 96% and 92%, respectively.

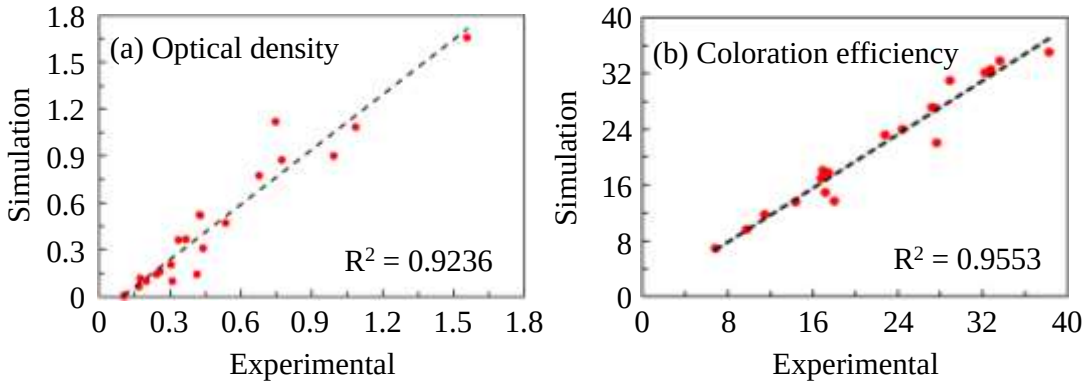

Figure 5. 9 Plots of the (a) Δ*OD* and (b) *CE* values obtained through the experiments and simulations. Simulation: predicted Δ*OD* and *CE* values by simulation (dashed line). Experimental: Δ*OD* and *CE* values obtained by experimental (red dots).

5. 4 Conclusions

In this study, machine learning was applied to obtain the optimal WO_3 NPs dispersed ink preparation condition for the application of EC materials. The Δ*OD* and CE values of WO_3 ink under various conditions were predicted by using SVR and RBF kernel in a short time, and the optimized preparation conditions for the coating process were reviewed. The highest predicted values of Δ*OD* and *CE* obtained through simulation showed high accuracy of over 90% compared to experimental values. In contrast, although the error range was large in the experiments and simulations which indicate the low Δ*OD* values, there was no problem in obtaining the conditions for preparing the WO_3 ink showing the optimal EC characteristics. In addition, the highest *CE* value of 38.2 cm^2/C obtained through this study was improved by about 10% compared to the *CE* value (35.0 cm^2/C) of Chapter 3. We believe that these results will lead and suggest a new development direction for EC research in the future. In addition, in future studies, we propose a more extensive machine learning development study by considering more variables such as various additives (surface active materials, binders, etc.) and manufacturing processes.

Reference

[1] C.Y. Jeong, H. Watanabe, K. Tajima, Adhesive electrochromic WO_3 thin films fabricated using a WO_3 nanoparticle-based ink, Electrochim. Acta, 389 (2021) 138764. https://doi.org/10.1016/j.electacta.2021.138764

[2] C.Y. Jeong, T. Kubota, K. Tajima, Flexible electrochromic devices based on tungsten oxide and Prussian blue nanoparticles for automobile applications, RSC Adv. 11 (2021) 28614. https://doi.org/10.1039/D1RA05280B

[3] K. Tajima, H. Watanabe, M. Nishino, T. Kawamoto, Green fabrication of a complementary electrochromic device using water-based ink containing nanoparticles of WO_3 and Prussian blue, RSC Adv. 10 (2020) 2562. https://doi.org/10.1039/C9RA09153J

[4] C. Y. Jeong, T. Kubota, K. Tajima, M. Kitamura, H. Imai, Complementary electrochromic devices based on acrylic substrates for smart window applications in aircrafts, Mater. Chem. Phys. 277 (2022) 125460. https://doi.org/10.1016/j.matchemphys.2021.125460

[5] C.Y. Jeong, T. Kubota, C. Chotsuwan, V. Wungpornpaiboon, K. Tajima, All-solid-state electrochromic device using polymer electrolytes with a wet-coated electrochromic layer, J. Electroanal. Chem. 897 (2021) 115614. https://doi.org/10.1016/j.jelechem.2021.115614

[6] J. Wei, X. Chu, X.-Y. Sun, K. Xu, H.-X. Deng, J. Chen, Z. Wei, M. Lei, Machine learning in materials science, InfoMat 1 (2019) 338. https://doi.org/10.1002/inf2.12028

[7] H. Wei, S. Zhao, Q. Rong, H. Bao, Predicting the effective thermal conductivities of composite materials and porous media by machine learning methods, Int. J. Heat Mass Transf. 127 (2018) 908. https://doi.org/10.1016/j.ijheatmasstransfer.2018.08.082

[8] Y. Liu, J. Wu, G. Yang, T. Zhao, S. Shi, Predicting the onset temperature (Tg) of Ge_xSe_{1-x} glass transition: a feature selection based two-stage support vector regression method, Sci. Bull. 64 (2019) 1195. https://doi.org/10.1016/j.scib.2019.06.026

[9] L. Xu, L. Wencong, J. Shengli, L. Yawei, C. Nianyi, Support vector regression applied to materials optimization of sialon ceramics, Chemom. Intell. Lab. Syst. 82 (2006) 8. https://doi.org/10.1016/j.chemolab.2005.08.011

[10] S.S. Gilan, H.B. Jovein, A.A. Ramezanianpour, Hybrid support vector regression – Particle swarm optimization for prediction of compressive strength and RCPT of concretes containing metakaolin, Constr Build Mater. 34 (2012) 321. https://doi.org/10.1016/j.conbuildmat.2012.02.038

[11] V. Vapnik, Statistical Learning Theory, John Wiley and Johns, New York (1998).

[12] A.J. Smola, B. Schölkopf, A Tutorial on Support Vector Regression, NeuroCOLT

Technical Report NC-TR-98-030, Royal Holloway College, University of London, UK (1998)
[13] N.-Y. Chen, W.-C. Lu, J. Yang, G.-Z. Li, Support Vector Machine in Chemistry, World Scientific Publishing Company, Singapore (2004).
[14] A.I. Belousov, S.A. Verzakov, J. von Frese, A flexible classification approach with optimal generalisation performance: support vector machines, Chemometr. Intell. Lab. Syst., 64 (2002) 15. https://doi.org/10.1016/S0169-7439(02)00046-1
[15] S.F. Fang, M.P. Wang, W.H. Qi, F. Zheng, Hybrid genetic algorithms and support vector regression in forecasting atmospheric corrosion of metallic materials, Comput. Mater. Sci. 44 (2008) 647. https://doi.org/10.1016/j.commatsci.2008.05.010
[16] V.N. Vapnik, S. Golowich, A. Smola, Support vector method for function approximation, regression estimation and signal processing,M. Mozer, M. Jordan, T. Petsche (Eds.), Advance in Neural Information Processing System, vol. 9, MIT Press, Cambridge (1997), pp. 281-287.
[17] V.N. Vapnik, The Nature of Statistical Learning Theory, Springer Verlag, New York (1995)
[18] S.R. Gunn, Support vector machines for classification and regression, ISIS Technical Report, University of Southampton (1998).
[19] J. Platt, IEEE Intell. Syst. 13 (1998) 26.
[20] E. Yapıcı, H. Akgün, K. Özkan, Z. Günkaya, A. Özkan, M. Banar, Prediction of gas product yield from packaging waste pyrolysis: support vector and Gaussian process regression models, Int. J. Environ. Sci. Technol. (2022). https://doi.org/10.1007/s13762-022-04013-1
[21] J. Sun, J. Zhang, Y. Gu, Y. Huang, Y. Sun, G. Ma, Prediction of permeability and unconfined compressive strength of pervious concrete using evolved support vector regression, Constr. Build. Mater. 207 (2019) 440. https://doi.org/10.1016/j.conbuildmat.2019.02.117
[22] X. Wang, F. Huang, Y. Cheng, Super-parameter selection for Gaussian-Kernel SVM based on outlier-resisting, Measurement, 58 (2014) 147. https://doi.org/10.1016/j.measurement.2014.08.019
[23] Scikit-learn, Machine Learning in Python, https://scikit-learn.org/stable/auto_examples/svm/plot_rbf_parameters.html

Chapter 6

Research Summary

Research summary

In this study, WO_3 NPs dispersion ink with excellent adhesion was developed for the fabrication of electrochromic devices capable of wet coating, device fabrication tests were performed using the developed materials, and performance was predicted and demonstrated using machine learning.

To improve the adhesion between the WO_3 nanoparticles and the substrate of the ink, polyvinyl alcohol (PVA) was added as an additive. PVA was adjusted to 0-10 wt.%, and electrochemical properties and EC properties were studied. As a result, the WO_3 thin film prepared with 1 wt.% PVA addition showed excellent adhesion between WO_3 nanoparticles and substrate. In addition, it was found that the composition of the WO_3 thin film exhibiting excellent electrochemical properties with the largest coloration efficiency of 35 cm^2/C and electrochromic properties with a change in visible light (λ = 633 nm) transmittance of 90%⇔13%.

To fabricate the next-generation EC device, we investigated the fabrication of flexible ECD using a PET substrate. For the preparation of EC materials, coated WO_3 and PB films were prepared using the WO_3 synthesized in Chapter 3 and the PB ink originally developed by Adhesion and Interface Research Group at National Institute of Advanced Industrial Science and Technology (AIST), and these were assembled to prepare a flexible EC device. The prepared flexible PET EC device showed a dramatic color change from transparent to dark blue and showed higher coloring efficiency (123.32 cm2 / C) than the conventional glass EC device (86.44 cm2 / C). Furthermore, it showed electrochemical stability without deterioration up to 100 cycles, and mechanically excellent durability against repeated bending and twisting experiments.

Finally, machine learning was applied to obtain the optimal WO_3 NPs dispersed ink preparation condition for the application of EC materials. The predicted value obtained through simulation showed an accuracy of more than 90% with the experimental value. In addition, the highest coloring efficiency value of 38.2 cm^2/C obtained through this study was improved by about 10% compared to the coloring efficiency value (35.0 cm^2/C) of Chapter 3. Therefore, we believe that it is possible to develop an optimized process for the preparation of EC materials using machine learning. In the future, we will focus on the development of functional nano-dispersion inks optimized to prepare functional thin films using various parameters (materials, manufacturing conditions, atmosphere, etc.) through simulation prediction using more advanced algorithms.

Achievements of This Research

Journal papers

1) C. Y. Jeong, H. Watanabe, K. Tajima, Adhesive electrochromic WO_3 thin films fabricated using a WO_3 nanoparticle-based ink, Electrochim. Acta 389 (2021) 138764.

2) C. Y. Jeong, T. Kubota, K. Tajima, Flexible electrochromic devices based on tungsten oxide and Prussian blue nanoparticles for automobile applications, RCV Adv. 11 (2021) 28614.

Domestic Conference

1) C. Y. Jeong, K. Tajima, H. Watanabe, M. Nishino, T. Kawamoto, D. Fukushi, S. Saito, Preparation of Tungsten Oxide Nanoparticle Dispersion Slurry and Evaluation of Electrochromic Characteristics, The 87th Meeting of the Electrochemical Society, Online (3. 2020)

2) C. Y. Jeong, K. Tajima, H. Watanabe, H. Akiyama, T. Kamei. M. Fukui, Improvement of wettability of PB nanoparticle dispersion ink and evaluation of EC characteristics by examining surface treatment method, The 88th Meeting of the Electrochemical Society, Online (3. 2021)

Others

1) Journal papers

1. 1) C. Y. Jeong, Y. Abe, M. Kawamura, K. H. Kim, T. Kiba, Electrochromic properties of rhodium oxide thin films prepared by reactive sputtering under an O_2 or H_2O vapor atmosphere, Sol. Energy Mater. Sol. Cells 200 (2019) 109976.

1. 2) C. Y. Jeong, Y. Abe, M. Kawamura, K. H. Kim, T. Kiba, H. Watanabe, K. Tajima, T. Kawamoto, Electrochromic properties of sputter-deposited rhodium oxide thin films of varying thickness, Thin Solid Films 709 (2020) 138226.

1. 3) C. Y. Jeong, T. Kubota, C. Chotsuwan, V. Wungpornpaiboon, K. Tajima, All-solid-state electrochromic device using polymer electrolytes with a wet-coated electrochromic layer, J. Electroanal. Chem. 897 (2021) 115614.

1. 4) K. Tajima, C. Y. Jeong, T. Kubota, T. Ito, K. Araki, T. Kamei. M. Fukui, Mass-producible slit coating for large-area electrochromic devices, Sol. Energy Mater. Sol. Cells, 232 (2021) 111361.

1. 5) C. Y. Jeong, T. Kubota, K. Tajima, M. Kitamura, H. Imai, Complementary electrochromic devices based on acrylic substrates for smart window applications in aircrafts, Mater. Chem. Phys. 277 (2022) 125460. https://doi.org/10.1016/j.matchemphys.2021.125460

2) International Conferences

2. 1) C. Y. Jeong, Y. Abe, M. Kawamura, K. H. Kim, T. Kiba, Electrochromic properties of rhodium oxide thin films prepared by reactive sputtering in O_2 and H_2O atmosphere, 13th International Meeting on Electrochromic (IME-13), Chiba, Japan (8. 2018)

2. 2) C. Y. Jeong, Y. Abe, M. Kawamura, K. H. Kim, T. Kiba, Optical and electrochromic properties of rhodium oxide thin films prepared by reactive sputtering in O_2 and H_2O atmosphere, American Vacuum Society (AVS) 65th International Symposium &Exhibition, Long Beach, U.S.A (10. 2018)

2. 3) C. Y. Jeong, Y. Abe, M. Kawamura, K. H. Kim, T. Kiba, Electrochromic properties of sputter-deposited rhodium oxide thin films with various film thicknesses, The 15th International Symposium on Sputtering & Plasma Processes (ISSP2019), Kanazawa, Japan (6. 2019)

3) Domestic Conference

3. 1) C. Y. Jeong, Y. Abe, M. Kawamura, K. H. Kim, T. Kiba, Preparation of rhodium oxide thin films by reactive sputtering and their electrochromic properties, The 78th Meeting of The Japan Society of Applied Physics (JSAP), Hakata, Fukuoka, Japan (9. 2017)

3. 2) C. Y. Jeong, Y. Abe, M. Kawamura, K. H. Kim, T. Kiba, Effect of substrate temperature on the electrochromic properties of the rhodium oxide thin film prepared by reactive sputtering method in water vapor atmosphere, 53th Meeting of The Japan Society of Applied Physics (JSAP), Hokkaido Chapter, Sapporo(1. 2018)

3. 3) C. Y. Jeong, Y. Abe, M. Kawamura, K. H. Kim, T. Kiba, Evaluation of electrochromic properties of rhodium oxide thin films prepared by reactive sputtering in O_2 and H_2O atmosphere, The 85th Meeting of the Electrochemical Society (ECSJ), Tokyo (3. 2018)

3. 4) C. Y. Jeong, Y. Abe, M. Kawamura, K. H. Kim, T. Kiba, Effect of thickness of rhodium oxide thin film prepared by reactive sputtering method on electrochromic properties, The 86th Meeting of the Electrochemical Society, Kyoto (3. 2019)

3. 5) C. Y. Jeong, Y. Abe, M. Kawamura, K. H. Kim, T. Kiba, H. Watanabe, K. Tajima, T. Kawamoto, Enhanced electrochromic characteristics of rhodium oxide thin film for smart window application, The Chemical Society of Japan Autumn Program 9th CSJ Chemistry Festa 2019, Tokyo (10. 2019)

4) Awards

4. 1) The 10th Symposium of Korea Scientists and Engineers Association in Japan Joint Subcommittee "Academic Best Award", 2. 2019

4. 2) The 15th International Symposium on Sputtering & Plasma Processes Best Poster

Presentation Award, 6. 2019

Acknowledgments

I would like to thank those who have given me much help and support for this research. First and foremost, I want to express my great gratitude to Professor **Yoshio Abe**, for offering me the opportunity to pursue my PhD degree under your supervision. He taught electronic materials and various technologies from the basics for 5 years and gave me the opportunity to participate in various academic societies, broadening my horizons as a scientist. He always respected my decisions and choices and gave me sincere advice. His trust and support encouraged me to dig into matters which have never been touched upon. Also, there were many cases where I barely submitted my papers at conferences or thesis deadlines, but nevertheless, thank you for always patiently waiting. Furthermore, he supported me to become a scholarship student at Rotary Club, etc. so that I could focus on my studies.

I would also like to express my gratitude to Professors **Midori Kawamura**, **Kyung Ho Kim**, and **Takayuki Kiba** for their numerous professional comments and advice in preparing various papers, research reports, and conference presentations.

My deepest gratitude is also due to the members of the supervisory committee Professor **Naofumi Ohtsu**, Professor **Takeshi Matsuda**. They provided individual advice and opinions on my research.

I must give special thanks to the members of the Adhesion and Interfacial Research Group of Nanomaterials Research Institute at National Institute of Advanced Industrial Science and Technology (AIST).

First and foremost, I would like to thank you for every moment spent with Dr. **Kazuki Tajima**, an advisor to AIST. I have benefited greatly from my fellowship with them over the past three years. He treated me strictly with regards to my research and at the same time guided me with an open mind. Furthermore, I learned a lot about how to think scientifically. His profound knowledge, insight, and selfless devotion left a deep impression on me. Thank you for his patience to answer many of my questions, big or small, and sometimes silly questions. Moreover, the way you live, and work has inspired me. His strong support has made it possible for me to have 4 theses accepted during my 3 years of doctoral course.

I would also like to thank Dr. **Haruhisa Akiyama** for his many suggestions regarding my research. Special thanks to Dr. **Kazumasa Shimamoto**, who taught me how to use Python for machine learning from the basics. Because of his help, I was able to acquire new skills to apply informatics science to material development.

I wish to thank Mr. **Hiroshi Watanabe** and Mr. **Takashi Kubota**. I am very grateful

to them for their valuable advice and scientific discussions on electrochromic experiments. Also, the constant support and information sharing in the experiment has always yielded good results. Furthermore, I would also like to thank Dr. **Kazuhiko Tonooka** and Dr. **Hitoshi Taguchi,** for providing sincere advice and critical opinions on the experimental results from a new point of view rather than from an electrochemical view.

I would like to especially thank the members of the Nanoparticle Functional Design Group of Nanomaterials Research Institute at AIST. Dr. **Tohru Kawamoto** who is the group reader allowed me to conduct research at his group for about one and a half years, so I was able to study and share opinions about nanomaterials with electrochromic as well as adsorption properties during the research. Dr. **Akira Takahashi** gave detailed information about XRD that I did not know, which was very helpful in analyzing the XRD data for my anomaly study. I also benefited from meetings with Dr. **Hatsuho Usuda**, Dr. **Yuta Shudo** Dr. **Higashi Tanaka**, Dr. **Parajuli Durga**, Dr. **Kimitaka Minami**, Mr. **Yutaka Sugiyama**, Ms. **Keiko Noda**, Ms. **Masami Kawakami**, Mr. **Koji Sakurai**, Mrs. **Akiko Shiomi**, Ms. **Chieko Tatamura**, Mr. **Takehiko Hiwatari**, Ms. **Yoshie Mishima**, and Mr. **Naoki Nakashima**.

Thanks to all colleagues in the Electronic Materials Laboratory at in Kitami institute of Technology (KIT). Especially, thank them so much to my dear comrades **Yuki Yokoiwa**, **Yasunari Nozaki**, and **Ryo Kawanami**, who helped me so much so that I could adjust to studying in Japan. The two-year master's course I spent with you guys was so precious and fun to me. In addition, thank them to my dear junior students **Yusuke Ito**, **Fan Wang**, **Nakai Chihiro**, **Yasuhiro Ayauchi**, and **Masataka Kataoka** for always respecting me, and for helping me with my poor Japanese. The exchange of opinions about the research I shared with you has been very helpful in completing this research.

I would like to profoundly thank the **Okazaki**, **Hayase**, **Matsubara** families my Japanese friends, and my Korean seniors and juniors at the KIT for the past 5 years. Thanks to my Japanese teacher Ms. Suzue Murata. My Japanese has made great progress with her help.

I would also like to thank Mr. **Wonsig Jin**. He was the first to recognize my potential for growth as a Ph.D. and taught me the virtues and character that a person should have not only academically but also in human relationships. Dr. **Kyong Moo Lee** helped me a lot in adjusting to Japan, and he became a mentor and supported me mentally until I completed my research.

Finally, I would like to show my deepest appreciation to my family and fiancé

Kinoshita Akari, who have given me a chance and great supports. Their supports have always been the driving force to my study and life in KIT and AIST these five years.